Dissertation

submitted to the
Combined Faculties of the Natural Sciences and Mathematics
of the Ruperto-Carola-University of Heidelberg, Germany
for the degree of
Doctor of Natural Sciences

presented by
Dipl.-Phys. Jan-Patrick Porst
born in Pretoria
Oral examination: February 1st, 2011

High-Resolution Metallic Magnetic Calorimeters

for

β-Spectroscopy on ^{187}Rhenium

and

Position Resolved X-Ray Spectroscopy

Referees:

Prof. Dr. C. Enss

Prof. Dr. K. Blaum

This thesis describes the development of metallic magnetic calorimeters (MMCs) for high resolution spectroscopy. MMCs are energy dispersive particle detectors based on the calorimetric principle which are typically operated at temperatures below 100 mK. The detectors make use of a paramagnetic temperature sensor to transform the temperature rise upon the absorption of a particle in the detector into a measurable magnetic flux change in a dc-SQUID.
The application of MMCs for neutrino mass measurements and their advantages with respect to other approaches are discussed. In view of this application the development of an MMC optimized for β-endpoint spectroscopy on ^{187}rhenium is presented. A fully micro-fabricated X-ray detector is characterized and performs close to design values. Furthermore, a new technique to more efficiently couple rhenium absorbers mechanically and thermally to the sensor was developed and successfully tested. By employing a metallic contact, signal rise times faster than 5 μs could be observed with superconducting rhenium absorbers.
In addition to the single pixel detectors, an alternative approach of reading out multiple pixels was developed in this work, too. Here, the individual absorbers have a different thermal coupling to only one temperature sensor resulting in a distribution of different pulse shapes. Straightforward position discrimination by means of rise time analysis is demonstrated for a four pixel MMC and a thermal model of the detector is provided. Unprecedented so far, an energy resolution of less than $\Delta E_{\mathrm{FWHM}} < 5\,\mathrm{eV}$ for 5.9 keV X-rays was achieved across all absorbers.

Hochauflösende Metallische Magnetische Kalorimeter für die β-Spektroskopie an ^{187}Rhenium und die ortsaufgelöste Röntgenspektroskopie

In der vorliegenden Arbeit wird die Entwicklung, Herstellung und Charakterisierung von hochauflösenden Metallischen Magnetischen Kalorimetern (MMC) beschrieben. Ein magnetisches Kalorimeter ist ein energiedispersiver Teilchendetektor, der bei Temperaturen unter 100 mK betrieben wird. Der Energieeintrag wird dabei in Form einer Temperaturänderung und der damit verbundenen Magnetisierungsänderung des paramagnetischen Temperatursensors durch ein sensitives DC-SQUID-Magnetometer nachgewiesen.
Die Verwendung von MMCs zur Neutrinomassenbestimmung durch β-Endpunktspektroskopie an ^{187}Rhenium und die Vorzüge dieser Methode im Vergleich zu anderen Ansätzen wird diskutiert und ein im Hinblick auf diese Anwendung optimierter Detektor vorgestellt. Die Charakterisierung eines vollständig mikrostrukturierten Röntgendetektors bestätigt weitgehend die Erwartungen an die thermodynamischen Eigenschaften aller Detektorkomponenten. Darüber hinaus wird ein neues Verfahren beschrieben, das es erlaubt, Rheniumabsorber sowohl mechanisch als auch thermisch sehr gut mit dem Temperatursensor zu verbinden. Mit Hilfe einer metallischen Verbindung können so Signalanstiegszeiten unter 5 μs in unterschiedlichen supraleitenden Rheniumabsorbern beobachtet werden.
Zusätzlich zu der Entwicklung von Ein-Pixel-Detektoren wird in dieser Arbeit ein Detektor entwickelt, der es erlaubt mit nur einem Temperatursensor mehrere Absorberelemente auszulesen. Die einzelnen Röngtenabsorber sind dafür thermisch unterschiedlich stark an den Sensor gekoppelt und eine Energieabsorption in dem jeweiligen Absorber führt zu verschiedenen Signalanstiegszeiten. Für einen Detektor mit vier Absorbern wird mit Hilfe einer Analyse der Signalanstiegszeiten eine eindeutige Pixelzuordnung nachgewiesen, zudem wird ein thermisches Modell für diesen Detektortyp dargestellt. Mit 5.9 keV Röntgenquanten konnte für Energiespektren in allen vier Absorbern eine für diesen Detektortyp bisher unerreichte Energieauflösung unter $\Delta E_{\mathrm{FWHM}} < 5\,\mathrm{eV}$ gemessen werden.

Contents

II Experiment

Introduction

In the early 1950s Reines and Cowan experimentally proved the existence of the weakly interacting neutrinos. Their *Project Poltergeist* adopted the upcoming technique of using liquid scintillators to develop a large scale detector that could provide evidence of the neutrino via inverse β-decay.

As an artificial neutrino source they chose the largest accessible fission reactor in Savannah, USA, after dismissing their first plans of using a nuclear explosion. The detector consisted of 4200 liters of scintillation material placed 11 meters from the reactor's core around two water tanks. The reactor neutrinos interacted with the water molecule protons, creating neutrons and positrons. Each positron created a pair of gamma rays after annihilating with an electron, whereas the neutron was absorbed by cadmium in the tank leading to a delayed emission of a gamma ray. A low background environment was established by using 12 meters of overburden to reduce background events caused by cosmic rays. All of this was required to achieve a signal to total accidental background ratio of 20:1 while detecting a few thousand neutrino induced events. The existence of the neutrino could finally be proven in 1956 [Cow56] and marked the beginning of exciting decades with experiments investigating neutrino physics.

The neutrino was then included sixfold as a massless particle in the *Standard Model*. Roughly ten years later, the neutrino was again in the focus of experimental interest. With the detection of neutrinos escaping from our Sun models of the Sun's internal fusion processes could be tested. Surprisingly, these experiments showed a lack of detected electron neutrinos, which could not be described by any of the solar models. This discrepancy soon led to the hypothesis of neutrino flavor transitions, the so called neutrino flavor oscillations. Theoretically, this mixing of the neutrino's weak interacting states can only occur, if the rest masses differ from each other. In terms of the neutrino itself, oscillations imply nonzero rest masses.

This result reaches well beyond only solar neutrinos. On cosmic scales the gravitational theory of the evolution of the universe is affected, on a subatomic level it impacts the so far very robust and durable *Standard Model* of elementary particle physics. Therefore a quantitative determination of the neutrino mass spectrum is desirable to solidify the base for advanced theories beyond the Standard Model.

Nowadays laboratory based neutrino mass measurements are possible by, for example studying the single β-decay. When an atom undergoes β-decay, a certain amount of energy is carried away by the electron, the electron antineutrino, and the recoiled daughter atom. Typically, the bulky atom remains relatively still, while the electron and neutrino share the available energy. The observable energy spectrum of the electron is continuous up to an energy of almost Q, which is the maximal kinetic energy of the electron assuming a vanishing neutrino mass. Decay energy stored in the hypothetic rest mass of the neutrino is unavailable to the electron, and the mass of the neutrino can be determined from a careful measurement of the spectrum near the endpoint.

For the last forty years the spectrum of the tritium β-decay has been measured with different spectrometers. With these experiments, an upper limit of the neutrino mass of $2.0\,\mathrm{eV/c^2}$ was achieved [PDG10]. The upcoming KATRIN experiment [Ang04] will use a spectrometer based on the well established MAC-E Filter [Lob85] but, compared to older experiments, on a much larger scale and together with a high-intensity tritium source. The latter is needed to be able to collect large statistics close to the end point of the spectrum, where the finite neutrino mass becomes apparent. The aimed sensitivity is $m_{\nu_\mathrm{e}} = 0.2\,\mathrm{eV/c^2}$.

In this work an alternative concept has been followed, based on a calorimetric measurement of the ^{187}Re β-spectrum. For several reasons the isotope ^{187}Re is a promising candidate for this type of neutrino mass measurement. Rhenium exhibits one of the lowest known end point energies in nature with $Q = 2.47\,\mathrm{keV}$ and the natural abundance of the isotope of interest lies around 63%. Due to its high nuclear charge number, it also efficiently stops the emitted electron and can therefore be used as source and absorber at the same time. The experiment is complimentary to KATRIN, as it is based on completely different experimental techniques and faces entirely different experimental challenges.

For the experiments described in this work, a low temperature detector technique was employed. Based on a superconducting rhenium absorber a metallic magnetic calorimeter (MMC) was developed. While in previous experiments with this sensor type normal conducting absorbers were used the superconductivity of the absorber allows, due to its vanishing electronic heat capacity, for much larger detection volumes.

Operated at a temperature well below 100 mK, an MMC uses a highly sensitive paramagnetic thermometer[1]. The temperature information is obtained from the magnetization change of the paramagnetic sensor, which is located in a weak magnetic field. Any energy input leads to a change in magnetization in the sensor, which is read out with a low noise SQUID magnetometer. In addition to being a sensi-

[1]The paramagnetic sensor is based on a diluted alloy of gold with a few hundred ppm of erbium (Au:Er)

tive thermometer the detector benefits from the vanishing heat capacity towards low temperatures as well as the existence of very low noise magnetometers.

This work also introduces a multiplexing scheme which can be employed for MMC based detectors. Multiple absorbers are thermally linked to only one temperature sensor. The thermal links from the individual absorbers to the temperature sensor are varied such that pixel discrimination is achieved based on the signal rise time. Using this scheme, the necessary readout channels for a given number of active pixels can be drastically reduced. This development also opens up the possibility to tailor the signal rise of single pixel detectors, a technique that can be useful for future work with rhenium absorbers.

The thesis is organized in the following way. Some experiments and facts on massive neutrinos are briefly summarized in chapter 1. The requirements for a calorimetric measurement of the ^{187}Re β-decay are discussed in detail. An experiment for determining the neutrino mass is outlined and the requirements for a suitable detector are defined.

Chapter 2 discusses the detection principle of magnetic calorimeters and possible multiplexing schemes. Theoretical background is given and new ideas leading to an optimized performance of a metallic magnetic calorimeter are introduced.

Chapter 3 discusses the employed experimental techniques. In chapters 4 and 5 the development and micro-fabrication of a detector specifically designed for rhenium β-spectroscopy is discussed. Here the design and fabrication of a multiplexed four pixel X-ray *Hydra* detector are included. Throughout the thesis, the detector developed for a rhenium experiment and the *Hydra* detector are treated in parallel, only features not common to both detector types are discussed separately.

In Chapter 6 measurements with three detectors towards a rhenium experiment are presented. A complete characterization of a fully micro-fabricated detector suitable for the readout of rhenium absorbers shows performance close to design values using 5.9 keV X-rays. A detector with polycrystalline rhenium absorber is characterized and results of a single pixel rhenium detector similar in volume to the one proposed in chapter 1 are presented. Finally, a thorough characterization, including a detailed thermal model, of a four pixel X-ray detector scheme is presented. An unprecedented energy resolution for such a device is demonstrated.

Part I

Theory

Chapter 1

Massive Neutrinos

The neutrino is one of the fundamental particles which make up the universe, and their number exceeds the count of all the atoms in the entire universe by far. Much of what is known about neutrinos was only learned within the last century. Neutrino discoveries have come so fast there was barely time to rebuild the conceptual matrix by which they might be understood.

At the beginning of the 20th century, conservation of energy and momentum seemed to be violated by the weak β^--decay of a neutron. The measured energy spectrum of the electrons was continuous. This was caused by the fact that only the electron and the proton could be detected, but the electron from a given beta-decay process was expected to be emitted with a constant energy. Thus, conservation of energy and momentum seemed to be violated. A possible solution was suggested by W. Pauli in 1930 by assuming a three body decay where a neutral not yet known particle is also generated. In the following years a theory including this particle was developed by E. Fermi.

Due to the extremely low cross section of this particle, which only interacts via the electroweak and gravitational forces, it took more than 20 years until its existence could be confirmed experimentally by F. Reines and C. Cowan in 1956 [Cow56]. Subsequently the neutrino was included sixfold in the Standard Model as an uncharged and massless Dirac particle. It belongs to the family of elementary particles called leptons and occurs in three flavors: the electron neutrino ν_e, the muon neutrino ν_μ and the tau neutrino ν_τ. Given the nature of Dirac particles, it appears as a neutrino and an antineutrino. Due to the fact that neutrinos do not carry any charge, they could also be their own antiparticles – which would make them so called Majorana particles – a question not answered yet.

Roughly ten years after the experimental evidence, the neutrino again was in the focus of interest as a discrepancy between the number of solar electron neutrinos detected on the earth and a number calculated from theoretical solar models was found. This discrepancy was explained with neutrino flavor oscillations – the fact that neutrino flavor states $(\nu_\mathrm{e}, \nu_\mu, \nu_\tau)$ are quantum superpositions of mass states

(ν_1, ν_2, ν_3) with nonzero masses. The existence of neutrino oscillations requires a nontrivial mixing of the weak interacting states and moreover, that the masses differ from each other. This in turn requires the neutrinos to carry a nonzero mass. Only a few decades after including the neutrino in the Standard Model, it is now the particle scrutinizing the Standard Model.

Over the last decades the neutrino became the focus of many experiments and theoretical work, where many aspects of neutrino physics are addressed. In the following paragraphs, a brief overview of the current status of neutrino physics will be given, which does not claim to be complete, but will motivate the efforts to develop methods and instrumentation for direct neutrino mass measurements.

1.1 Neutrino oscillation as proof of massive neutrinos

There are intense efforts to fully understand the neutrino mixings. Theoretically, the mixing of the weak interacting states is described by the mixing matrix $\mathbb{U}$. The entries U_{ij} of this matrix are parameterized by the mixing angles Θ_{ij}, the mass differences and the so called CP violating phase δ. If this matrix was the identity matrix, then the flavor eigenstates would be the same as the mass eigenstates. Mixing, however, is observed.

From experiments probing the neutrino oscillations, it is well established that the neutrinos do have nonzero rest masses. The two differences of squared neutrino masses observed so far in neutrino oscillation experiments provide neither the absolute mass values nor the order of the neutrino masses. The current neutrino phenomenology implies, that the three-neutrino mass spectrum m_i $(i = 1, 2, 3)$ is formed by a "doublet" of relatively close states and by a third "lone" neutrino state, which may be either heavier than the doublet (normal hierarchy) or lighter (inverted hierarchy). Both scenarios are depicted in figure 1.1. From additional, dispersion-like matter effects in solar neutrino oscillation, m_2 is known to be larger than m_1 [Fog06]. Furthermore, the mass difference between the mass eigenstates ν_1 and ν_2 is known to be much smaller than the mass difference of either of the doublet states to the third mass eigenstate ν_3.

In the most frequently adopted labeling of such states, the lightest (heaviest) neutrino in the doublet is called ν_1 (ν_2), so that their squared mass difference is $\delta m^2 = m_2^2 - m_1^2 > 0$. The lone state is then labeled as ν_3 and the sign of $m_3^2 - m_{1,2}^2$ distinguishes the normal hierarchy from the inverted hierarchy. The mass differences are small and separate m_3 from a more closely spaced doublet m_1 and m_2. From oscillation data it can be deduced that, independently of the mass scheme, at least two neutrinos have nonzero mass, with masses larger than about 8 meV. Furthermore, in contrast to the very weak mixing in the quark sector, the mass eigenstates are strongly mixed in the weak interaction. The mixing angle θ_{12} dominating the

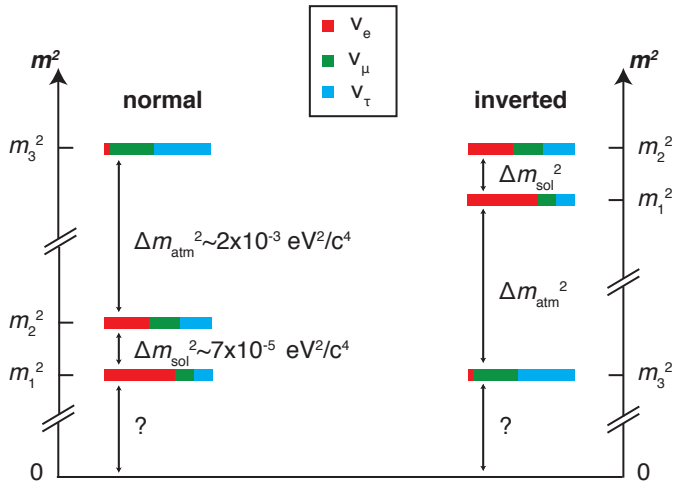

Figure 1.1 Configurations of neutrino mass states as suggested by oscillation measurements. Currently, a normal (left) and an inverted (right) hierarchy cannot be distinguished. The flavor composition is implied as a color code as well (see text for details).

observed ν_e, ν_μ oscillation of solar and reactor oscillations is found to be about 34° [Sch08], while the angle θ_{23}, dominating the observed atmospheric neutrino oscillation of ν_μ to ν_τ, is large and compatible with maximum mixing (45°) but not necessarily so [Sch08].

The oscillation between the electron and tau flavors is mainly described by the mixing angle θ_{13} and is yet to be discovered. The available data allow for θ_{13} being nonzero [Fog08a]. Three large scale reactor antineutrino disappearance experiments – DoubleChooz in France [Wan09], Daya Bay in China [Ard06] and RENO in South Korea [Kim08] – are currently being built to search for a non-vanishing θ_{13} mixing angle, which might open the way to unveiling CP violation in the leptonic sector.

In table 1.1 the current limits on the mixing in the neutrino sector are summarized, giving the neutrino mass differences $\delta m^2 = m_2^2 - m_1^2$ and $\Delta m^2 = \left| m_3^2 - \frac{m_1^2+m_2^2}{2} \right|$ (the largest and second largest squared mass gaps are then given by $\Delta m^2 \pm \delta m^2/2$ in both hierarchies) as well as the three mixing angles. Presently, no absolute mass scale is established. In order to gain knowledge about the absolute neutrino masses other aspects of neutrino physics complementing the mixing behavior need to be studied.

Table 1.1 Current knowledge of the neutrino mixing parameters. All quantities are given as 2σ ranges [Fog08b].

Parameter	2σ **range**
$\delta m^2 \left[10^{-5}\text{eV}^2\right]$	$7.31 - 8.01$
$\Delta m^2 \left[10^{-3}\text{eV}^2\right]$	$2.19 - 2.66$
$\sin^2 \Theta_{12}$	$0.278 - 0.352$
$\sin^2 \Theta_{23}$	$0.366 - 0.602$
$\sin^2 \Theta_{13}$	< 0.036

1.2 Searching for the neutrino mass

Presently, the upper limit for the mass of the anti-electron neutrino, $m_{\overline{\nu}_e}$, is $2.0\,\mathrm{eV/c^2}$ [PDG10]. Hence, the neutrinos are the lightest known massive particles, with a gap of about six orders of magnitude to the next lightest particle – the electron. It is one of the fundamental quests to establish an absolute mass scale for neutrinos due to the implications in particle physics as well as in cosmology.

Different methods are employed to investigate this field. From the measurement of the cosmic microwave background it is possible to set an upper value to $M_\nu = \sum_{i=1}^{3} m_{\nu_i}$ – the sum of the three mass eigenstate values. The positive identification of the neutrinoless double beta decay process would allow one to set an upper limit on $m_{2\beta} = \sum_{i=1}^{3} U_{li}^2 m_{\nu_i}$ – the coherent sum over all neutrino mass eigenvalues. Finally, investigating the single beta decay, the incoherent sum over the mass eigenstates $m_{\nu_l}^2 = \sum_{i=1}^{3} |U_{li}^2| m_{\nu_i}^2$ can be determined. A short overview is given in the next section.

Cosmology

As the neutrinos are known to carry mass, they play an important role in cosmological processes. Cosmological observations set a bound on the sum of the neutrino masses $M_\nu = \sum_i m_{\nu_i}$.

Within the first seconds after the Big Bang, a sea of neutrinos decoupled from the rest of matter. A dense (113 neutrinos and antineutrinos of each flavor per $\mathrm{cm^{-3}}$ [Les06]) blackbody radiation of so-called relic neutrinos similar to the cosmic microwave background remained. This cosmic neutrino background (CνB) has an estimated temperature of 1.95 K, which implies a very small cross section to be probed directly. These neutrinos are attributed to dark matter, which is solely seen by its gravitational interaction. The relic neutrinos came into existence from the same thermodynamical equilibrium state from which the cosmic microwave background radiation (CMBR) also originates. Currently, the most precise determination of the CMBR is delivered by the WMAP[1] satellite experiment. These data allow to set a limit to the sum of the neutrino masses $M_\nu = \sum_i m(\nu_i)$. According to cosmological models including the presence of the cosmological constant, cold dark matter and inflation, it is possible to extract information on the neutrino masses. This can be obtained by analyzing the fluctuations of the CMB, that contains information on the fluctuation in the matter density of the phase where photons decoupled from matter.

Currently, cosmology provides an upper bound on the neutrino mass. Even though the exact number is model dependent, a very conservative upper limit on the sum of neutrino masses can be quoted as $\sum_i m(\nu_i) \lesssim 0.6 - 0.7\,\mathrm{eV}$ at 95% confidence

[1] WMAP is an acronym for Wilkinson Microwave Anisotropy Probe, http://map.gsfc.nasa.gov/

level (C.L.) [Han10]. Improvements to this limit by more than one order of magnitude are expected in the near future for example by data from the Planck satellite [Tau04] or the polarization sensitive probing of the CMB anisotropies. This fact points out the power of cosmological investigations for neutrino physics but still underlines the need for a complementing direct measurement of the neutrino mass.

Supernovae

A completely different approach to study the properties of neutrinos is related to supernovae. In these astronomical events a stellar explosion can radiate as much energy as our Sun is expected to emit over its entire life span. Most of the energy produced in a supernova is radiated in the form of an immense burst of neutrinos. The observation of these neutrinos is not only important for the study of supernova dynamics, but also for the study of neutrino properties. In the supernova explosion SN1987A (discovered on February 24$^{\text{th}}$, 1987) four underground neutrino detectors were in operation: KAMIOKANDE-II (Japan), IMB (USA), Baksan (Russia) and LSD (France). These detectors observed an unusual number of events within a time window of about 10 s in the hours before the optical discovery of SN1987A. That the neutrinos arrive at the earth first is due to nature of the supernova, where the neutrino emission occurs simultaneously with the core collapse and before the emission of visible light, that occurs only after the shock wave reaches the stellar surface.

Although a huge number of approximately 10^{57} neutrinos are emitted in such an event, even the neutrino signal from a supernova explosion in the direct vicinity of our Milky Way is hard to detect. On the one hand, the detectors only cover a tiny fraction of the solid angle, on the other hand the cross section for detecting those traversing the detector is small. The total flux distributed on the surface of a sphere is continuously diluted by the expansion of the shell. Once this shell with a thickness of a few light seconds reaches a radius of 168 000 light years, "only" 10^{14} neutrinos per square meter remain. Out of these, about 25 caused events measured in one of the three detectors. They represent the first neutrinos detected which were clearly attributed to a precise astronomical source other than the Sun. Since neutrinos have nonzero mass, their transmitting velocities are smaller than that of light. This introduces a time-of-flight delay for neutrinos emitted by a source at a given distance and with a given energy [Pir81]. Assuming that the observed events are due to electron antineutrinos and neglecting neutrino mixing, this can lead to a model independent upper bound of $m_{\nu_e} \lesssim 30\,\text{eV/c}^2$ [Sch87]. There have been efforts to lower this upper bound by making assumptions on the cooling of the star and by applying more sophisticated statistical methods to the data. Currently the lowest limit set from the SN1987A data is $m_{\nu_e} \leqslant 5.7\,\text{eV/c}^2$ [Lor02].

Neutrinoless double-β-decay

Yet another method of determining the neutrino mass indirectly is to study the neutrinoless double-beta decay. Double-beta decay is a rare nuclear transition in which the charge of two isobaric nuclei changes by two units emitting two electrons. Two double-beta decay modes are possible.

A double-beta decay of a nucleus with emission of two neutrinos ($2\nu\beta\beta$) takes place if the single beta-decay is energetically forbidden but the decay to a nucleus with a charge difference of two units is allowed. Presently there are 35 isotopes known which can decay through the $2\nu\beta\beta$ process with forbidden or suppressed single-beta decay [Giu07]. Since this represents a second-order process of the weak interaction, half-lives are expected to be very long (of the order of 10^{20} years or even more). In this decay mode the neutrino is considered to be a Dirac particle.

The neutrinoless double-beta decay ($0\nu\beta\beta$) is a process in which the antineutrino emitted by one neutron can be absorbed as a neutrino by the other. The process is only possible if the lepton number is not conserved ($\Delta L = 2$), neutrino and antineutrino are identical (Majorana) and the exchanged neutrino changes helicity $|h| \neq 1$ (which is only possible for massive particles). Hence, if neutrinoless double-beta decay was observed, it would prove that neutrinos are Majorana particles and and also provide a measurement of the neutrino mass, since the half life of neutrinoless double-beta decay is related to the square of the neutrino mass:

$$T_{1/2}^{0\nu} = G^{0\nu} |M^{0\nu}|^2 \left(\frac{m_{2\beta}}{m_\mathrm{e}} \right)^2 , \tag{1.1}$$

where $G^{0\nu}$ is the phase space integral for the two electrons, $M^{0\nu}$ is the nuclear matrix element and $m_{2\beta}$ is the so-called effective Majorana neutrino mass. This mass is given by

$$m_{2\beta} = \sum_{i=1}^{3} U_{ei}^2 m_{\nu_i}, \tag{1.2}$$

i.e. the coherent sum over all neutrino mass eigenvalues m_i. Provided that the matrix element can be calculated with sufficient accuracy using theoretical models, the value of $m_{2\beta}$ can thus be derived from a measured decay rate for the given neutrinoless double-beta decay. Currently, the standard deviations of calculated values of the matrix elements are in the 5 % range [Rod06, Rod07]. In the absence of a detected signal, a lower limit on the half life $T_{1/2}^{0\nu}$ transforms into an upper limit on the neutrino mass, assuming the neutrino is a Majorana particle.

Unfortunately, even if $0\nu\beta\beta$ decay is allowed, it occurs at only a small fraction of the rate of $2\nu\beta\beta$. One of the main challenges of double beta decay searches, then, is to distinguish the little number of mono-energetic electron pairs produced by $0\nu\beta\beta$

decay from the large continuum of electron pairs produced through $2\nu\beta\beta$ decay.

The expected half-life of more than 10^{25} years for this decay channel is an ambitious challenge to experimental physics. All thinkable approaches searching for the evidence of neutrinoless double-beta decay are naturally large scale (in the order of 1 ton of active material), very low background experiments. Currently, there is a claim for evidence by the Heidelberg-Moscow collaboration studying the isotope ^{76}Ge [KK01] which set an upper limit to the effective Majorana-neutrino mass of $m_{2\beta} < 0.35\,\mathrm{eV/c^2}$. Present $m_{2\beta}$ sensitivities are still outside the range required to test the inverted neutrino mass hierarchy but future efforts are being made to pursue this goal. Several experiments are taking data or are planned to investigate this field of neutrino physics. To give a few examples, GERDA uses ^{76}Ge crystals as both a source and detector [Joc10] and within a few years it will be possible to test the results of the Heidelberg-Moscow experiment. COBRA employs telluride (^{130}Te) and cadmium (^{116}Cd) [Zub06], CUORICIONO and CUORE also investigate ^{130}Te employing TeO_2 crystals [Sis10, Arn08], and NEMO-3 uses molybdenum (^{100}Mo), selenium (^{82}Se) and other isotopes [Arn05]. The future sensitivity to the effective mass is foreseen to be lower than $m_{2\beta} < 0.05\,\mathrm{eV/c^2}$.

Direct searches through single β-decay

As described above, neutrino oscillation experiments are only sensitive to mass differences and indirect measurements are always model dependent. Direct measurements of the neutrino mass, however, are sensitive to the neutrino mass while being model independent. This class of experiments is given by the time of flight measurements of supernova neutrinos and by the study of the kinematics of weak decays. In the case of the kinematical study of the single-beta decay, the rest mass of the flavor eigenstates ν_l are given as the incoherent sum over the mass eigenstates

$$m^2_{\nu_l} = \sum_{i=1}^{3} |U_{li}|^2 m^2_{\nu_i}. \tag{1.3}$$

Here, the square of the absolute values of the matrix elements are pre-factors of the mass eigenvalues and thus the individual terms cannot cancel each other out.

Currently, the most stringent upper bounds to the antineutrino mass were set by studying the shape of a single-beta decay spectrum of tritium. In the laboratory based experiments carried out in Mainz and Troitsk, the tritium β-spectrum was studied to set upper limits of $2.3\,\mathrm{eV/c^2}$ [Lob03] and $2.05\,\mathrm{eV/c^2}$ [Kra05], respectively. A recent, even more refined analysis of both sets of data sets the upper limit of $m_{\bar{\nu}_e}$ to $2.0\,\mathrm{eV/c^2}$ [PDG10].

Future experiments such as KATRIN [Ang04] and MARE [Gat06b] are designed to improve this limit by one order of magnitude and reach sensitivities of $m_{\bar{\nu}_e} <$

$0.2\,\mathrm{eV/c^2}$. The underlying experimental method will be treated in greater detail in the next section.

1.3 Neutrino mass determination using single β-decays

The most sensitive known method to measure the electron neutrino mass is by observing the electron spectrum in nuclear β-decay.

$$\mathcal{N}(A,Z) \longrightarrow \mathcal{N}(A,Z+1) + e^- + \overline{\nu}_\mathrm{e}, \tag{1.4}$$

where A and Z are the mass and the atomic number of the parent nucleus, respectively. Following Fermi's golden rule, the differential decay rate in allowed β-decays is given by:

$$\frac{\mathrm{d}\Gamma}{\mathrm{d}E_\mathrm{e}} = S(E_\mathrm{e})F(Z',E_\mathrm{e})E_\mathrm{e}p_\mathrm{e}E_\nu p_\nu \tag{1.5}$$

Here $S(E_\mathrm{e})$ contains the nuclear matrix element, $F(Z',E_\mathrm{e})$ is the Fermi function, and E_e (E_ν) and p_e (p_ν) are the electron (neutrino) energy and momentum. The Fermi function accounts for the Coulomb interaction between the emitted electron and the remaining charge $Z'e$ and mainly effects the first part of the spectrum.

As the final nucleus $\mathcal{N}(A,Z+1)$ is much heavier than the final leptons, its kinetic energy is negligible and the total energy of the leptons is given by the mass difference of the parent and daughter nuclei. The neutrino energy is given by

$$E_\nu = Q - T, \tag{1.6}$$

where $T = E_\mathrm{e} - m_\mathrm{e}c^2$ is the kinetic energy of the electron and $Q = M_i c^2 - M_f c^2 - m_\mathrm{e}c^2$ is the total energy of the leptons minus the electron mass.

The Q-value of the process is the maximal kinetic energy of the electron if the neutrino is massless. On the other hand, if the electron neutrino has a mass m_{ν_e}, the maximal kinetic energy of the electron is $T_\mathrm{max} = Q - m_{\nu_e}$.

If a nonzero neutrino mass is taken into account, the energy available to the emitted electron is reduced. This mainly effects the spectral shape in the region towards the maximum energy and equation (1.5) becomes

$$\frac{\mathrm{d}\Gamma}{\mathrm{d}T} = S(E_\mathrm{e})F(Z',E_\mathrm{e})E_\mathrm{e}p_\mathrm{e}(Q-T)^2\sqrt{1-\frac{m_{\nu_\mathrm{e}}^2}{(Q-T)^2}}, \tag{1.7}$$

where $\mathrm{d}E_\mathrm{e} = \mathrm{d}T$ was used.

For a neutrino with zero mass, the line representing the number of events emitted with a certain energy intersects the energy axis at Q. A finite neutrino mass leads

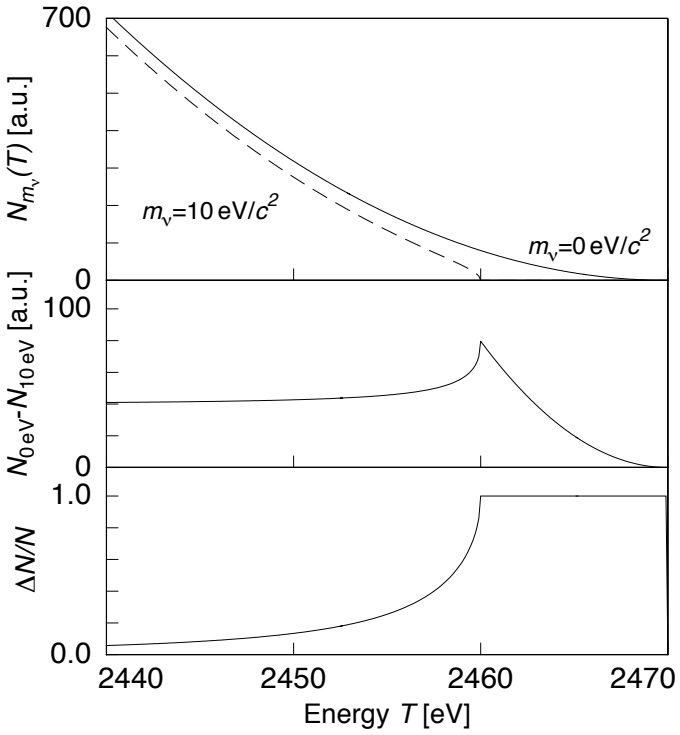

Figure 1.2 **Top:** Endpoint region of a β-spectrum with $Q = 2470\,\mathrm{eV}$ for a neutrino mass of $m_\nu = 0$ eV/c^2 (continous line) and $m_\nu = 10$ eV/c^2 (dashed line). **Middle:** Absolute difference of the two spectra. **Bottom:** Relative difference of the two spectra.

to a deviation in the spectrum and the endpoint lies at $E = Q - m_{\nu_e}c^2$ as illustrated in the top panel of figure 1.2 for $m_\nu = 0$ eV/c^2 and $m_\nu = 10$ eV/c^2.

The fraction of events in the most relevant energy interval ΔT close to the endpoint of the spectrum is

$$F(\Delta T) = \frac{1}{N} \int_{Q-\Delta T}^{Q} N(T, m_{\nu_e} = 0)\mathrm{d}T \propto \left(\frac{\Delta T}{Q}\right)^3 . \tag{1.8}$$

The fraction of counts most useful in revealing the neutrino mass decreases with the third power of the end-point energy. This extremely tiny amount of events can be emphasized by choosing β-decaying isotopes with very low endpoint energies.

Two isotopes that meet this requirement are under current investigation: the radioactive hydrogen isotope tritium (^{3}H) with $Q = 18.6\,\mathrm{keV}$ and rhenium (^{187}Re) with an end-point energy of 2.47 keV.

For investigations of the neutrino mass in the eV or sub eV range, only events within the last few eV of the spectrum contain the necessary information. Applying (1.8) to tritium, assuming a neutrino mass of the resulting useful fraction of events within the last 10 eV of the spectrum is only 3×10^{-10}, for rhenium it is 1×10^{-7}. Both of these numbers are quite small and clearly show that handling a large number of total events is essential for all direct neutrino mass experiments.

Currently, three approaches to precisely measure the electron spectrum of the

mentioned isotopes are followed by the projects KATRIN (KArlsruhe TRItium Neutrino), MARE (Microcalorimeter Arrays for a Rhenium Experiment) and Project 8 . The techniques used in KATRIN and MARE have already set upper bounds to the neutrino mass of $2\,\mathrm{eV/c^2}$ in the Mainz/Troitsk experiments [PDG10] and $15\,\mathrm{eV/c^2}$ at 90 % confidence level in the Mibeta experiment [Sis04], respectively, while Project 8 follows a new concept and still needs to provide a proof of principle result.

The improvement of the present limits by one order of magnitude would probe the cosmologically relevant neutrino mass range and distinguish degenerate neutrino mass scenarios from the hierarchical ones.

KATRIN

The **KA**rlsruhe **TRI**tium **N**eutrino (KATRIN) experiment [Ang04] aims at directly measuring the neutrino mass by investigating the kinematics of the tritium β-decay with a sensitivity of $0.2\,\mathrm{eV/c^2}$. This experiment is presently in the construction phase and a completed system is planned for 2012. It is based on the principle of a so-called MAC-E filter[2][Lob85]. In the spectrometer, the electrons are isotropically emitted in a beta source and are magnetically guided into a broad beam flying almost parallel to the magnetic field lines generated in a large volume of $1250\,\mathrm{m^3}$. This beam of electrons runs against an electrostatic potential. Only the electrons overcoming this threshold will be reaccelerated and collimated onto the detector. The MAC-E filter, therefore, acts as an integrating high-energy pass filter. The tritium source planned for the KATRIN experiment will emit a flux of $2 \times 10^{10}\,\mathrm{Bq}$. Only a fraction of about 2×10^{-7} of the emitted electrons will be guided to the main spectrometer, leading to an event rate in the detector of a few Hertz depending on the retarding potential.

A problem present in this experimental approach is the use of a source external to the detector. This fact allows transitions to excited states of the produced daughter atom, the molecule it is bound in or the substrate it is bound to. In the detector, this decay will not be distinguishable from a decay to the ground state and thus gives rise to a reduced kinetic energy of the emitted electrons – a signature similar to the one caused by a nonzero neutrino mass.

One of the advantages of the KATRIN experiment is the high energy resolution of the order of 1 eV which can be achieved. A second advantage is the high pass filter characteristic of the experiment, which makes it possible to select only those electrons very close to the endpoint energy and thus concentrating on the most relevant part of the β-spectrum. This in turn, permits the use of a high activity source and high statistics can be achieved in a reasonable time.

[2]Magnetic Adiabatic Collimation with an Electrostatic filter

MARE

The MARE project – **M**icrocalorimeter **A**rrays for a **R**henium **E**xperiment – is based on the calorimetric measurement of the rhenium β-spectrum using low temperature detectors [Gat06b]. The goal of MARE is to achieve a sensitivity to the neutrino mass which would compete with the KATRIN experiment and potentially exceed it. The experiment is complementary, based on totally different experimental techniques and facing different experimental challenges.

MARE will study the decay of ^{187}Re. This isotope demonstrates one of the lowest Q values in nature at $Q = 2.47\,\mathrm{keV}$. The low endpoint energy will lead to about 400 times higher fraction of events in the relevant region around the endpoint compared to decay events from tritium. In this approach, the source is embedded inside the detector. Only the neutrinos will be able to escape from the detector, so this leads to a calorimetric measurement of the desired quantity, namely the total decay energy minus the energy carried away by the neutrino $Q - E_\nu$.

Low temperature micro-calorimeters operating at temperatures below $T = 100\,\mathrm{mK}$ are proposed as detectors. The underlying general principle of a calorimeter is pictured in Figure 1.3. The detector consists of an absorber suited for the particles to be detected and is strongly coupled to a thermometer which precisely monitors the absorber's temperature. Together they form the calorimeter, which is weakly coupled to a thermal bath.

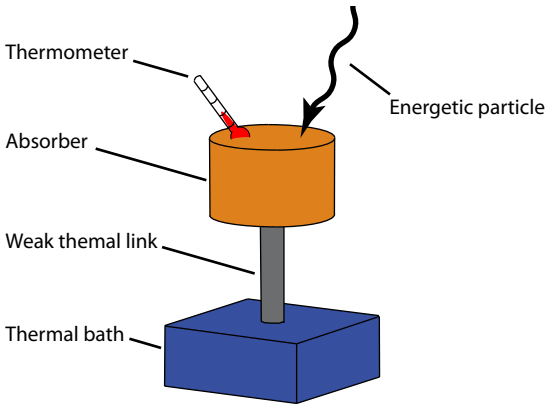

Figure 1.3 Basic principle of a calorimetric detector.

The energy E deposited in the absorber is determined via the temperature rise of the detector of given heat capacity C_{tot}

$$\delta T \cong \frac{E}{C_{\mathrm{tot}}}. \tag{1.9}$$

The signature of such an event is a fast temperature rise followed by the relaxation back to the temperature of the thermal bath. The decay time is determined by the

total heat capacity C_{tot} and the thermal conductance G involved:

$$\Delta T(t) \propto \frac{E}{C_{\mathrm{tot}}} e^{-t/\tau} \quad \text{with} \quad \tau = \frac{C_{\mathrm{tot}}}{G}. \tag{1.10}$$

The first phase of MARE is planned to start in 2010. In the Milano group a modular design was proposed where the first module consisting of 72 detectors based on semiconductor thermistors, provided by the Goddard (NASA) group, is being built to reach a neutrino-mass limit of $5\,\mathrm{eV/c^2}$ within a measuring time of two years. The experiment could then be extended using further modules, to a total of 288 detectors [Fer09].

In order to reach a sensitivity on the level of $0.2\,\mathrm{eV/c^2}$ in the second phase of MARE, intense detector research and development is needed. The present work is located within this framework, developing a metallic magnetic calorimeter with a fast response time and high energy resolution for the spectroscopy of the rhenium beta decay.

Project 8

This novel approach of investigating the neutrino mass was presented only recently [Mon09]. It is a new concept using electron energy spectroscopy in which the coherent cyclotron radiation emitted by an energetic electron in a magnetic field is detected. For mildly relativistic electrons, like those of the tritium decay, the cyclotron frequency will be shifted and this will allow the extraction of the electron energy from the spectrum of the emitted radiation. A conceptual study of this approach has been carried through and is presented in the reference given, but the systematics of this new technique are currently still unknown.

1.4 Neutrino mass sensitivity

In the present section, a discussion of the neutrino mass sensitivity using a calorimetric approach will be given. In this discussion several experimental configurations will be addressed to estimate the fundamental experimental sensitivity for such an experiment. For the moment, the details of a low temperature micro-calorimeter are not important. The detector will simply be assumed to be an energy dispersive device in which released energy leads to a pulse shaped signal with a fast rise time in the microsecond range and a decay that is approximately a thousand times slower – in the millisecond range. The amplitude of the pulse shaped signal is proportional to the energy deposited in the calorimeter.

In [Nuc09], the sensitivity is estimated using Monte Carlo methods. There the outcome of a large set of events is simulated for different experimental conditions taking into account the detector response, unresolved pileup and background. From each

set a spectrum is generated and fitted using a parameterized theoretical spectrum. In the theoretical spectrum, the same effects as discussed above were incorporated, in addition to the response function of the detector and the pileup effect the existence of a constant background were incorporated.

Within this work, a complementary approach to estimate the neutrino mass sensitivity is presented. At first, this is done using a simple statistical argument. In due course an imperfect detector will be considered by including a gaussian line shape of the detector. Furthermore, the effect of unresolved pulse pileup and its influence on the neutrino mass sensitivity will be discussed as well as the influence of unavoidable background events. In addition to previous discussions, the energy interval around the endpoint which needs to be analyzed to achieve the best sensitivity is discussed.

The outcome of the studied sensitivity for the given parameter space agree very well with the ones presented in [Nuc09]. This agreement is true both, for the qualitative trends, as well as for the quantitative results. The observations made from this study, are taken as a guideline for the detector development, which is discussed in the remainder of the thesis.

1.4.1 Statistical sensitivity

In order to discuss the sensitivity to the neutrino mass m_ν upper bound, which is considered here to be significantly smaller than the energy resolution of the detector, the number of counts near the endpoint of the measured β-spectrum need to be compared to the number of events in the same region assuming a vanishing neutrino mass. This sensitive endpoint region is illustrated in figure 1.2. The number of events within an energy interval ΔE below the endpoint Q of a β-spectrum is given by

$$F_{\Delta E}(m_\nu) = \int_{Q-\Delta E}^{Q} N_\beta(E, m_\nu) dE, \tag{1.11}$$

where $N_\beta(E, m_\nu)$ is the electron energy spectrum of the β-decay for a given neutrino mass m_ν. For further reference the total number of counts N_{tot} is defined as

$$N_{\mathrm{tot}} = \int_{0}^{Q} N(E, m_{nu}) dE \ . \tag{1.12}$$

The signal s corresponding to a nonzero neutrino mass is the difference between the number of events for a vanishing and no-zero neutrino mass

$$s = |F_{\Delta E}(0) - F_{\Delta E}(m_\nu)|. \tag{1.13}$$

In case of a perfect detector and negligible pileup and background, the precision of the measurement will only be compromised by the statistical uncertainty. Assuming Poissonian statistics and a large number of counts, the noise n is given by the square root of the number of counts expected in the interval ΔE below the endpoint Q for zero neutrino mass:

$$n = \sqrt{F_{\Delta E}(0)}. \tag{1.14}$$

From this it is possible to extract a sensitivity for the neutrino mass. A confidence level (C.L.) of 90% can be achieved when the signal to noise ratio s/n equals 1.7. In order to better understand the requirements to reach such a sensitivity, a simplified spectral shape as well as a Taylor expansion is used in the following.

A good high energy description for the spectral shape of the rhenium decay is given by [Dvo09]:

$$N_\beta(E, m_\nu) \simeq \frac{3}{Q^3}(Q-E)^2\sqrt{1-\frac{m_\nu^2}{(Q-E)^2}}, \tag{1.15}$$

In order to find the signal to noise ratio (1.15) needs to be integrated near the endpoint. Integration and second order Taylor expansion leads to

$$F_{\Delta E}(m_\nu) \simeq \left(\frac{\Delta E}{Q}\right)^3\left(1-\frac{3m_\nu^2}{2\Delta E^2}+\frac{3m_\nu^2}{8\Delta E^4}\right) \tag{1.16}$$

Using just the first order of (1.16) and solving for m_ν it is possible to get a first impression of the requirements on a calorimetric measurement of a β-spectrum which is sensitive at the 90 % confidence level $\Sigma_{m_\nu}^{90\%}$:

$$\Sigma_{m_\nu}^{90\,\%} \simeq \left[\frac{4}{9}\left(\frac{s}{n}\right)^2\frac{Q^3\Delta E}{N_{\mathrm{tot}}}\right]^{1/4}, \tag{1.17}$$

where $N_{\mathrm{tot}} = N_{\mathrm{det}} A_\beta t_M$ is the product of the total number of detectors N_{det}, A_β is the single pixel activity and t_M is the measurement time. With this general approach it is possible to understand some dependencies as well as the order of magnitude of the involved quantities. The two most striking facts of this simple analysis are, that the sensitivity to an upper bound $\Sigma_{m_\nu}^{90\%}$ for m_ν is increasing with the fourth root of the total number of counts $N_{\mathrm{tot}} = A_\beta N_{\mathrm{det}} t_M$. Equation 1.17 also suggests that under these perfect conditions it is beneficial to reduce the analyzed interval ΔE as this will also restrict the neutrino mass. Evaluating (1.17) at a 90% confidence level, with an energy interval of $\Delta E = 10\,\mathrm{eV}$, an endpoint energy of $Q = 2470\,\mathrm{eV}$ and a total number of 10^{14} events leads to a neutrino mass sensitivity of 0.21 eV. Note that the number of events within the analyzed region ΔE would be roughly six million. As mentioned before, this approach does not yet fully represent the realistic

experimental conditions. In the following sections two detector development goals, namely high energy resolution and fast detector response, will be addressed and their influence on the sensitivity to the neutrino mass will be discussed. Additionally, unwanted background is included in the discussion of the neutrino mass sensitivity.

1.4.2 Detector linewidth

For any energy resolving detector there are limits on the energy resolution and the response time. The low temperature detectors discussed within this work are among the highest resolving devices spanning a wide range of detectable energies. Currently, the best performing metallic magnetic calorimeter has a resolving power greater than 2000 for soft X-rays showing an energy resolution of $\Delta E_{\mathrm{FWHM}} = 2.7\,\mathrm{eV}$ at an energy of 5.9 keV [Fle09a]. Clearly, a non-perfect detector response, usually characterized by a gaussian with a full width at half maximum ΔE_{FWHM}, will effect the entire spectrum recorded, in particular smearing out the crucial endpoint region of the β-spectrum. This will also affect the sensitivity to the neutrino mass. Additionally, the interval ΔE around the endpoint being investigated will depend on the quality of the detector.

In the signal to noise ratio an imperfect detector impacts both the signal and the noise. As the energy resolution gets worse, the difference between the integrated number of counts for a zero and a nonzero neutrino mass in a certain interval around the endpoint decreases.

The results presented were achieved using numerical calculations. Here, the theoretical spectrum was convoluted with a gaussian detector response function of a given width. Numerical calculations verify what was stated before, namely, that the analyzed energy interval ΔE should be small. However, the interval should not be smaller than the actual neutrino mass. This seems plausible looking at figure 1.2, which shows a decreasing signal for intervals smaller than m_ν. Including the detector linewidth not only changes the signal to noise ratio but also the optimal interval to be analyzed. For tritium experiments, these dependencies were treated and it was found that an interval of $\Delta E \approx 2\Delta E_{\mathrm{FWHM}}$ centered near the extrapolated β endpoint energy should be used [Sim81]. For the presented numerical calculations this aspect is studied. The interval was varied to achieve an optimal signal to noise ratio for a given detector linewidth and experimental conditions, i.e. pileup and background rates.

1.4.3 Unresolved pulse pileup

For a neutrino mass measurement as discussed in this work the entire spectrum is measured by means of a calorimeter or an array of them. In such a detection scheme each individual event is represented by a pulse-shaped signal with a finite rise time

τ_0. Pairs of events that occur within a very small time interval τ_R, which are in the order of the detector's rise time will not be resolved in time as the resulting detector signal can hardly be distinguished from a single event caused by the sum of the energies of the two absorbed particles. This gives rise to the phenomenon of *unresolved pileup*. The energy information is, therefore, lost and in particular it could occur that two low energy events will be summed up and contribute one count in the region close to the endpoint, contaminating the spectral shape in this crucial interval.

The unresolved pileup spectrum is given by the convolution of the β-spectrum with itself, weighted by the factor P, which is the fraction of unresolved pileup:

$$N_{\mathrm{pu}}(E) = P \int_0^E N_\beta(E') N_\beta(E - E') dE'. \tag{1.18}$$

For a Poissonian time distribution, the fraction of unresolved pileup events will be given by

$$P = 1 - e^{-A_\beta \tau_{\mathrm{R}}} \simeq A_\beta \tau_R, \tag{1.19}$$

where τ_{R} is the pulse-pair resolving time. The probability of having an unresolved pileup of more than two events is negligible, therefore, such events are not taken into account. The pileup spectrum can be calculated using (1.18) and the approximated spectral shape (1.15). For this purpose we want to neglect the gaussian detector response as well as a nonzero neutrino mass as both will have little effect on the pileup spectrum

$$N_{\mathrm{pu}}(E) = P \frac{1}{Q} \left[9 \left(\frac{E}{Q}\right) - 18 \left(\frac{E}{Q}\right)^2 + 12 \left(\frac{E}{Q}\right)^3 - 3 \left(\frac{E}{Q}\right)^4 + \frac{3}{10} \left(\frac{E}{Q}\right)^5 \right]. \tag{1.20}$$

near the endpoint Q. Figure 1.4 shows a logarithmic plot of the β-spectrum given by (1.15) and the pileup spectrum in comparison. As expected, the convoluted spectrum is extends to higher energies than Q. From figure 1.4 as well as from (1.20), it can be seen that the pileup spectrum only shows a weak energy dependence near the endpoint such that in a first order approximation this contribution is constant in energy.
Integrating the pileup spectrum in an interval ΔE around the endpoint will give the corresponding contribution to the noise:

$$F_{\Delta E}^{\mathrm{pu}} = P \frac{1}{20} \left[6 \left(\frac{\Delta E}{Q}\right) + 15 \left(\frac{\Delta E}{Q}\right)^2 + 20 \left(\frac{\Delta E}{Q}\right)^3 - 15 \left(\frac{\Delta E}{Q}\right)^4 - 6 \left(\frac{\Delta E}{Q}\right)^5 - \left(\frac{\Delta E}{Q}\right)^6 \right]. \tag{1.21}$$

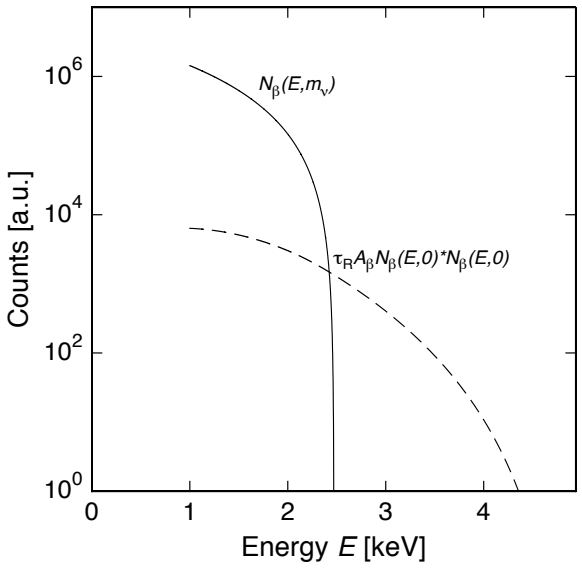

Figure 1.4 Beta spectrum as given in 1.15 and in comparison to a unresolved pileup spectrum for a pileup rate of $P = 10^{-6}$.

For an interval of $\Delta E = 10\,\mathrm{eV}$ and $P = 1 \times 10^{-6}$ a fraction of about 1×10^{-9} events are falsely counted in this region in comparison to a fraction of about 6.6×10^{-8} events which really occur in this energy range.

1.4.4 Background

For completing the discussion of the signal to noise ratio near the endpoint of the rhenium β-spectrum it is necessary to address one more noise contribution, namely the background. In the present discussion, an energy independent background event rate will be assumed. It is possible to parametrize this contribution by

$$F_{\Delta E}^{\mathrm{bg}} = \xi \Delta E \frac{1}{A_\beta}, \tag{1.22}$$

where ξ is the average background counting rate per unit energy for a single detector. The background will contribute to the noise in a similar manner as the pileup. Both noise sources show a rather flat spectrum around Q. It is therefore interesting to note that the increase of any of the two quantities – pileup-rate or background rate – is interchangeable with the other. Nevertheless, the two noise sources will be treated separately as they involve completely different needs with respect to detector development. As this work will primarily focus on the development of a calorimeter for this specific experiment, the sources of background will not be discussed in great detail, rather the background rate will just be assumed as a parameter. A possible value of the background rate could be taken from, for example the value that was observed in recent experiments. In the MANU experiment for example [Gat00], which took place under normal laboratory conditions and not in an underground

laboratory, an energy independent background rate of 3×10^{-4} events/eV/day was measured around Q. This translates to about 1 event per year in an energy interval of 10 eV.

The amount of background will mostly be set to a value comparable to recent experiments of this kind.

Comparing this to the previous pileup discussion, the background contribution in an energy interval of 10 eV, assuming a β-activity of $A_\beta = 1$ Bq, will be of the order of $3 \times 10^{-4} \times 10/86400 = 3.4 \times 10^{-8}$. Astonishingly enough, this would be about as much as 50% of the expected electron count rate in the same energy interval. Therefore, achieving low background conditions will be of utmost importance.

Of course a detector with the fastest possible pulse pair resolving time and a setup with the lowest achievable background is wanted. From this observation, it is evident that unresolved pulse pileup and background have interchangeable effects on the neutrino mass sensitivity. In a first order approach, reducing the background rate by a factor of 10 will automatically allow an increase of the beta activity A_β or an acceptance of a slower rise time by the same factor of 10, keeping the sensitivity at the same level. The higher activity would reduce the number of detectors or the total measuring time needed.

Although no detailed studies of background conditions or low background environments have been undertaken within this work, this discussion already reveals the importance of the shielding the experimental apparatus will require. For future design considerations the material choice in the vicinity of the experiment as well as a possible location of the experiment in a low background underground laboratory will need to be addressed.

1.4.5 The optimal interval

The neutrino mass sensitivity depends on the quantities discussed above, namely total statistics, rate of unresolved pileup and background. Furthermore, the method of data analysis will be important. So far in this discussion the approach of counting the number of events in a given energy interval around the endpoint was presented. For this method, choosing the interval around the endpoint is crucial. The studied interval can be parametrized in terms of the full-width at half-maximum energy resolution of the instrumental linewidth of the detector, setting the interval to $\Delta E = b\Delta E_{\mathrm{FWHM}}$, where b can be varied. In earlier discussions of this topic [Sim81] this interval was chosen to have the width of two times the full width at half maximum. In [Nuc09] this interval size is also chosen.

Throughout the numerical calculations made in this work, this topic has been addressed as well. In the presented calculations the interval was centered at Q and extended to energies below and above $[Q - b\Delta E_{\mathrm{FWHM}}; Q + b\Delta E_{\mathrm{FWHM}}]$.

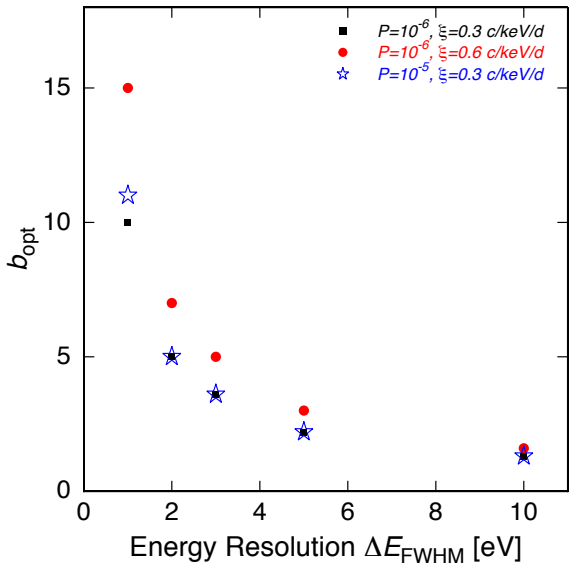

Figure 1.5 Dependence of the optimal energy interval $\Delta E = b_{\mathrm{opt}} \Delta E_{\mathrm{FWHM}}$ to be analyzed around Q.

Figure 1.5 shows the dependence of the optimally chosen b_{opt} on the energy resolution ΔE_{FWHM} for different experimental conditions, where the unresolved pileup rate P and the background ξ are varied. It can be seen that for high levels of background or unresolved pileup the size of the optimal interval becomes independent of the detector's energy resolution ΔE_{FWHM}. In the limit of an energy resolution that is by far larger than the neutrino mass and for little background or pileup rate, an optimal interval is found where b is between 0.7 and 0.9, corresponding to an interval size very close to the one suggested by Simpson.

In the limit of detectors with an energy resolution comparable to the neutrino mass to be determined, the approach chosen may not be justified anymore. In that case no clear b can be found to maximize the signal to noise ratio and b is getting large. In this scenario, the functional dependence on b becomes very flat for $b \gtrsim 4$, which suggests that an additional criterium to optimize the interval needs to be found. It may be beneficial to choose a different method of analysis, like fitting, to extract the neutrino mass from the measured spectrum.

1.4.6 Results

At this point, all of the discussed noise contributions can be combined to estimate the neutrino mass sensitivity. The resulting signal to noise ratio, including all discussed noise contributions, takes the form:

$$\frac{s}{n} = \sqrt{A_\beta N_{\mathrm{det}} t_{\mathrm{M}}} \frac{F_{\Delta E}(m_\nu) - F_{\Delta E}(0)}{F_{\Delta E}(0) + F_{\Delta E}^{\mathrm{pu}} + \xi \Delta E / A_\beta}. \tag{1.23}$$

Assuming a Poissonian distribution a 90% confidence level is tested whenever the signal to noise ratio is equal to $s/n = 1.7$. In the following discussion of different

experimental scenarios a 90% confidence level is always considered.

First, the dependence of the sensitivity to the total number of counts will be presented. Figure 1.6 illustrates the importance of the total number of counts N_{tot} acquired for a neutrino mass measurement. Data for different energy resolutions and unresolved pileup rates $P = A_\beta \tau_{\mathrm{R}}$ are depicted. The background rate was neglected for these computations as it is interchangeable with unresolved pileup. The dashed line is just a guide to the eye and represents a functional dependence proportional to $N^{-1/4}$ as suggested by the purely analytic approach (1.17), which appears to hold for a large variety of parameters.

In order to reach a sensitivity that is in the sub eV range or even below the limit of 0.2 eV, a total number of counts of the order of 10^{14} is needed. Already from this graph, it is appreciable that the detector performance expressed in resolvable pileup and energy resolution, will be crucial to such a measurement. Equally, the suppression of background events in the studied energy band will be of vital importance, but for clarity, is not included in this graph. A detector with an energy resolution of $\Delta E_{\mathrm{FWHM}} = 10\,\mathrm{eV}$ and an unresolved pileup rate of $P = 1 \times 10^{-6}$ could undercut the important $2\,\mathrm{eV/c^2}$ sensitivity limit with acquiring just over 10^{10} events. According to the $N_{\mathrm{tot}}^{-1/4}$ dependence the $0.2\,\mathrm{eV/c^2}$ level would require about four orders of magnitude more events.

From the previous section it is evident that a high number of counts is necessary, therefore in the following discussion a total number of $N_{\mathrm{tot}} = 10^{14}$ events is assumed to study the dependence of the sensitivity on energy resolution, detector rise time and background rates.

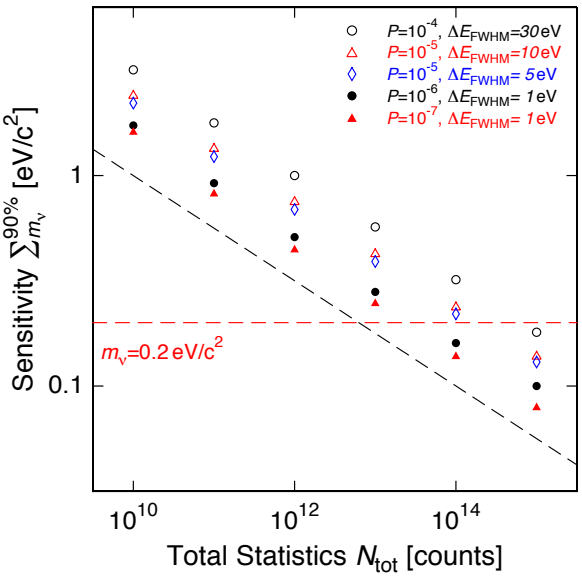

Figure 1.6 Dependence of the neutrino mass sensitivity on the total number of events for different values of energy resolution ΔE_{FWHM} and fraction P of unidentified pileup. No background events were assumed. The dashed line is a guide for the eye and represents a functional dependence of $N_{\mathrm{tot}}^{-1/4}$.

Figure 1.7 shows the sensitivity to the neutrino mass as a function of the detector energy resolution, for different unresolved pileup fractions. In most scenarios shown, the background was taken into account but the rate was chosen to be as low as $\xi = 0.003\,\text{events/keV/d}$. This emphasizes the effect of unresolved pileup as in this limit one needs to assume that the effect of unresolved pileup dominates.

These results show that the unresolved pileup rate should be as low as possible. Reducing this rate for a $\Delta E_{\text{FWHM}} = 1\,\text{eV}$ detector from 10^{-4} to 10^{-7} results in an improvement in the sensitivity by a factor of two. This motivates the necessity for a detector with a fast rise time. The energy resolution of the detector is also important, but it can clearly be seen, that for high probabilities of unresolved pileup $P > 10^{-5}$ the dependence of the sensitivity on energy resolution is rather flat. Both observations demonstrate that for sensitivities lower than 0.2 eV the deployed detectors should perform with energy resolutions $\Delta E_{\text{FWHM}} \leqslant 10\,\text{eV}$ and pileup rates $P = A_\beta \tau_{\text{R}} \leqslant 10^{-5}$.

For comparison two computed data sets are shown using background event rates of 0.03 events/keV/d and 0.3 events/keV/d, respectively. The latter rate has been measured by the MANU experiment under normal laboratory conditions. In this case a fast detector response was assumed and the dependence of the sensitivity on the energy resolution is nearly flat for $\Delta E_{\text{FWHM}} < 10\,\text{eV}$. This scenario is roughly equivalent to a 100-fold pileup rate and underlines the importance of both, a low background rate as well as a fast detector response.

The observations made so far, will be a guideline for the detector development aiming at an experiment using low temperature calorimeters for a neutrino mass measurement.

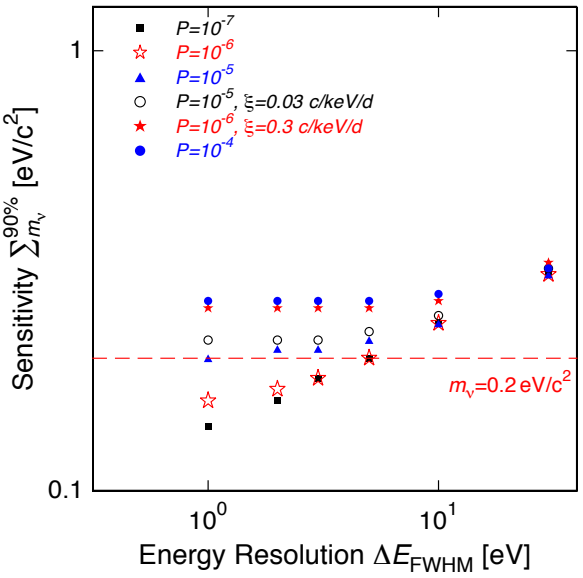

Figure 1.7 Dependence of the statistical sensitivity to neutrino mass on the energy resolution ΔE_{FWHM} of the detector. For the data shown a total number of counts of $N_{\text{tot}} = 10^{14}$ was assumed. If not noted otherwise the background rate was set to a negligible level of $\xi = 0.003\,\text{events/keV/d}$.

1.5 Conclusion – Outline of a neutrino mass experiment

In this chapter a brief outline of neutrino physics was given, motivating laboratory based neutrino mass measurements. The limits of the sensitivity to the neutrino mass using a calorimetric approach were discussed in some detail. Two possible scenarios for a neutrino mass experiment using low temperature calorimeters are given, followed by a brief summary of the important steps in detector development that will be discussed in the remainder of this thesis.

A suggested experiment to reach a neutrino mass sensitivity of $0.2\,\mathrm{eV/c^2}$ would need to acquire at least 10^{14} events. Detectors performing at an energy resolution of $\Delta E_{\mathrm{FWHM}} = 5\,\mathrm{eV}$ and with a rate of unresolved pileup of $P = A_\beta \tau_\mathrm{R} = 5 \times 10^{-6}$, a signal rise time of $\tau_0 \leqslant \tau_R$, and a background of $0.03\,\mathrm{events/keV/d}$ would require $630,000$ detector years of measuring time. Of course an experiment of this scale would require a large number of detectors of the order of $10,000$ to $100,000$. As these numbers appear challenging in all respects, another scale of such an experiment could be outlined as follows. As the current limit on the neutrino mass is given as $2\,\mathrm{eV/c^2}$, any improvement of this will be much appreciated. A calorimetric experiment to fulfill this would for example be given by measuring 10^{11} events at a rate of 5 Bq per detector with detectors performing with an energy resolution of 10 eV and a pulse pair resolving time of $10\,\mu\mathrm{s}$. Here a sensitivity of $1.5\,\mathrm{eV/c^2}$ can be reached assuming the background of the MANU experiment of $0.3\,\mathrm{events/keV/d}$. Such an experiment would require just over 600 detector years, so for example this experiment could be carried out with 1000 detectors and reach the mentioned upper limit in under one year of measuring time. Increasing the total number of counts by one order of magnitude, one could set an upper limit of $0.85\,\mathrm{eV/c^2}$. For example, an array of 600 detectors could be deployed for one year to gain the needed statistics for the $1.5\,\mathrm{eV/c^2}$ limit. Once this is reached the experiment could be expanded by additional modules to 6000 detectors to acquire the needed statistics for reaching the $1\,\mathrm{eV/c^2}$ limit. Both sketched scenarios point out the most important requirements a detector array for a neutrino mass measurement must fulfill:

1. Fast rise time are mandatory. The detector response should allow a pulse-pair resolving time to be in the order of 10^{-6}.
2. Energy resolution $\Delta E_{\mathrm{FWHM}} \leqslant 10\,\mathrm{eV}$.
3. A feasible readout scheme for the large number of required channels.
4. Detector fabrication should be based on micro-fabrication techniques in order to build the required number of detectors and reach a good reproducibility.
5. The environment of the experiment should provide a background count rate which is as low as possible.

Most of these topics will be addressed within the following chapters. The first two topics will be treated in great detail, the theoretical background of metallic magnetic calorimeters will be discussed in chapter 2, where the fundamental limitations of these techniques will also be discussed. The development of a detector specifically for this application will be discussed in chapter 4.

Chapter 2

Theoretical and Experimental Background

2.1 Principles of Metallic Magnetic Calorimeters

In this chapter the underlying principles of metallic magnetic calorimeters (MMCs) are discussed. The detection scheme is described and general requirements as well as limits on the energy resolution are addressed.

The schematic of a calorimeter is shown in Figure 2.1. The detector consists of an absorber suited for the particles to be detected. It is strongly coupled to a thermometer, which precisely monitors the absorber's temperature. To allow a return to thermal equilibrium after the absorption of energy, the calorimeter is weakly linked to a thermal bath.

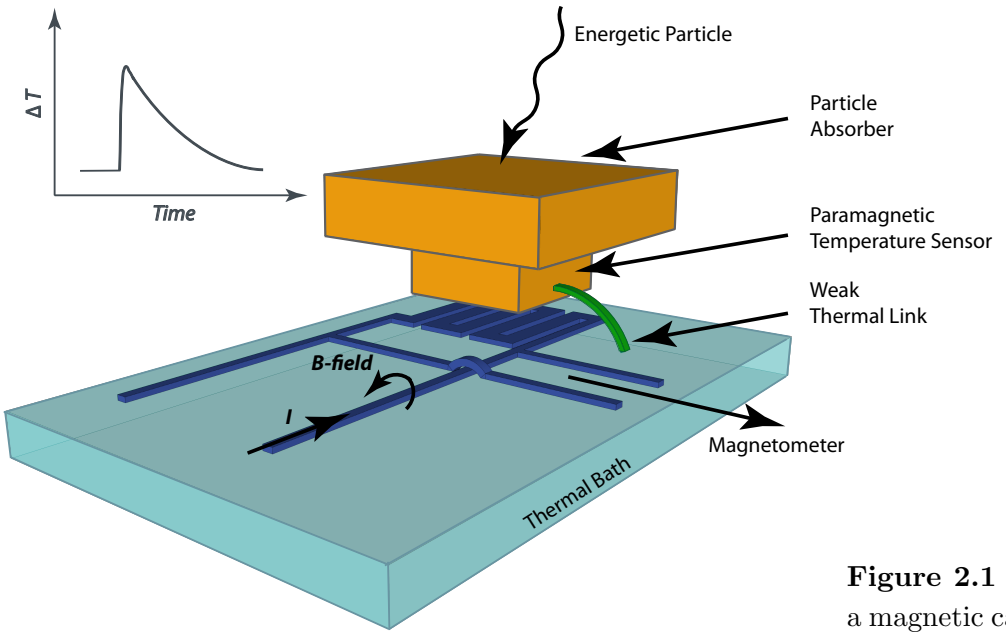

Figure 2.1 Sketch of a magnetic calorimeter.

The absorption of a particle corresponds to an energy input δE into the calorimeter, which leads to a temperature rise according to

$$\delta T = \frac{\delta E}{C_{\mathrm{tot}}}. \tag{2.1}$$

For a known total heat capacity C_{tot} of the calorimeter the energy deposited in the absorber can thus be determined via the temperature rise δT.
A signature of such an event can be arranged to be a fast temperature rise in the thermometer followed by a slower relaxation to the temperature of the thermal bath. In first order, the rise and decay time can be described as a simple exponential law

$$\Delta T(t) = \delta T(-e^{-t/\tau_0} + e^{-t/\tau_1}). \tag{2.2}$$

Here τ_0 is the intrinsic rise time of the detector and $\tau_1 = C_{\mathrm{tot}}/g_{\mathrm{b}}$ is the thermal decay time given by the ratio of the total heat capacity and the thermal conductance g_{b} to the thermal bath.

Currently, mainly three types of low temperature particle detectors have been developed for soft X-rays:

- Semiconductor Thermistors [McC05],
- Superconducting Transition Edge Sensors (TES) [Irw05],
- Metallic Magnetic Calorimeters (MMC) [Fle05].

For completeness Superconducting Tunnel Junctions (STJs) [Twe88] should be mentioned, that are not widely developed any longer. Also Microwave Kinetic Inductance Detectors (MKIDs) [Day03] are promising candidates for high resolution detectors. They are especially suited for the low energy regime and can easily be integrated into large detector arrays.

The measurement principles of all differ in the type of the thermometers. Both the semiconductor thermistor as well as the transition edge sensor rely on a strong temperature dependence of the electrical resistance. The first type exploits the electron conduction of highly doped semiconductors at low temperatures. The second type is operated at the metal-to-superconductivity transition. In a narrow temperature interval, the dependence of the resistance on the temperature T is very steep leading to a high temperature-to-resistance-transfer coefficient. In this thesis the last of the listed detector types is utilized and is discussed in detail in the following.

In a magnetic calorimeter the temperature is monitored based on the temperature dependence of the magnetization of a paramagnetic sensor. The sensor is placed in

a weak magnetic field and operated in a temperature range where the magnetization M shows Curie-like behavior

$$M \propto \frac{1}{T}. \tag{2.3}$$

The process of particle detection can be understood in the following way: the absorption of an energetic particle with energy δE causes a rise in temperature δT of absorber and sensor. The accompanied decrease in magnetization δM of the sensor can be read out inductively as a change of flux $\delta\Phi$ in a pick-up loop

$$\delta\Phi = \frac{\partial M}{\partial T}\,\delta T = \frac{\partial M}{\partial T}\,\frac{\delta E}{C_{\mathrm{tot}}}. \tag{2.4}$$

This flux change can be monitored by a low-noise dc-SQUID magnetometer. Herewith, a highly resolved measurement of the temperature of the sensor and hence the energy content of the calorimeter is feasible.

The use of paramagnetic temperature sensors for calorimetric particle detection was pioneered by Bühler and Umlauf in the 1990s [Büh88, Büh93, Büh94], who studied detector prototypes based on dielectric paramagnets. Results obtained with these low temperature calorimeters were very promising, showing large signals and a good noise performance. The downside of the dielectric host, however, is the intrinsically slow signal rise time. This is given by the relatively weak spin–phonon coupling at low temperatures in dielectric materials. This problem was addressed in [Ban93] suggesting the use of metals as host material for the paramagnetic ions. Due to the much stronger electron–spin coupling the metal host allows for a faster magnetization change and thus higher count rates.

This approach was further developed and handmade detectors for X-ray spectroscopy were built that showed energy resolutions down to $\Delta E_{\mathrm{FWHM}} = 2.7\,\mathrm{eV}$ at X-ray energies of 5.9 keV [Fle09b]. For the development of detector arrays, micro-fabrication techniques were explored and different groups started the development of new geometries which have become accessible with these new techniques. This required reproducing the well understood thermodynamic quantities of bulk materials such as niobium, gold and gold-erbium alloys in deposited thin films [Zin04, Hsi08, Bur08].

With these new fabrication techniques the same level of energy resolution was proven. At X-ray energies of 5.9 keV energy resolutions of $\Delta E_{\mathrm{FWHM}} = 2.8\,\mathrm{eV}$ [Fle09a] and $\Delta E_{\mathrm{FWHM}} = 3.3\,\mathrm{eV}$ [Ban09] were demonstrated with fully micro-structured detectors opening a vast field of new geometries and hence applications. However, this detection method is believed to achieve energy resolutions even below $\Delta E_{\mathrm{FWHM}} = 1\,\mathrm{eV}$ which would open for example new methods for chemical analysis.

2.2 Sensor material Au:Er

In this section a brief description of the paramagnetic sensor material Au:Er is given. A more detailed description can be found elsewhere, e.g. [Fle03, Fle05].

At concentrations below a few percent of erbium in gold, the two metals form a solid solution [Rid65]. Here Er^{3+}-ions substitute the Au^{+} ions at their regular lattice sites. The erbium's $4f$ electron shell is located deeply inside the erbium ion and is only partly filled. This causes the formation of a strong magnetic moment that interacts only weakly with the conduction electrons and the crystal field. The weak interaction of the erbium ion with its surrounding allows to determine the magnetic moment from the angular momenta J, L, S that can be derived according to Hund's rules. Above 100 K the magnetization of dilute Au:Er alloys can be described by the magnetic moment $\mu = g_{\mathrm{J}} J$ of the erbium ions with a Landé factor $g_{\mathrm{J}} = 1.2$ and the total angular momentum $J = 15/2$. At lower temperatures the description needs to include the influence of the crystal field. This leads to a splitting of the degenerate (16-fold) Er^{3+} ground state into a series of multiplets, the lowest in energy being a Γ_7-Kramers doublet. The zero field energy splitting between the Kramers-doublet and the in energy next higher Γ_8 quartet was found to lie between $\Delta E = 11\,\mathrm{K} \times k_{\mathrm{B}}$ and $\Delta E = 19\,\mathrm{K} \times k_{\mathrm{B}}$ [Wil69, Sjö75, Dav73, Hah92], here k_{B} is the Boltzmann constant. Consequently, at temperatures well below 1 K and for small magnetic fields the magnetic behavior can be described by treating it as a two level system with an effective spin of $\widetilde{S} = 1/2$ and an isotropic Landé factor of $\widetilde{g} = 6.8$ [Tao71].

The knowledge of the magnetization and the heat capacity of the sensor material, which are both dominated by the erbium ions, form the basis of understanding and optimizing metallic magnetic calorimeters. Since the working temperatures of MMCs is below 100 mK the magnetic moments only occupy states of the Γ_7-Kramers doublet. In order to make predictions on the magnetization and the heat capacity of the material both the magnetic dipole-dipole interaction as well as the indirect RKKY[1] exchange coupling between the magnetic moments need to be included as discussed in [Fle05].

In figure 2.2 an exemplary comparison between the calculated and the measured temperature dependencies of the magnetization and the heat capacity for a $\mathrm{Au{:}Er}_{315\,\mathrm{ppm}}$ thin film are shown for several magnetic fields, respectively. At this point these data serve as a proof that the thermodynamic properties of the sensor material Au:Er can be calculated with confidence and can therefore be considered as well understood.

The time constant for the energy transfer between erbium ions and conduction electrons in gold is known from the temperature dependence of the width of the electron-spin resonance line [vS81]. Lifetime broadening of the erbium resonance is

[1] Initialism for Rudermann Kittel Kasuya Yosida

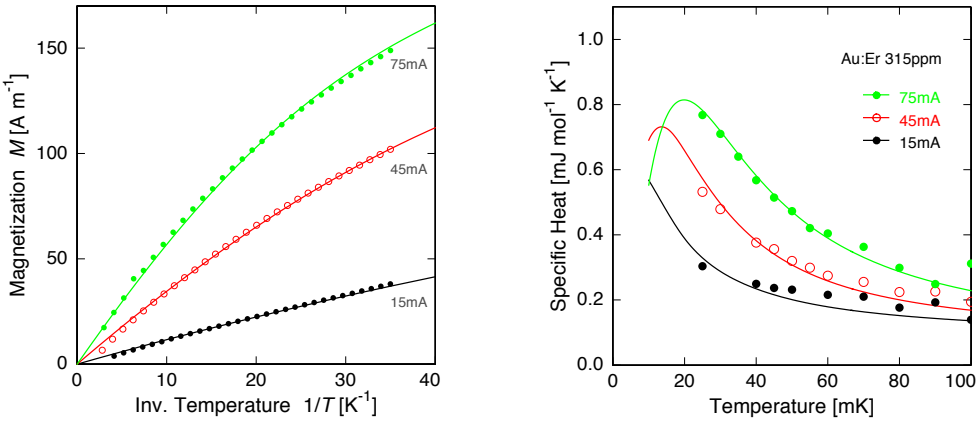

Figure 2.2 **Left:** Magnetization of a Au:Er film with a concentration of 315 ppm erbium as a function of inverse temperature at various applied magnetic fields. **Right:** Specific heat for the same Au:Er sample. For both plots the solid lines represent results of the numerical calculations whereas the symbols represent measured data.

observed even below $T = 1\,\mathrm{K}$ [Sjö75]. From these data the energy relaxation time τ_K between the erbium ions and the conduction electrons obeys the Korringa relation $\tau_\mathrm{K} = K/T$ where $K = 7 \times 10^{-9}\,\mathrm{Ks}$. Once the energy deposited in an absorber is transferred to the sensor via conduction electrons, the spins will register this energy within less than $\simeq 100\,\mathrm{ns}$ at $T = 50\,\mathrm{mK}$. Given a good thermal coupling of the absorber to the sensor, the response time τ_0 of the calorimeter is determined by the Korringa time and the heat capacities of the spin system C_s and the electronic system C_e

$$\tau_0 = \frac{C_\mathrm{e}}{C_\mathrm{e} + C_\mathrm{s}} \tau_\mathrm{K}. \tag{2.5}$$

2.3 Absorber types

In general, a new design of a high resolution detector starts with the choice of the absorber that suits the properties of the particles to be detected. The main points that need to be considered are the quantum efficiency and the geometrical cross section in order to achieve the required stopping power for the particles to be stopped in the energy range of interest, the specific heat of the used material and the efficiency and speed of the absorber of thermalizing the energy. The first properties set a limit on the atomic numbers Z of the absorber material and its geometrical dimensions.

In general the specific heat c of a material is

$$c(T) = c_\mathrm{ph}(T) + c_\mathrm{e}(T) + c_\mathrm{n}(T) + c_\mathrm{sc}(T) + c_\mathrm{TS}, \tag{2.6}$$

the sum of the specific heats given by the different degrees of freedom in a material. This can for example be a phononic contribution c_{ph}, a contribution by conduction electrons c_{e} or the nuclei c_{n}. In the case a material is superconducting the contribution of the free electrons will be reduced due to the formation of Cooper pairs and the electronic term will be replaced by c_{sc}. In addition, tunneling systems can contribute to the specific heat. Different types of materials have already been used for micro-calorimeters and are briefly introduced in the following.

Insulators and Semiconductors This class of material does not have an electronic contribution to the specific heat. Neglecting the contribution of tunneling systems only the contribution c_{ph} of the lattice is of importance. According to the Debye theory this contribution is parameterized as

$$c(T) = c_{\mathrm{ph}}(T) = \beta T^3 \tag{2.7}$$

and can be very small. However, absorbed particles can create electron-hole pairs, that might have long life times. The thermalization of the energy is therefore affected by statistical and positional variation in the electron-hole pair creation and trapping. This degraded thermalization efficiency has proven to impact the energy resolution. Nevertheless, very good results were achieved using semiconducting absorbers with a very small inter-band gap, e.g. mercury cadmium telluride ($\approx 60\,\mathrm{meV}$). Connected to a silicon thermistor an energy resolution below $\Delta E_{\mathrm{FWHM}} = 4\,\mathrm{eV}$ at an X-ray energy of $5.9\,\mathrm{keV}$ was achieved [Dre10]. This combination was chosen to be deployed in the space based ASTRO-H mission to monitor astronomical X-ray sources [Ast10].

Metals Generally, normal conducting metals have excellent thermalization properties, even at very low temperatures. Incident energy is quickly converted to thermal phonons and electrons. This process usually takes place within much less than a microsecond. As for all materials the stopping power for X-rays depends strongly on the atomic number Z of the material and is very good for high Z materials. In metals the electronic contribution to the heat capacity is dominant at temperatures below 1 K. For this class of absorbers the specific heat is given as the sum of the phononic and the electronic contribution,

$$c(T) = c_{\mathrm{ph}}(T) + c_{\mathrm{e}}(T) = \beta T^3 + \gamma T, \tag{2.8}$$

where γ is the material specific Sommerfeld coefficient and the phononic contribution can usually be neglected at $T < 0.1\,\mathrm{K}$.

For many applications gold is used as absorber material due to the good heat conductance and the high stopping power ($Z = 79$). Metals with smaller

electronic density of states are used to benefit from the reduced heat capacity. Bismuth has been studied extensively as the quality of deposited thin films depends crucially on the fabrication technique and meanwhile returns good results. Currently the highest resolving low temperature calorimeter featured an absorber made of a gold-bismuth bilayer in combination with a TES sensor and showed an energy resolution of 1.8 eV at 5.9 keV X-ray energy [Ban08].

Superconductors In the search for absorber materials with high stopping power and low heat capacity, superconductors are promising candidates. At temperatures close to their critical temperatures T_c the electrons start to form Cooper pairs. The electronic contribution to the specific heat is described by

$$c_\mathrm{sc}(T) = a\gamma T_\mathrm{c} e^{-bT_\mathrm{c}/T}, \tag{2.9}$$

with the dimensionless, material specific parameters a and b. Thus at temperatures well below their transition to the superconducting state ($T \ll T_\mathrm{c}$), the electronic contribution to the specific heat is negligible and only the phononic contribution remains. This fact allows for the use of large volume absorbers without fundamentally compromising the energy resolution.

Besides this attractive aspect, superconductors are not widely used as absorbers since they present a more complicated thermalization of energy that is not fully understood up to now. Different candidates have already been studied covering both type I and type II superconductors [Cos93, Zin06, Per08]. From [Cos93] it was concluded that for superconductors made of pure elements an empirical law can be derived stating that for temperatures $T < 2 \times 10^{-4} \Theta_\mathrm{D}$ not the entire energy released in the absorber is contributing to the detector signal on the observable timescales.

Nevertheless, superconductors have already been used as absorber material of MMCs. Rhenium was used for the measurement of the β-spectrum of ^{187}Re. The choice of superconducting rhenium over other rhenium compounds is motivated by the higher activity per unit of heat capacity that is achievable. In addition to these studies MMCs were used to investigate the thermalization of energy in different superconductors. Aluminum and aluminum manganese were studied in [Wel08, Ran09] and their interesting results will be discussed briefly in chapter 6.1. In particular MMCs with 50 μm thick aluminum absorbers showed fast rise times of $\tau_0 \simeq 0.6\,\mu$s and an energy resolution of $\Delta E_\mathrm{FWHM} < 10$ eV for 6 keV photons. These results further encourage the investigation of superconducting absorbers.

So far, the underlying thermalization behavior of the absorbed energy in a superconductor is not fully understood. On the one hand the application of

superconductor as absorber for low temperature detectors are motivated by the achievable high stopping power per unit of heat capacity. Tin for example was employed successfully for gamma-ray spectroscopy where an energy resolution of $\Delta E_{\mathrm{FWHM}} = 42\,\mathrm{eV}$ at an energy of 103 keV was achieved [Zin06]. On the other hand, the high sensitivity of low temperature detectors allows to investigate the thermalization of energy in superconductors.

Table 2.1 summarizes the properties of absorber materials presently used with microcalorimeters and gives an example for each category discussed before. It shows the values for the pre-factor β of the phononic contribution to the specific heat and the Sommerfeld coefficients γ. It also lists the total thickness d required to achieve 95% quantum efficiency at a photon energy of $E = 5.9\,\mathrm{keV}$, which corresponds to an X-ray line that is accessible calibration purposes and lies in the energy range of interest for many detector applications. This and the specific heat for such absorbers at a typical operating temperature of $T = 30\,\mathrm{mK}$ are the most interesting quantities for designing a new high-resolution detector. For the detection of soft X-rays the detector is often assumed to have an absorber heat capacity corresponding to absorber dimensions of $250 \times 250 \times d\,\mu\mathrm{m}^3$. Evidently absorber types, for which the electronic contribution to the heat capacity is not present as in semiconductors or strongly suppressed due to pairing as in superconductors, the specific heat is very small.

Table 2.1 Properties of different absorber materials [Win07, Hen93, Kit06].

Property	**Units**	**HgCdTe**	**Si**	**Au**	**Bi**	**Re**
Type		semiconductor		metal		superconductor
Atomic number, Z	-		14	79	83	75
Molar mass, M_{mol}	g/mol					
Density, ρ	$\mathrm{kg/m^3}$	1355	2330	19300	9780	21020
β	$\mathrm{J\,K^{-4}/m^3}$		0.6	42.5	54.1	3.0
Sommerfeld coefficient, γ	$\mathrm{J/K^2/m^3}$			65.7	3.9	265.2
Atten. length λ (5.9 keV)	μm	1.4	28.9	1.1	2.0	1.3
d for 95% Q.E. @ 5.9 keV	μm	4.2	86.5	3.4	6.0	3.9
$C(30\,\mathrm{mK})_{(250\times250\,\mu\mathrm{m}^2)\times d}$	pJ/K		4×10^{-6}	0.42	0.04	2×10^{-5}

2.3.1 Down-conversion of energy in a superconductor

In a detector for neutrino mass measurements discussed here superconducting rhenium is used as absorber material. This section gives a short introduction to what is known on the energy thermalization in superconductors and points out the possible experimental challenges connected with it. It also underlines the fact that it involves many facets of fascinating condensed matter physics that can be explored,

as so far no microscopic theory exists that can explain all observed effects. In this section a short discussion of the possible mechanisms of the energy thermalization process in a superconducting absorber is given. According to literature the energy downconversion in a superconductor following the absorption of a photon occurs in three distinct stages [Koz00]:

1. The absorption of an X-ray will ionize an atom and produce a primary photo electron. Shortly after this, the deposited energy will be carried by a small number of energetic electrons. These electrons will lower their average energy through direct electron-electron interactions thereby breaking Cooper pairs and producing quasiparticles until an average energy W_0 is reached. These processes usually take place within picoseconds.

2. At this point, quasiparticles start emitting many Debye-phonons in a very fast cascade. This phase ends when the strongly non-equilibrium quasiparticles have relaxed to energies around the Debye energy W_D.

3. In a third stage, the excited quasiparticles relax down to states close to the gap edge Δ of the superconductor through coupled mechanisms of energy exchange between quasiparticles and phonons.

Generally, the density of excess quasiparticles produced by a single event is quite low. For soft X-rays or β-particles of a few keV energy approximately 10^6 quasiparticles are generated. For typical absorber volumes this corresponds to a few quasiparticles per $\mu\mathrm{m}^3$ resulting in a low recombination rate. Moreover, a bottleneck is caused by the competition between the pair-breaking rate and the escape rate of 2Δ phonons emitted in the recombination process. Long recombination times and the phonon bottleneck contribute to delay the transfer of the energy trapped in the quasiparticle system on time scales much longer than the characteristic ones of thermal detectors. Thus, this amount of "undetected" energy could degrade the energy resolution of the detector as the signal to noise ratio will be compromised. These effects were studied for tin and tantalum absorbers in [Per04, Per08].

A poor thermal conductance of large volume superconducting absorbers can lead to pulse shape variations depending on the position of energy absorption. Also the creation of high energetic phonons that can travel long distances within superconducting crystals can lead to extra energy losses to the substrate. Such energy losses can cause a deformation of the energy spectrum. As energy is lost for some events, these can cause tails on the low energy side of discrete lines in the X-ray energy spectra.

2.3.2 Rhenium as absorber material

For neutrino mass measurements with low temperature calorimeters, ^{187}Re is a promising isotope to be studied as a β-source. Due to the low endpoint energy, the only way to precisely measure the electron energy spectrum is to implement the source directly into the absorber and perform a calorimetric measurement. As already discussed, our approach is to use natural rhenium as absorber material. In this section general properties of rhenium are discussed in more detail, some of which are summarized in Table 2.3.2.

Table 2.2 Some physical properties of rhenium [Win07, Kit06, Sis04, Tul80].

Natural abundance	^{185}Re (37.4%), ^{187}Re (62.6%)
Half life of ^{187}Re	43.2 Gy
Density	21.02 g/cm^3
Electronic configuration	$[Xe]4f^{14}5d^{5}6s^{2}$
Crystal structure	hcp
Lattice constants a/c	2.76 Å/4.45 Å
Debye temperature Θ_{D}	417 K
Transition temperature T_{c}	1.69 K
Gap energy Δ	0.39 meV
Melting point	3459 K
Coherence length ξ_0	$110 - 150$ nm
London penetration depth λ	$56 - 68$ nm
Critical field B_{C} at $T = 0$ K	20.0 mT
El. resistivity (300 K)	18 $\mu\Omega$cm
Sound velocities $v_{\mathrm{t}}/v_{\mathrm{l}}$	2930/5360 m/s

The rare transition-metal rhenium naturally occurs as a mix of the isotope ^{185}Re (37 %), which is stable, and the isotope ^{187}Re (63 %), which is unstable with a very long half life $\tau_{1/2} = 43.2$Gy [Sis04]. Rhenium crystals have a hexagonal close-packed structure and are type I superconductors with a critical temperature of $T_{\mathrm{c}} = 1.7$ K. The ratio of the critical temperature to the Debye temperature is very small $T_{\mathrm{c}}/\Theta_{\mathrm{D}} = 1.7\,\mathrm{K}/417\,\mathrm{K} = 0.004$ and thus rhenium is accounted to the weakly coupled superconductors. The high melting point of more than 3400 K and the high density of 21.02 g cm^{-3} are only exceeded by a few elements.

β-decay of ^{187}Re

The isotope ^{187}Re is unstable with a comparably long lifetime and decays by a single unique, first forbidden transition to the ^{187}Os ground state according to

$$^{187}\mathrm{Re} \rightarrow {}^{187}\mathrm{Os} + \mathrm{e}^{-} + \overline{\nu_{\mathrm{e}}}. \tag{2.10}$$

Considering the long half life of ^{187}Re, the natural isotope abundance x_{187} and the molar mass M_{Re} the activity A is given by

$$A = x_{187} \frac{m_{\mathrm{Re}} N_A}{M_{\mathrm{Re}}} \frac{\ln 2}{\tau_{1/2}}. \tag{2.11}$$

For 1 mg of rhenium this gives an activity of approximately 1.0 Bq. As discussed in section 1.4.3 in respect to pileup events the total activity is a crucial parameter for calorimetric measurements of the neutrino mass. The given activity of a detector with bulk rhenium of that weight does indeed suit the needs for those experiments. A rhenium absorber of 1 mg would for example be a cuboid with side lengths $250 \times 250 \times 750\,\mu\mathrm{m}^3$.

Heat capacity

As discussed before, the heat capacity of the absorber is of utmost importance for a low temperature calorimeter. In equation (2.6) the specific heat was described as a sum of contributions given by the different degrees of freedom. The specific heat of rhenium has been studied by various groups [Sha67, GH71].

Compared to other metals rhenium metal in the normal conducting state has a large Sommerfeld coefficient. Normalized to volume this is approximately a factor of four larger than the one for gold. Therefore using normalconducting rhenium as absorber material would not be the first choice.

In fact, the operating temperatures of low temperature detectors are well below the transition temperature of rhenium, thus the contribution of the electronic system to the specific heat is strongly reduced. The properties of superconducting rhenium are in agreement with the properties of a weak-coupling superconductor that is calculated on the basis of the BCS theory of superconductivity. The electronic contribution to the specific heat in the superconducting state can thus be expressed as

$$c_{\mathrm{sc}} = a\gamma T_C e^{(-bT_C/T)} \tag{2.12}$$

with $a = 8.14$, $b = 1.413$ and $\gamma = 2290\,\mu\mathrm{Jmol}^{-1}\mathrm{K}^{-2}$ [Smi70]. At 50 mK, the electronic system of 1 mg superconducting rhenium will only have a heat capacity of $C_{\mathrm{sc}} = 2.6 \times 10^{-16}\,\mathrm{pJ/K}$ – a value approximately sixteen orders of magnitude below that of the normal conducting state. These considerations emphasize the importance of rhenium being superconducting at the detector's working temperatures.

The dominating specific heat should thus be given by the lattice contribution

$$c_{\mathrm{ph}} = \beta T^3. \tag{2.13}$$

With $\beta = 27\,\mu\mathrm{Jmol^{-1}K^{-4}}$ [GH71] and $m = 1\,\mathrm{mg}$, the heat capacity at $T = 50\,\mathrm{mK}$ would be as small as $C_{\mathrm{ph}} = 0.02\,\mathrm{pJ/K}$. For completeness it should be mentioned, that rhenium shows a very large specific heat attributed to the nuclear moments

$$c_{\mathrm{N}} = AT^{-2} + BT^{-3}, \tag{2.14}$$

using $A = 40.6\,\mu\mathrm{Jmol^{-1}K}$, $B = 0.0034\,\mu\mathrm{Jmol^{-1}K^2}$, [GH71].

At a temperature of 50 mK the nuclear heat capacity of 1 mg adds up to a large value of $C_{\mathrm{N}} = 17486\,\mathrm{pJK^{-1}} + 615\,\mathrm{pJK^{-1}}$. In fact this very large heat capacity will not effect the detector response after the absorption of a particle as the nuclear spin system is strongly decoupled from the electronic system. The nuclear-spin lattice relaxation times become very long (presumably of the order of tens of seconds like in other superconductors [Phi64]), thermally isolating the nuclear spin system.

2.4 Detector readout

The magnetic nature of the detector signal requires a precise measurement of magnetic flux changes in the vicinity of the spins. Technically, sensitive and low noise magnetometers are a prerequisite for high resolving MMCs. In this section magnetometers based on **S**uperconducting **Q**uantum **I**nterference **D**evices (SQUIDs) are introduced and their noise performance as well as other experimental details are discussed.

Many of the early MMC devices were based on available gradiometric dc-SQUIDs, which were equipped with one or two cylindrical sensors and exposed to an external magnetic field. The external field was for example generated by a hand wound coil of superconducting wire [Fle03]. The development of thin film techniques opened a new field of possible geometries and readout schemes. The signal coupling from the spins of the sensor material to the magnetometer is addressed in the last part of this section.

2.4.1 Magnetometer

In MMCs, small changes of the magnetic flux represent the temperature rise upon the absorption of a particle and thus the energy deposited by it. To measure this flux change SQUIDs are used. Usual signal amplitudes are of the order of a magnetic flux quantum $\Phi_0 = h/2e = 2.07 \times 10^{-15}\,\mathrm{Vs}$, to put this into perspective the magnetic earth field penetrating an area of $200\,\mu\mathrm{m} \times 200\,\mu\mathrm{m}$ – which would be the area of a typical sensor – corresponds to approximately $1000\,\Phi_0$ and is more than three orders of magnitude larger than the signals detected by a SQUID in an MMC. Thus for high resolution measurements, the amplitude of time-dependent magnetic stray fields at the detector needs to be reduced significantly by proper shielding.

A SQUID, together with a suitable readout electronics, combine low intrinsic noise with a large usable bandwidth and comparably low power dissipation. A detailed description of SQUIDs can be found in the literature [Cla04]. Here only a brief summary is given.

DC-SQUIDs

A dc-SQUID is a superconducting device for converting magnetic flux, electrical current or any other physical quantity that can be converted into magnetic flux, into a voltage. A schematic of a SQUID is shown in figure 2.3a). It consists of a superconducting loop with two regions of weak superconductivity – the Josephson junctions. In parallel to each junction a shunt resistor avoids hysteretic behavior of the device.

The weak links are small enough for Cooper pairs to tunnel through the insulating barrier maintaining their phase coherence. A representative current voltage-characteristic is shown in 2.3b). When the bias current I_b is lower than a critical current I_c driven through the device, the current is carried by tunneling Cooper pairs and no voltage drop across the junctions is observed. For bias currents slightly larger than I_c, the device jumps to a resistive branch and a voltage drop across the junctions occurs. This regime can be described with a dynamic resistance $R_{dyn} = \partial U / \partial I_b$. For larger bias currents the voltage drop asymptotically approaches an ohmic behavior with a slope dominated by the shunt resistors. The absolute value of the critical current depends on the superconducting material, operation temperature, the geometry of the tunneling barriers and, for our purposes most important, periodically on the magnetic flux inside the SQUID loop.

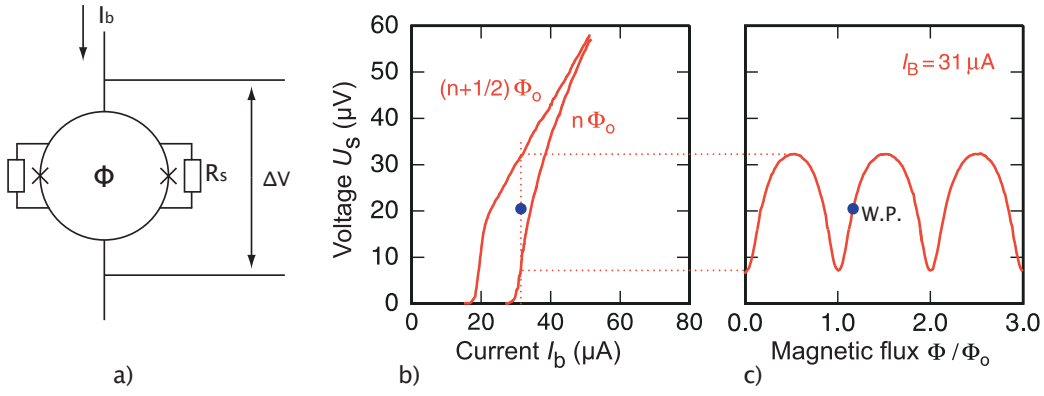

Figure 2.3 **a:** Schematic of a SQUID. **b:** $I - V$ characteristic of a SQUID. **c:** $V - \Phi$ characteristic of a SQUID [Wei96].

For a magnetic flux of $\Phi = n\Phi_0$ and $\Phi = (n+1/2)\Phi_0$, the two extremal branches of the voltage-current characteristic are observed as depicted in figure 2.3b). Thus, for a constant bias current I_b the voltage signal changes periodically with continuously increasing flux Φ as depicted in figure 2.3c). The period of this oscillation is given by the magnetic flux quantum Φ_0.

In response to a small input flux $\delta\Phi \ll \Phi_0$ the voltage drop across the SQUID can be considered linear and effectively is a flux-to-voltage converter. In order to achieve a large voltage drop for small flux changes in the SQUID loop, a SQUID is operated at the steepest point of the voltage-flux characteristic, where the absolute value of the transfer coefficient $V_\Phi = (\partial V/\partial\Phi)_I$ is maximal.

Second SQUID stage

The main problem concerning the direct readout of a SQUID is that the voltage noise of even the best room temperature amplifier is significantly higher than the noise of a bare SQUID, which is typically in the order of $S_U = 100\,\mathrm{pV}/\sqrt{\mathrm{Hz}}$ for a device operated at liquid helium temperature. For low noise, high bandwidth applications a second SQUID stage can be introduced between the first-stage SQUID and the room temperature readout electronics. A two-stage readout setup is an efficient way to increase the transfer coefficient and thus reduce the noise contribution of the room temperature electronics.

In a two stage readout configuration as depicted in figure 2.4 both SQUID stages are individually biased with the bias currents I_b1 and I_b2, respectively. A change in flux in the first stage (e.g. induced by a current in the input coil L_i1) causes a change of voltage across the first stage SQUID which in turn results in a current δI_1 flowing through the input coil L_i2 of the secondary SQUID. This changes the magnetic flux in the amplifier SQUID by

$$\delta\Phi_2 = M_\mathrm{is2}\delta I_1 \tag{2.15}$$

where M_is2 is the mutual inductance of input coil and secondary SQUID. Together with the used gain resistance R_g this leads to a small-signal flux-to-flux amplification of

$$G_\Phi = \frac{\partial\Phi_2}{\partial\Phi_1} = M_i\left(\frac{\partial I_1}{\partial\Phi_1}\right)_{R_\mathrm{g},I_\mathrm{b}} \tag{2.16}$$

at the working point. For convenience this flux gain is tuned to lie between $G_\Phi = 1$ and $G_\Phi = 2$ in order to guarantee a steep slope of the two-stage $V-\Phi$ characteristic that features unique working points.

Due to the flux gain G_Φ and the transfer coefficient V_Φ of the second stage SQUID, the input noise contribution of the room-temperature electronics to the apparent flux

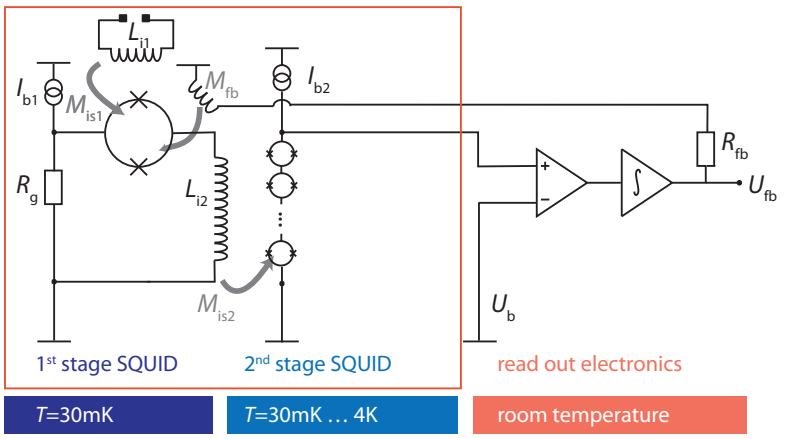

Figure 2.4 Schematic of a two stage SQUID magnetometer including a flux-locked loop circuit.

noise in the detector can be greatly reduced. In the framework of this thesis a series-SQUID array is used as a second stage SQUID. It consists of $14 - 25$ SQUIDs in series. The voltages drops across these SQUIDs add coherently, which leads to a steep slope at the working point of approximately $1 - 2\,\mathrm{mV}/\Phi_0$.

FLL mode

The linear regime of the SQUID as a flux-to-voltage converter is usually limited to a few percent of a flux quantum. In order to linearize the response in a larger flux range a SQUID is typically operated in a so called flux-locked loop (FLL) mode. The main components of the FLL circuitry are also included in figure 2.4.

In the FLL mode any variation of the voltage across the SQUID at the chosen working point is amplified, integrated and fed back into the SQUID loop via a feedback resistor R_{fb} and a feedback coil that is inductively coupled to the SQUID. The strength of this coupling is given by the mutual inductance M_{fb}. Choosing a negative feedback, the flux in the SQUID is kept constant and the output signal of the FLL-electronics is the voltage U_{fb} across the feedback resistor:

$$U_{\mathrm{fb}} = \frac{R_{\mathrm{fb}}}{M_{\mathrm{fb}}} \Delta\Phi_{\mathrm{fb}}, \tag{2.17}$$

which depends linearly on the compensating flux $\Delta\Phi_{\mathrm{fb}}$ and therefore is also linear in the detected flux change.

FLL dynamics

The dynamic performance of a SQUID system is mainly characterized by two parameters: the FLL bandwidth $f_{3\mathrm{dB}}$ and the slew rate $\dot{\Phi}_{\mathrm{max}}$. The FLL bandwidth defines the maximum signal frequency while the slew rate describes the maximum rate at which the electronics can change the flux in the SQUID.

The slew rate of the SQUID system described before is derived in [Cla04] and it is given by

$$\dot{\Phi}_{\max} = \pi \Delta\Phi_{\mathrm{lin}} \left.\frac{\partial U}{\partial \Phi}\right|_{\Phi_A} \frac{M_{\mathrm{fb}}}{U_{\mathrm{fb}}} f_{\mathrm{GBP}}. \tag{2.18}$$

The slew rate is proportional to the quasi-linear regime $\Delta\Phi_{\mathrm{lin}}$ of the $V - \Phi$ characteristic, as well as to the unity-gain bandwidth f_{GBP} of the amplifier and integrator.

For typical values of the SQUID systems used within this work, slew rates of up to $10\,\mathrm{M}\Phi_0/\mathrm{s}$ were achieved. Assuming the rise time to be limited to $\tau_0 \simeq 0.1\,\mu\mathrm{s}$ by the spin-electron coupling in the sensor material, detector signals of up to one flux quantum in amplitude can be resolved by the SQUID readout.

2.4.2 Readout geometries

As we discussed before, the magnetization change of the paramagnetic sensor is inductively read out by a pick-up coil in a close vicinity of the sensor.

Several possible planar readout geometries are depicted in figure 2.5. Most of the MMCs developed and discussed in this work are based on the geometry shown in figure 2.5a). It consists of two meander-shaped pick-up coils of inductance L_{m} that are connected in parallel and form a first order gradiometer. The input coil of a SQUID L_{i}[2] is connected in parallel to the two meanders.

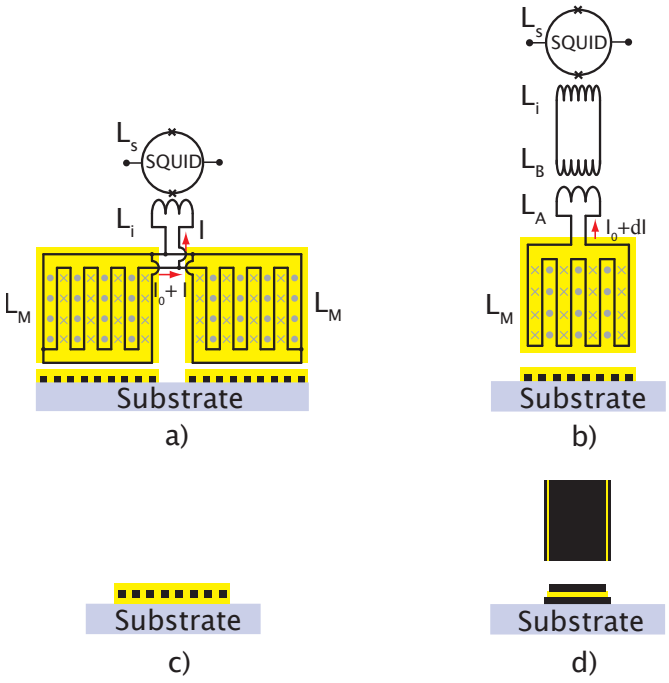

Figure 2.5 Different coupling schemes of micro-fabricated MMCs.

[2] L_{i} refers to the input coil inductance L_{i_1} of the first stage SQUID, for the sake of simplicity the index will be omitted from now on.

In the MMCs discussed in this work the superconducting pick-up coil serves two purposes: it generates the necessary magnetic field by a persistent current of several milliampere and it detects the flux changes within the pick-up coil that occur upon the absorption of a particle.

The magnetic field induced by the persistent current is a inhomogenous multipole field of high order. The meander-shaped geometry reduces the magnetic cross talk of neighboring pixels but also makes a precise calculation of the field distribution necessary to predict detector performance and to optimize devices.

A readout geometry as sketched in figure 2.5b) can further reduce the degrading effect of stray inductances. Here an additional flux transformer is included in the design.

In the geometries described so far the paramagnetic sensor is only placed on top of the pick-up coil and thus not more than one half of the field energy generated by the current in the meander will be distributed within the volume of the sensor. For further reference the filling factor F will be defined as the fraction of the field energy located within the sensor volume.

Obviously, a higher filling factor will potentially allow for larger signals and thus further development towards a sandwich type design is promising. In a sandwich type design the sensor can either be placed on both sides of the planar meander-shaped coil or the sensor can be placed in between two field generating planar structures. Both possible schemes are sketched in figure 2.5c) and 2.5d), respectively.

Placing the sensor on both sides of the pick-up coil will not change the general considerations of the coil shape. In the case a very thin sensor is sandwiched in between two coils the magnetic field distribution in the sensor will be almost homogenous and hence the actual geometry of the trilayer will not be much constrained.

2.4.3 Coupling

For all geometries and magnetic coupling schemes discussed in the previous section the flux coupling from the pick-up coil to the SQUID loop is important in order to predict signal sizes and noise contributions. The flux coupling depends on all involved inductances, namely the inductance L_m of the pick-up coil, the input coil inductance L_i of the SQUID and all involved stray inductances L_str given for example by bonding wires and on-chip wiring. Additionally, the mutual inductance M_is of the SQUID's input coil to the SQUID loop itself and the inductances of an additional flux transformer, if present, are important.

A good estimate for the coupling can be found in the following way: by applying Kirchhoff's rules to the circuits shown in figure 2.5a), the flux coupling can be parameterized by the introduced inductances. For the scheme of two meanders

connected in parallel the fraction of flux coupled to the SQUID loop is given by:

$$\frac{\partial \Phi_{\mathrm{S}}}{\partial \Phi} = \frac{M_{\mathrm{is}}}{L_{\mathrm{m}} + 2(L_{\mathrm{i}} + L_{\mathrm{str}})}. \tag{2.19}$$

Using typical numbers for inductances of meanders and input coil used within this work, one can calculate the fraction of magnetic flux coupled from the meander to the SQUID loop.

For a SQUID with a mutual inductance $M_{\mathrm{is}} = 0.38\,\mathrm{nH}$ and an input inductance of $L_{\mathrm{i}} = 1.8\,\mathrm{nH}$, a meander with inductance $L_{\mathrm{m}} = 1.8\,\mathrm{nH}$ and a stray inductance of the leads of $L_{\mathrm{str}} = 0.5\,\mathrm{nH}$ the fraction of flux coupled from the meander to the SQUID is approximately 6 %.

2.5 Signal, noise and numerical optimizations

Up to now several aspects of magnetic calorimeters were treated. This section focuses on the detector theory of metallic magnetic calorimeters. The generation of the signal and some unavoidable noise sources are discussed as well as their impact on the energy resolution. In conclusion the optimization of a magnetic calorimeter for a certain application is discussed.

The thermodynamical properties of the sensor and the absorber material are the cradle of all thermal detectors. The properties of the bulk Au:Er are well understood and are accessible by numerical calculations as described in section 2.2. Also thin film techniques reproduce the values of bulk erbium gold alloys. Combining this fact with the knowledge of the field distribution generated by the pick-up coil in the sensor volume, the flux change $\delta\Phi$ in a given pick-up coil upon the deposition of energy δE can be calculated with confidence. This can be applied for a wide variety and range of operational parameters like temperature T, field generating current I, absorber heat capacity C_{a} or erbium concentration x.

We will see that the fundamental limit to the energy resolution of a calorimetric detector depends on the thermodynamic fluctuations of energy between the absorber heat capacity C_{a}, the sensor heat capacity C_{s} and the thermal bath. Other dominant noise sources come from the readout chain and the sensor material. All of the named noise contributions can be calculated from the detector parameters or can at least be empirically parameterized. Combining their spectral power densities with the one of the expected signal allows to calculate the noise equivalent power NEP and with that the energy resolution ΔE_{FWHM} of the detectors.

In the following paragraphs an analytical approach to describe the expected signal size is made. It is followed by a parameterization of the noise. The combination of both components give a measure to optimize for the best possible energy resolution.

2.5.1 Signal

Even if most MMCs developed within this work are based on transformer-coupled meanders depicted in figure 2.5a) and b) we want to start the calculation of the signal size by considering the sandwich geometry depicted in figure 2.5d). In this geometry the magnetic field in the sensor is nearly homogenous and easier for analytical treatment. At a later point we will get back to the meander based geometries. Figure 2.6 shows a sketch of the sandwich type geometry.

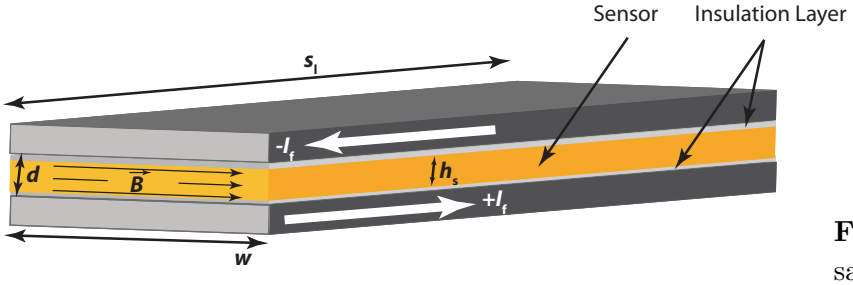

Figure 2.6 Sketch of a sandwich type geometry.

Here, the paramagnetic sensor is sandwiched by two insulated superconducting planar leads of width w and length s_l. The vertical distance between the two leads is d and the sensor height is h_s. The field generating current I_f is injected in opposite directions below and above the sensor. For $d \ll w$ the current generates a nearly homogenous magnetic field

$$B = \mu_0 \frac{I_\mathrm{f}}{w} \tag{2.20}$$

in the plane of the sensor, where $\mu_0 = 4\pi \times 10^{-7}\,\mathrm{Vs/A/m}$ is the permeability of free space. The inductance of the structure can be written as

$$L_\mathrm{m} = \mu_0 \frac{s_\mathrm{l} d}{w}. \tag{2.21}$$

The homogenous magnetic field B leads to a potentially higher energy resolution, since for a homogenous temperature distribution all spins give the same and therefore optimal signal response. Beneficial is also the intrinsically small coil inductance per sensor square.

The signal is given by the flux detected in the SQUID per deposited energy $\delta\Phi_\mathrm{S}/\delta E$ and one important contribution to the noise, the intrinsic flux noise of the SQUID S_Φ. Assuming that the used SQUID has a fixed coupled energy sensitivity ϵ, the flux noise can be expressed as $S_\Phi = 2L_\mathrm{S}\epsilon$, where L_S is the inductance of the SQUID loop. The signal-to-noise ratio is the quantity that needs to be optimized.

$$\frac{\delta\Phi_\mathrm{S}/\delta E}{\sqrt{S_\Phi}} \propto \frac{\delta\Phi/\delta E}{\sqrt{L_\mathrm{m}}}. \tag{2.22}$$

Using (2.4) and (2.21) one finds the following quantity to be optimized

$$\frac{\delta\Phi/\delta E}{\sqrt{L_\mathrm{m}}} = \sqrt{\mu_0}\sqrt{F}\frac{\sqrt{swh}}{c_\mathrm{s}swh + C_\mathrm{a}}\frac{\partial M}{\partial T}, \tag{2.23}$$

where c_s and M denote the specific heat per unit volume and the magnetization of the sensor material, respectively. Furthermore, it is assumed that the sensor material only fills the fraction $F \simeq h/d$ of the gap between the coplanar sandwich structures. The third factor in (2.23) is maximized once the heat capacity of the sensor equals the absorber heat capacity $c_\mathrm{s}swh = C_\mathrm{a}$, using this criterium leads to the expression

$$\frac{\delta\Phi/\delta E}{\sqrt{L_\mathrm{m}}} = \sqrt{F}\frac{1}{2\sqrt{C_\mathrm{a}}}\left[\sqrt{\frac{\mu_0}{c_\mathrm{s}}}\frac{\partial M}{\partial T}\right]. \tag{2.24}$$

The condition $c_\mathrm{s}swh = C_\mathrm{a}$ can be used to calculate the sensor volume, when the corresponding specific heat is known. This also means that two of the three dimensions of the sensor can be chosen freely, which in turn opens a wide range of inductances for the pick-up coil. The last factor of (2.24) only depends on the magnetic field strength and on the properties of the sensor material, namely the concentration of magnetic erbium ions, their g-factor and the RKKY interaction strength α and needs to be optimized. Assuming $g = 6.8$ and $\alpha = 5$ for Au:Er [Fle05] this factor can be optimized numerically and becomes

$$\left[\sqrt{\frac{\mu_0}{c_\mathrm{s}}}\frac{\partial M}{\partial T}\right]_{x_\mathrm{opt},B_\mathrm{opt}} = 0.23\frac{1}{\sqrt{T}}. \tag{2.25}$$

At a temperature of $T = 50\,\mathrm{mK}$ the maximum of this factor is reached for a magnetic field of $B_\mathrm{opt} = 15\,\mathrm{mT}$ and a rather large concentration of $x_\mathrm{opt} = 2200\,\mathrm{ppm}$. For these parameters the specific heat of the Au:Er sensor is $c_\mathrm{s,opt} = 500\,\mathrm{J/m^3/K}$. The values of B_opt, x_opt and $c_\mathrm{s,opt}$ vary proportional to T. It is worth mentioning that this maximum is rather flat. Even choosing a concentration or a magnetic field that is smaller by a factor of two reduces the signal to SQUID flux noise ratio only by approximately 10%.

To give a first impression for the quantities involved, an MMC operated at $T = 50\,\mathrm{mK}$ with an absorber heat capacity of $1\,\mathrm{pJ/K}$ is assumed to absorb a $5.9\,\mathrm{keV}$ photon. For a pick-up coil with inductance $L_\mathrm{m} = 100\,\mathrm{pH}$ this can at most produce a flux change of $2.3\,\Phi_0$. Assuming a sensor with a height of $h_\mathrm{s} = 0.3\,\mu\mathrm{m}$ that is operated in the optimal field would yield a sensor area of $A_\mathrm{s} \simeq (81\,\mu\mathrm{m})^2$. A sandwich structure with a width of $w = 5\,\mu\mathrm{m}$ would have a length of $s_\mathrm{l} \simeq 1300\,\mu\mathrm{m}$ and according to (2.21) an inductance of approximately $L_\mathrm{s} \simeq 100\,\mathrm{pH}$. In case of transformer-coupling to a 100 pH SQUID, the flux would be reduced by approximately a factor of two. Using a detector not featuring the sandwich structure, the filling factor F would be in the order of 0.4, leading to a reduction of the signal by a factor of $\sqrt{F} = 0.625$.

A reduction in signal size by a factor of $1/\sqrt{2}$ would be the result of using a setup where two detection loops are gradiometrically wound and connected in parallel.

The setup that is depicted in figure 2.5a) allows to readout two pixels with only one readout channel. Here, the coupling of the signal is reduced by a factor of $(2\sqrt{2F}) \simeq 1.8$ compared to the ideal scenario of the sandwich geometry discussed before.

2.5.2 Noise contributions and noise equivalent power

For the further discussion a common figure of merit, the noise equivalent power or NEP is introduced. It is defined by the root mean square (rms) power required at the input at a given frequency to produce an output voltage equal to the rms noise voltage in a unit bandwidth at that frequency and is the inverse of the signal to noise ratio. The NEP of the detector can be expressed as the incoherent sum of the individual noise sources:

$$\mathrm{NEP}^2(f) = \mathrm{NEP}^2_{\mathrm{TD}}(f) + \mathrm{NEP}^2_{\mathrm{SQ}}(f) + \mathrm{NEP}^2_{\mathrm{ER}}(f). \tag{2.26}$$

The energy resolution of thermal detectors with frequency dependent NEPs are discussed in detail in [McC05]. Within the framework of optimal filtering of the detector signal it was shown that the energy resolution can be calculated from the integrated noise equivalent power by

$$\Delta E_{\mathrm{FWHM}} = 2.35 \Delta E_{\mathrm{rms}} = 2.35 \left(\int_0^\infty \frac{4}{\mathrm{NEP}^2(f)} \, \mathrm{d}f \right)^{-1/2}. \tag{2.27}$$

From this equation it is obvious that the lower the NEP, the better the energy resolution. Since the integral is evaluated over all frequencies, also the frequency dependence of the NEP is important. In general, the energy resolution will become better, the larger the frequency range with small NEP. This expression can be solved analytically or numerically for any number of noise sources that can be parametrized and need to be included into the model.

The signal in the frequency domain is given by

$$\tilde{p}(f) \frac{\partial \Phi}{\partial E} \Delta E, \tag{2.28}$$

where

$$\tilde{p}(f) \simeq \frac{\tau_1}{\sqrt{1 + (2\pi f \tau_0)^2} \sqrt{1 + (2\pi f \tau_1)^2}} \tag{2.29}$$

is a normalized responsivity of a detector. Here τ_0 is the time constant of an assumed exponential rise of the signal and τ_1 the time constant of the signal decay, respectively.

The most fundamental contributions to the noise in a calorimetric detector are the energy fluctuations between the subsystems of the calorimeter and the fluctuations between the calorimeter and the thermal bath. Figure 2.7 illustrates the scenario as a canonical ensemble with two subsystems.

The conduction electrons of the sensor and the absorber are combined to a heat capacity C_e on the top left. They are thermally linked by the conductance g_ze to the subsystem of the magnetic moments with a heat capacity C_s (top right). Furthermore, the electronic system is connected to the thermal bath with temperature T_0 via a thermal link g_b.

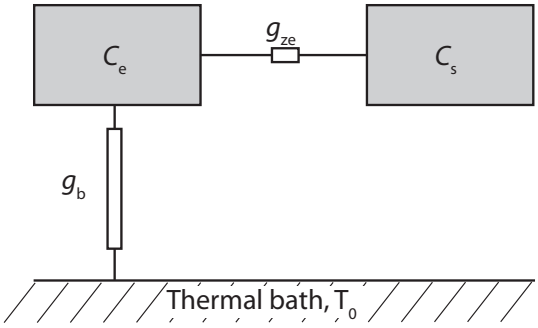

Figure 2.7 A simplified model of a magnetic calorimeter with two subsystems.

The energy content and its evolution in time can be described by two differential equations (for details see [Fle05]). At a fixed temperature the energy content in the spin system varies with a standard deviation of

$$\sigma(E_\mathrm{s}) = \sqrt{k_\mathrm{B} C_\mathrm{s} T^2}. \tag{2.30}$$

The spin system is connected to the electronic system and the thermal bath by two different thermal links giving rise to fast and slow fluctuation of energy to the respective system.

The corresponding contribution to the NEP is

$$\mathrm{NEP}_\mathrm{TD} = \tilde{p}^{-1} \sqrt{2 C_\mathrm{a} k_\mathrm{B} T^2} \left[\frac{4\tau_1}{1 + (2\pi f \tau_1)^2} + \frac{4\tau_0}{1 + (2\pi f \tau_0)^2} \right]^{1/2}. \tag{2.31}$$

Here the first term of the sum is caused by the fluctuations of energy between the system of magnetic moments and the thermal bath, whereas the second term is caused by the fluctuations of energy between the system of the magnetic moments and the conduction electrons. The second term limits the useful bandwidth as well as it sets a limit to the achievable energy resolution.

For a high resolution X-ray detector typical values are a rise time of $\tau_0 = 1\,\mu\mathrm{s}$, a decay time of $\tau_1 = 1\,\mathrm{ms}$ and an absorber heat capacity of $C_\mathrm{a} = 1\,\mathrm{pJ/K}$ at a temperature of $T = 50\,\mathrm{mK}$ leading to a frequency dependent NEP with two plateaus that

represent the low frequency term and the high frequency term of (2.31), respectively. The plateau values are given by 1.6×10^{-20} W for the first term and by 5.2×10^{-22} W for the second term. The NEP is plotted as a function of frequency in figure 2.8 together with the other contributions to the total NEP, which will be described in the following.

The noise of the SQUID readout can be in the same order of magnitude as the fundamental thermodynamic fluctuations of energy if the coupling between magnetic moments and the SQUID is not carefully optimized. The SQUID noise can thus be a potentially limiting factor to the energy resolution of MMCs. Typically, a SQUID adds two noise contributions, one being white in frequency and another one that increases towards low frequencies with a $1/f$-type slope

$$S_{\Phi_\mathrm{S}}(f) \simeq S_{\Phi_\mathrm{S}}^{\mathrm{white}} + S_{\Phi_\mathrm{S}}^{1/\mathrm{f}} \frac{1}{f^n}, \tag{2.32}$$

where $S_{\Phi_\mathrm{S}}^{1/\mathrm{f}}$ is the amplitude of the flux noise at $f = 1\,\mathrm{Hz}$ and n lies between 0.6 and 1. The second contribution is neglected here for simplicity, but in the numerical detector optimization it will be taken into account. The contribution to the noise equivalent power that is proportional to an energy sensitivity ϵ referred to the pick-up coil L_m can be calculated with (2.24) to be:

$$\mathrm{NEP}_\mathrm{SQ} = \tilde{p}^{-1}\sqrt{2\epsilon}\left[\frac{\partial\Phi}{\partial E}\frac{1}{\sqrt{L_\mathrm{m}}}\right]^{-1}. \tag{2.33}$$

Assuming a type of dc-SQUID used within the framework of this thesis with $\epsilon < 100\,h$ throughout the frequency band [Dru07], the corresponding NEP caused by the SQUID readout is 3.9×10^{-22} W. Comparing this NEP to the one originating from the thermodynamic fluctuations assuming a sandwich type detector with $F = 1$ the limitations on the energy resolution of an MMC are solely given by the fundamental energy fluctuations between the thermodynamic subsystems. Of course, any coupling loss between the paramagnetic sensor and the SQUID as well as filling factors below unity will directly effect the total NEP. For both cases the readout NEP will be of increasing importance and thus these losses in flux coupling should be kept small.

Another contribution to the noise that needs mentioning here has been observed in all MMCs so far. It is attributed to the magnetic moments of the sensor material Au:Er and shows a frequency dependence proportional to $1/f$. It does not show a dependence on temperature between 30 mK and 4.2 K and the noise power seems to be proportional to the number of erbium ions in the sensor. This noise contribution can be described by attributing a fluctuating magnetic moment with a spectral noise density of $S_\mathrm{Er} \simeq 0.1\mu_\mathrm{B}^2/f^\xi$ to each erbium ion, here μ_B is the Bohr magneton and the exponent ξ takes values close to unity. According to the other noise sources its

contribution to the NEP can be expressed as

$$\mathrm{NEP}_{\mathrm{Er}} = \tilde{p}^{-1}\sqrt{xF\mu_0\frac{N_\mathrm{A}}{V_\mathrm{mol}}S_{\mathrm{Er}}(f)}\left[\frac{\partial\Phi}{\partial E}\frac{1}{\sqrt{L}}\right]^{-1}, \tag{2.34}$$

where x is the concentration of erbium ions in the sensor, $V_\mathrm{mol} = 1.02\times10^{-5}\mathrm{m}^3/\mathrm{mol}$ the molar volume of the host material gold and N_A the Avogadro constant. For a realistic concentration of $x = 300\,\mathrm{ppm}$ this frequency dependent contribution will be dominant at frequencies below a few thousand hertz, at $f = 5\,\mathrm{kHz}$ it will contribute a NEP of $3.78\times10^{-22}\,\mathrm{W}$ (assuming $\xi = 1$). Clearly, as this noise contribution scales with the number of erbium ions it will have an impact on the detector design.

In addition, magnetic Johnson noise, i.e., thermal fluctuations of magnetic flux in the pick-up coil caused by random thermal currents in the metallic materials in the vicinity of the pick-up coil, is a further noise contribution present in MMCs that potentially limits the energy resolution. These contributions are considered in the numerical calculations but are found to be negligible for most geometries and thus are not discussed in detail here. Figure 2.8 displays an overview of the discussed noise contributions as a function of frequency.

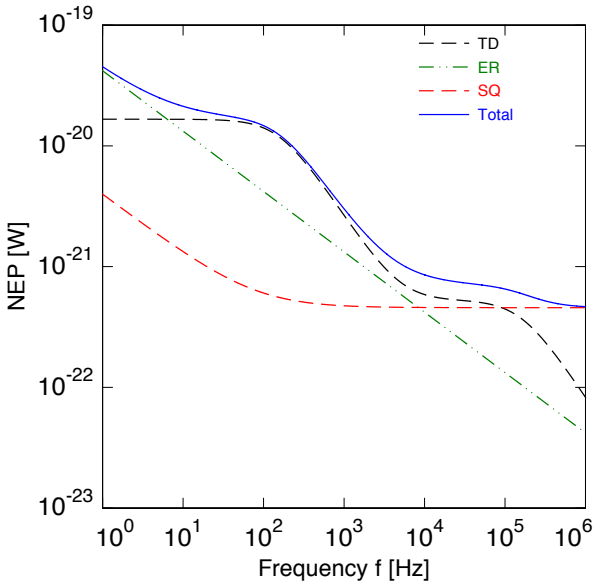

Figure 2.8 Different noise equivalent power contributions, (see text). A SQUID with $\epsilon = 40h$ and $\epsilon_{1/f} = 3000h$ is assumed as well as a sensor with an erbium concentration of $x = 700\,\mathrm{ppm}$.

Introducing the frequency and concentration dependent noise contribution $S_{\mathrm{Er}}(f)$ and including a frequency dependent SQUID noise term featuring a $1/f$-like behavior that realistically mimics a real SQUID noise makes the analytical analysis of the optimal design parameters more complex. Some general trends can still be summarized:

1. The noise power S_{Er} at low frequencies given by the magnetic moments is comparable to the one of the thermodynamic fluctuations of energy.

2. The contribution S_{Er} of the magnetic moments clearly favors a low concentration of erbium ions. This effect is even underlined by introducing a $1/f$-dependent SQUID noise. For the sandwich type coupling scheme the low frequency contribution of the SQUID does not have a big impact, as the erbium noise will be dominating, but for less optimal coupling schemes the $1/f$ type noise of the SQUID will become more important.

3. The introduction of S_{Er} and the resulting trend to favor low concentrations does not change earlier statements on the energy resolution drastically. It can be shown that even for concentrations as low as one-third of x_{opt} the factor in (2.25) still reaches a value of $\left[\sqrt{\mu_0/c}\,\partial M/\partial T\right] = 0.20/\sqrt{T}$, which is approximately 85% of its maximum. On the other hand, the low frequency contribution of the erbium ions is already greatly reduced at this concentration. To give an estimate for these quantities, evaluating (2.34) at a frequency of $f = 1/(2\pi\sqrt{\tau_0\tau_1}) = 5\,\mathrm{kHz}$, which defines the useful bandwidth of a detector with $\tau_0 = 1\,\mu\mathrm{s}$ and $\tau_1 = 1\,\mathrm{ms}$, yields a NEP $= \sqrt{x}\,2.18 \times 10^{-23}\,\mathrm{W}$ for a given concentration x in units of ppm. This shows that for concentrations of a few hundred ppm the NEP is comparable to the one of the high frequency part of the thermodynamic noise discussed above. In this limit the noise contributed by the magnetic moments of the erbium ions is smaller than the noise caused by energy fluctuations in almost the entire frequency range of interest (see figure 2.8) and consequently the minimally achievable energy resolution is only degraded by approximately a factor of 1.2.

4. Moving to concentrations even below $x_{\mathrm{opt}}/3$ the noise contribution of the erbium ions further decreases but as the factor $\sqrt{\mu_0/c}\,\partial M/\partial T$ declines more rapidly now, the signal size is largely reduced and the importance of the SQUID flux noise will increase and become the dominant contribution to the NEP, significantly degrading the energy resolution.

Having discussed all noise contributions we can get an estimate of the achievable energy resolution by calculating the total NEP

$$\mathrm{NEP}^2(f) = \mathrm{NEP}^2_{\mathrm{TD}}(f) + \mathrm{NEP}^2_{\mathrm{SQ}}(f) + \mathrm{NEP}^2_{\mathrm{ER}}(f) + \mathrm{NEP}^2_{\mathrm{J}}(f), \tag{2.35}$$

which is the sum in quadrature of the separate NEP terms considering their spectral shape mentioned above.

2.6 Position sensitive detection

In many applications a multi-pixel high resolution detector is desired. A straight forward way to achieve this would be to reproduce the single pixel as often as necessary. This scaling clearly will go along with a very complex readout, when the number of pixels becomes large. Since each pixel, as discussed so far, requires an individual readout chain, the multiplication of single pixels will be limited by the complexity of wiring, the corresponding heat load on the cryostat and the costs.

One method to implement more pixels while not changing the overall detector readout is to develop a detector that consists of multiple absorbers. This detector type is often referred to as *Hydra*, with reference to the multi-headed beast in Greek mythology.

A schematic of a Hydra detector is shown in figure 2.9. Four absorbers labeled 0 through 3 are connected with different thermal links to only one temperature sensor. The thermal conductance to the sensor is strongest for the absorber 0 and decreases gradually to absorbers with higher numbers.

On the right hand side of figure 2.9 a set of calculated signal shapes is displayed. The device is designed in such a way that the temperature evolution of the sensor with time depends on the absorber in which the particle was stopped. Each pulse shape shown represents a hit in a different absorber. The detection principle as well as the signal readout is identical to the one discussed in the previous sections for single pixel devices.

The events in the different absorbers can be separated by making a simple cut on the data according to the signal rise time. Therefore, the recorded events can be attributed to the individual pixels and energy spectra for each pixel can be extracted. The main advantage of such a device is that it reduces the total number of electronic channels required to read out a given number of pixels, effectively yielding

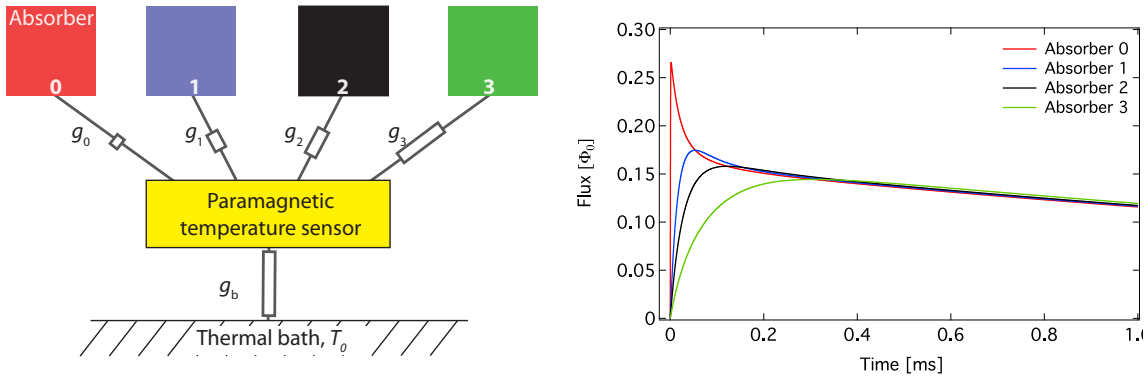

Figure 2.9 **Left:** Schematic of a position sensitive detector with four absorbers. **Right:** Modeled detector response for energy absorption in the different absorbers.

a multiplexed detector – one device with many sub-pixels.

A disadvantage of the augmented total absorber area is an increase of the total heat capacity C_{tot}, effecting the achievable energy resolution of such a device. Moreover, the achievable energy resolution will not be uniform across all pixels, as events in the individual pixels exhibit different signal-to-noise ratios. A second disadvantage of a device with an effectively larger absorber is of course a reduced treatable global count rate. Thus increasing the absorbers size will decrease the count rate capability.

In these devices, the method of tailoring the detector response is exploited to gain information on which of the absorbers was hit. Hence, a position sensitive device is created. Vice versa the same principle could be applied to eliminate position dependence within one absorber. In an absorber where the heat spreads diffusively an intrinsic position dependence will be observable. Whenever the variation in signal shape caused by particles absorbed at different locations in the absorber is significant, the energy resolution of the detector can be compromised. Creating a well defined thermal bottle neck for the heat transfer from the absorber to the thermometer acts like a thermal low pass filter. The heat is accumulated in the absorber first and traverses through the tailored link into the sensor. After this low pass filter the signal shape of events in all regions of the absorber are the same and a better energy resolution can be achieved.

A substantial part of this work was the development of a position-sensitive MMC design and its first demonstration. Most of this work took place at the MMC group at the NASA Goddard Space Flight Center (GSFC).

The detector consists of four discrete absorbers connected to a single magnetic sensor. Position-sensitive detectors have previously been developed [Smi08] based on superconducting transition-edge-sensor (TES) technology. Their design "inspired" the design presented here. A detailed description of the devices as well as thermal modeling and results representing the present record in resolving power for any position sensitive micro-calorimeter will be given in the sections 4.2 and 6.3.

2.7 Multiplexing concepts

Future applications of low temperature detectors such as neutrino mass measurements or X-ray astronomy are planned to consist of large detector arrays. For arrays of magnetic calorimeters the single detector channels need to be read out in a reliable and cost efficient way.

In the case of a gradiometric MMC design one SQUID readout channel is needed for every two pixels. When multiple energy absorbers are connected to only one temperature sensor as described in section 2.6, the signal for all pixels is read out by one SQUID measuring the change of magnetization of the only sensor. Combining

the gradiometric design with the Hydra concept one gains another factor of two in the number of pixels read out per SQUID. Hydra detectors have shown excellent results for designs with four pixels per readout channel based on MMCs presented later in this thesis [Por09] as well as based on TESs [Smi08]. This concept is currently extended towards devices featuring 9 or even 16 absorbers [Smi09a].

Obviously, the achievable count rate per pixel for these devices is reduced by a factor of at least $1/n$, where n is the number of pixels connected to one temperature sensor. The maximal achievable count rate is even lower as the signal rise time is slowed down for these devices. Considering applications, for example the outer focal plane elements of future X-ray astronomy missions [Gen09, Wol08], this is not a drawback. Wherever the expected count rates are relatively small this approach is a very promising concept.

Some other applications may not allow for slowing down the rise time of the detector. As discussed in section 1.4.3, the sensitivity of a neutrino mass measurement with rhenium absorbers will be degraded by slower rise times as the unresolved pileup will increase for a given decay rate per pixel.

In order to fulfill the requirements of this type of experiments not only the single channel detector performance is important but also the feasibility to build and run the entire experiment. The difficulty and cost of routing leads from each SQUID to room temperature and read out each SQUID with a dedicated electronics is eminent. These challenges have motivated efforts to cryogenically multiplex SQUIDs. Two classes of multiplexers are under current investigation: time division mulitplexers [Dor04, Che99, dK03, Rei03] and frequency division multiplexers [Yoo01, Cun02, vdK02, Irw04].

In a time domain multiplexing scheme as shown on the left of figure 2.10 each temperature sensor is read out by its corresponding SQUID. The readout of those is multiplexed by the following technique: the second stage SQUIDs are sequentially addressed or biased into their flux-sensitive stage. When in the superconducting state, the SQUIDs attributed to that pixel do neither contribute signal nor noise. The output of the second stage SQUID can be routed to another amplifying SQUID stage at low temperatures or can directly be read out by room-temperature electronics.

The sequential switching from one channel to the next reduces the time resolution of each channel by $1/n$, where n is the number of multiplexed SQUID channels. The signal is electronically or thermally low pass filtered before readout in order to provide a reliable feedback of each channel. Again this multiplexing technique represents a very powerful tool to readout multiple channels, but as for the position sensitive device it is not suitable for applications where fast response times or very high count rates are required.

A frequency domain multiplexing scheme is shown on the right of figure 2.10. Superconducting tank circuits with different resonance frequencies are coupled to

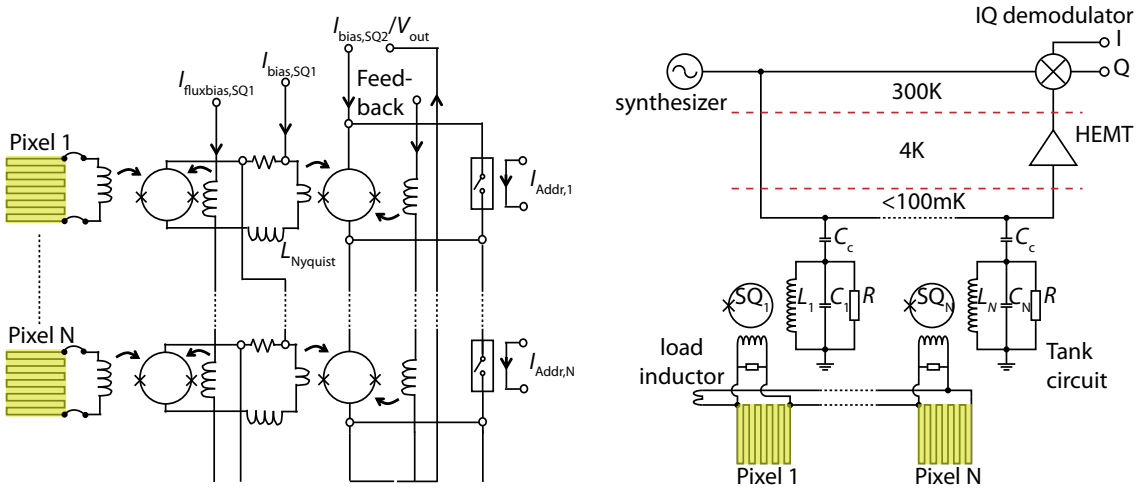

Figure 2.10 **Left:** Scheme of a time domain multiplexed readout. **Right:** Scheme of a microwave-SQUID multiplexed readout.

a common transmission line and each of these resonators is coupled to a different rf-SQUID. An rf-SQUID ideally functions as a flux-variable inductor [Cla04]. Each readout channel in this type of multiplexer consists of a superconducting resonant circuit coupled to an rf-SQUID. A signal produced by one of the detectors induces a current in the input coil of the corresponding SQUID. The flux change in this SQUID loop varies its inductance and by this the resonance frequency of the resonator is shifted. Every resonator in the so called microwave SQUID multiplexer occupies an individual frequency band and many of those can couple to a common transmission line. The readout of a detector array is accomplished by injecting a microwave frequency comb function containing a sine wave at the resonant frequency of each of the resonators into the feed line. Each resonator picks out one particular excitation signal while passing on all of the remaining ones unchanged. Each pixel of the detector will imprint its current state (temperature) on the corresponding carrier signal. The signal is then amplified at 4 K with a single cryogenic amplifier (HEMT), which has a noise temperature below 3 K and brought outside the cryostat with a single coaxial cable. At room temperature the amplitude and phase of each injected tone are mixed down to the base band and are monitored.

This technique allows to multiplex even fast signals as a bandwidth of several megahertz can be attributed to each channel by operating the described setup in the frequency band between 4 GHz and 8 GHz. This technique might be limited by the data processing at room temperature where enormously fast ADC converters and digital processing algorithms are required. It is worthwhile to mention that in this

scheme thousands of detectors could be read out with only one coaxial cable. Apart from all complexities of this readout scheme involved in the micro-fabrication, the exact design and the optimization of the elements (e.g., resonators and rf-SQUIDs), it benefits by moving a majority of the complexity from the base temperature to room temperature where the vast knowledge of microwave technology and fast digital electronics can be exploited. As a single channel readout would require 6 to 8 wires per channel, the heat load on the cold stages of a refrigerator alone would not allow for an experiment with thousands of pixels. From all proposed multiplexing schemes this is the most promising for an application like the rhenium experiment. Currently, enormous efforts are made in the community to further develop the microwave multiplexing technique. Probably, the most advanced project with respect to this multiplexing scheme is the **AR**ray **C**amera for **O**ptical to **N**ear-IR **S**pectrometry (ARCONS), that uses an array of $32 \times 32 = 1024$ Microwave Kinetic Inductance Detectors [Day03] read out with a frequency multiplexer [Maz10]. It will be employed in the Palomar observatory in 2011. This will also include a fully digital readout that is currently developed [CAS]. There are also substantial efforts being made in our MMC group in Heidelberg to develop the required components as rf-SQUIDs and resonators; an adequate cryogenic environment is already set up.

Part II

Experiment

Chapter 3

Cooling Techniques and Readout

3.1 Cryogenics

The detector system described in the previous chapter requires a working temperature well below $T = 100\,\mathrm{mK}$ to allow for an energy resolution in the range of a few electron volts. An overview of standard cooling techniques to millikelvin temperatures can be found in [Ens05, Pob07]. In the context of this work two different adiabatic electron spin demagnetization refrigerators (ADR) and a dilution refrigerator (DR) have been used. This section is not meant to discuss the well-known cooling techniques but to introduce the individual cryostats.

3.1.1 Adiabatic demagnetization refrigerator

Two different ADR systems have been used for the experiments carried out in Heidelberg and at Goddard, respectively. Both cryostats feature only one isolating vacuum space. For pre-cooling and as a thermal shield of the experimental platform at millikelvin temperatures liquid nitrogen and helium are filled in designated reservoirs. Radiation shields connected to the reservoirs surround the colder parts of the cryostat to reduce the heat input on them. The helium bath can be pumped to reach a base temperature of down to $T = 1.5\,\mathrm{K}$ as a starting point for the adiabatic demagnetization cycle.

The ADR in Heidelberg

The ADR used in Heidelberg is a two-stage system with two different paramagnetic salt pills (GGG[1] and FAA[2]).

Both pills are suspended by Kevlar strings for thermal isolation. The GGG pill is suspended from the helium platform and reaches a temperature around $T = 300\,\mathrm{mK}$ after demagnetization. This intermediate temperature stage can be used to heat

[1] Acronym for **G**adolinium **G**allium **G**arnet: $Gd_3Ga_5O_{12}$
[2] Acronym for **F**erric **A**mmonium **A**lum: $Fe_2(SO_4)_3(NH_4)_2SO_4 \cdot 24H_2O$

sink wires on their way to the colder FAA pill. The FAA pill is suspended by Kevlar strings from the GGG pill and represents the coldest stage in the cryostat. It reaches temperatures of around $T = 23\,\mathrm{mK}$. After reaching the base temperature warming rates as low as $0.1\,\mathrm{mK/h}$ were achieved, corresponding to a hold time at $T < 30\,\mathrm{mK}$ of 2 days.

Both pills are located within the bore of a single magnet. Thermal contact of the pills to the helium bath is achieved by a mechanical heat switch that is operated by a motor. An experimental platform is connected to the FAA pill, where the SQUIDs and detectors discussed in this thesis were installed.

For calibration of the installed detectors, X-ray sources are installed on a platform at liquid helium temperature.

The entire fridge, as well as the necessary electronics are located in a Faraday cage to shield the interior from external electromagnetic radiation. Inside the Faraday cage a battery-driven voltage supply can be used to reduce noise pick-ups, e.g. the 50 Hz-hum and its harmonics via the power supply from the mains.

The ADR at Goddard

The main features of the ADR at Goddard are identical to the ADR in Heidelberg. However, it is a single-stage system with only an FAA salt pill.

A superconducting niobium box is permanently installed to the FAA stage of the cryostat. All experiments are mounted on a circuit board. This board is then installed in the niobium box so the experiments are shielded against magnetic stray fields. The cryostat has X-ray windows in each radiation shield, so the X-ray sources can be placed outside the cryostat. The window in the vacuum chamber is made of beryllium, the X-ray windows on the niobium box are made of thin aluminum foil.

The possibility to place the X-ray sources outside the cryostat gives the opportunity to characterize the installed detectors with and without X-ray irradiation in the same experimental run. The absorption of the windows at photon energies above $E = 3\,\mathrm{keV}$ is negligible. Approximately one half of the cryostat, the part where the experiments are located, can be placed in a mu-metal shield to screen static or low-frequency magnetic fields.

3.1.2 Dilution refrigerator

In the context of this work, also a dilution refrigerator (DR) was used. Figure 3.1 shows a schematic as well as a photograph of the cryostat. In the DR used within this work the thermal shielding is accomplished by an onion-like assembly of thermal shields (3) and (4). These aluminum shields are connected to the nitrogen bath (1), the helium bath (11) and the still (5), successively reducing the thermal radiation on the mixing chamber (8) and the experimental platform (16).

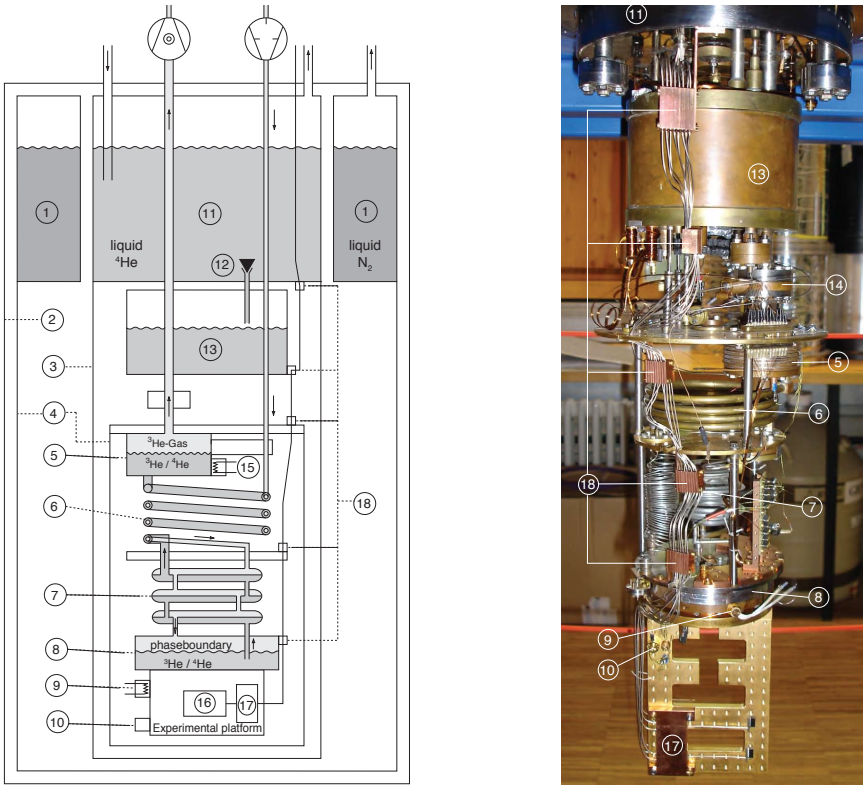

Figure 3.1 Schematic (left) and photograph (right) of the DR used: (1) nitrogen bath, (2) outer vacuum chamber, (3) inner vacuum chamber, (4) radiation shields, (5) still, (6) continuous heat exchanger, (7) step heat exchanger , (8) mixing chamber, (9) mixing chamber heater, (10) thermometer, (11) helium bath, (12) needle valve, (13) 1K-pot, (14) film burner, (15) still heater, (16) experimental platform, (17) SQUD connectors, (18) thermal anchoring of wires. More details in [Bur09]

The most important part of the refrigerator for the experiments is the coldest point of the refrigerator: the mixing chamber (8). A gold plated copper platform is connected to the mixing chamber, where the experiments can be mounted. The experimental platform of the cryostat reaches a base temperature of approximately 17 mK.

3.1.3 Temperature control

For all cryostats the temperatures are determined with calibrated resistive thermometers. Temperature regulation is realized with proportional-integral-derivative (PID) controllers.

In an ADR that does not supply continuous cooling power the temperature is regulated by controlling the magnetic field for the paramagnetic pill. The DR tem-

perature is regulated by adjusting the thermal load on the mixing chamber using a resistive heater.

Depending on the temperature resolution of the thermometer at a given temperature and on the quality of the PID settings, a temperature stability between 1 μK and 10 μK was achieved.

3.1.4 Wiring

For all described cryostats the heat sinking of the wires for SQUID readout or any other support lines is of vital importance. To reduce the heat load on the cold stage of the ADRs or the mixing chamber of the DR the wires are heat sunk at several temperatures in the cryostat. All described cryostats are capable to run four two-stage SQUID setups and support four MMCs with field and heater currents. For most experiments the wires form twisted pairs to reduce pickup of electromagnetic noise. Additionally, some of the wiring is shielded in niobium capillaries.

3.2 Data acquisition

The data acquisition is realized similarly for all experiments covered within this thesis. It is depicted schematically in figure 3.2. The detector output is amplified and linearized by the SQUID electronics[3]. Afterwards the signal is split up in two channels and pre-processed by low noise preamplifiers and band-pass filters. Both channels can be filtered individually. One channel is usually filtered and amplified strongly to be useful as a reliable trigger for data acquisition. The other channel serves as the signal and is filtered according to the purpose of data acquisition.

The signals are digitized by an ADC card. The ADC cards have different voltage resolution. For the characterization of the signal shape as well as spectroscopy with resolving powers $E/\Delta E$ below 2500 a 12 bit resolution is sufficient to not be limited by the noise of the data acquisition. However for high resolution detectors a higher resolution of 14 bit is favorable.

After digital signals are then processed. An online analysis is performed to allow for selective data acquisition.

Data are acquired on the basis of a trigger threshold that can be set in the software. Time windows of chosen length are acquired with a preset sampling rate. For the work within this thesis a typical recorded MMC signal for example consists of 16384 voltage samples within a time window of 800 μs to 160 ms. Usually one quarter of the samples are prior to the trigger to be sensitive on pretrigger offsets. These can for example be caused by temperature variations or by pulse pile-ups. The data is stored in a binary file allowing an offline analysis of the raw data.

[3]XXF, Magnicon, Hamburg, Germany.

A thorough analysis of the noise present in the detector signal is provided by acquiring baseline signals. These recorded timeframes are not triggered by overstepping the trigger level and do not contain a pulse shaped signal.

The software is also capable to simultaneously receive a temperature information via a network client, this allows for example data acquisition during a temperature sweep also providing the temperature information for each stored time window.

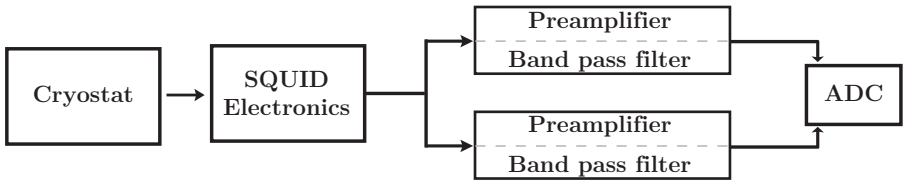

Figure 3.2 Schematic of the data acquisition.

3.2.1 Data analysis

Data analysis can be performed based on the concept of the optimal filter or on a time domain based algorithm. The optimal filter concept is discussed in detail in literature [Szy93, Fle03]. It is based on the frequency spectrum of signal and noise and is only "optimal" under certain conditions:

1. The detector response is linear. This means that, except for the amplitude, the pulse shape $s(t)$ of each photon signal will be identical, to that of every other photon irrespective of the energy.

2. The noise is stationary. The spectral amplitude and spectral shape of the noise is constant in time.

For different reasons the first condition is possibly not fulfilled by all detector signals. For example the detector could saturate for high photon energies or the pulse shape can vary depending on the position where the particle is stopped in the absorber.

For the devices discussed a saturation of the detector signal is not expected. Certainly, a position or rather an absorber index dependence is expected for the Hydra detectors. In this case the signals can be accounted to the individual absorbers by a rise time criterium. Within these subgroups the signal shape should be identical and the optimal filter can be applied to those.

Besides the data analysis based on the concept of the optimal filter it is also possible to conduct an thorough offline analysis. As for some experiments the main

criterium for a well functioning optimal filter – namely that the pulse shapes are not identical for all events – is not fulfilled, in some cases it is beneficial to rely on a time domain analysis of the data.

The time domain based algorithm assigns an energy input to each individual recorded event. It is assumed that all signals are identical except for a vertical offset and a multiplicative factor. To assign an energy to each signal $s(t)$ a reference signal $r(t)$ is created by averaging several signals of known energy. The algorithm now finds the offset V_0 and the scaling factor E of reference that minimize the sum of the quadratic deviations from the single signal for all samples of any given recorded signal $s(t)$

$$\chi^2 = \sum_i \left(s(t_i) - Er(t_i) + V_0\right)^2 . \tag{3.1}$$

Chapter 4

Detector Development

For the current work a new MMC detector, specifically for measuring the rhenium β-spectrum, was optimized, designed and fabricated. The design is based on results from numerical optimizations taking into account all relevant noise contributions as discussed in section 2.5. All current knowledge on micro-fabricating magnetic calorimeters as well as empirical understanding of previous experiments with rhenium absorbers were incorporated in the development and are described in this chapter. In section 4.1.2 the detector designs that were studied are introduced in detail.

4.1 Development of an MMC for a rhenium experiment

Driven by first promising results with MMCs for β-spectroscopy on superconducting rhenium achieved within the last years, a new generation of detectors was developed.

The new development directly addresses two fields of study: an optimized detector for β-spectroscopy on rhenium and a detector platform to study superconducting absorbers.

The design of a new generation of detectors relies on all available micro-fabrication techniques developed so far [Bur08]. A transformer-coupled double-meander with a center-to-center distance (pitch) of the field generating niobium stripes of $p = 6\,\mu$m was chosen as basis for optimization and design.

In a planar meander based detector geometry the magnetic field strength distribution at a distance d above the meander decays $\propto \exp(-d/p)$. This requires the sensor to be deposited as close as possible on top of the meander-shaped coil to achieve good filling factors. For the developed detector a metallic contact between sensor and absorber is desired to allow for signal rise times as short as possible. To achieve this a diffusion welding process was developed that will be described in some detail in section 5.2.

4.1.1 Optimization

The detector developed for this work is designed for the use with a superconducting rhenium absorber.

The developed optimization programs are based on the detector theory discussed in section 2.5. The boundary conditions for optimization were guided by the following thoughts and chosen as described in the following:

β-rate The activity per volume for natural rhenium is given by

$$\frac{A_\beta}{V_{\mathrm{Re}}} = 0.626 \frac{N_{\mathrm{A}} \ln 2}{V_{\mathrm{mol}} \tau_{1/2}} = 22 \, \frac{\mathrm{Bq}}{\mathrm{mm}^3}, \tag{4.1}$$

with the natural abundance of 62.6% of the isotope ^{187}Re, the molar volume of rhenium of $V_{\mathrm{mol}} = 8.86\,\mathrm{cm}^3$, the half-life of ^{187}Re $\tau_{1/2} = 43.2\,\mathrm{Gy}$ and Avogadro's number N_{A}. For the optimization of the detector an activity of 1 Bq was chosen for reasons of avoiding unresolved pileup events as discussed in section 1.4. This corresponds to a rhenium cuboid of $0.25 \times 0.25 \times 0.74\,\mathrm{mm}^3$.

Handling As is discussed in further detail later, the rhenium absorber needs to be well thermally coupled to the sensor by a metallic link. The attachment of the absorber to the sensor is achieved by diffusion welding. This process is done by hand and thus neither absorber nor sensor should be too small. From experience a detector area equal or larger than $250 \times 250\,\mu\mathrm{m}^2$ is a suitable size for this.

Heat capacity Although the superconducting rhenium absorber should hardly contribute to the heat capacity of the detector, recent experiments [Por08, Kir10] have shown that heat capacities of several pJ/K are observed in these systems. The optimization should leave room for these heat capacities and be flexible concerning these. In general this means that the sensor volume should not be chosen too small, in which case the optimal detector performance given for $C_{\mathrm{s}} = C_{\mathrm{a}}$ cannot be reached.

SQUIDs As described before, a transformer coupling scheme is used for current micro-fabricated devices. For this layout two pick-up loops with inductances L_{M} in parallel are micro-fabricated and then wire bonded to a SQUID with given input coil inductance L_{i}. Two types of SQUIDs are currently provided by the PTB Berlin, featuring input inductances of 1.8 nH and 22.3 nH, respectively. Although also SQUIDs with different input inductances might be developed in future, it is unlikely that these will have much smaller input inductances than the mentioned 1.8 nH. SQUIDs with even lower input inductances would suffer from coupling losses due to unavoidable stray inductances, e.g. of the bonding wires. Hence, for developing a high resolution X-ray detector

with small absorber heat capacities in the order of 1pJ/K the current generation of SQUIDs with $L_\mathrm{i} = 1.8\,\mathrm{nH}$ are assumed as boundary condition in the optimization of the detector geometry.

As noticed in the previous section, the SQUID noise is one of the most important contributions to the NEP, especially in a transformer-coupled layout. The SQUID noise should therefore be estimated realistically before starting optimization calculations as it might substantially influence the optimal value of the other free parameters. For the design of the current generation of detectors a defensive route was chosen, assuming SQUIDs that have a $1/f$-type noise contribution with an amplitude of $\sqrt{S_{\Phi_\mathrm{S}}^{1/\mathrm{f}}} = 10\,\mu\Phi_0/\sqrt{\mathrm{Hz}}$ at 1 Hz and a white noise contribution of $\sqrt{S_{\Phi_\mathrm{S}}^{\mathrm{white}}} = 0.5\,\mu\Phi_0/\sqrt{\mathrm{Hz}}$. The flux noise of state of the art SQUIDs can be up to a factor of two lower than the ones chosen here [Dru07].

Taking the fundamental and practical consideration mentioned above into account, optimal values for most parameters of the detector design can be defined.

For these calculations an exponential signal rise time of $\tau_0 = 10\,\mu\mathrm{s}$ is assumed. This relatively slow signal rise time compared to high resolution X-ray detectors ($\approx 100\,\mathrm{ns}$) is chosen to take into account a possibly slower thermalization within the absorber. The slower rise time will effectively increase the high frequency plateau of the noise caused by thermodynamic energy fluctuations and does not have a severe impact on the optimization of the parameters.

The decay time for the numerical optimization is set to $\tau_1 = 1\,\mathrm{ms}$. This rather fast thermal decay time is chosen to get an conservative estimate of the achievable energy resolution. Any weaker thermal links to the bath will reduce the plateau value of the low frequency noise given by thermodynamic fluctuations and thus enhance detector performance.

The SQUID performance is set to the level described above. In the calculation for the flux coupling (see equation (2.19)) a stray inductance of $L_\mathrm{str} = 0.5\,\mathrm{nH}$ was assumed.

The results of the optimization are summarized in table 4.1. The results are presented assuming a temperature independent absorber heat capacity of 1 pJ/K and 10 pJ/K, respectively. The operational temperature of the detector is chosen to be 30 mK and 50 mK, respectively.

The relevant parameters for a detector design as the sensor side length l_s and height h_s are shown as well as the meander inductance L_M of a meander with pitch $p = 6\,\mu\mathrm{m}$ completely covered by the sensor. Also the optimal erbium concentration x and field generating current I are shown. The resulting flux change in the SQUID per unit of absorbed energy $\partial\Phi/\partial E$, and the achievable energy resolution ΔE_FWHM are presented in the last two columns.

Table 4.1 Summary of detector optimization. Assumptions and boundary conditions: $\tau_0 = 10\,\mu$s, $\tau_1 = 1\,$ms, $\sqrt{S_{\Phi_S}^{1/f}} = 10\,\mu\Phi_0/\sqrt{\text{Hz}}$ at 1 Hz, $\sqrt{S_{\Phi_S}^{\text{white}}} = 0.5\,\mu\Phi_0/\sqrt{\text{Hz}}$, $L_i = 1.8\,$nH, $L_{str} = 0.5\,$nH, optimal values were the corresponding parameter was not evolved freely are denoted by a star (*).

T [mK]	C_a [pJ/K]	C_s [pJ/K]	l_s [μm]	h_s [μm]	L_M [nH]	x [ppm]	I [mA]	$\partial\Phi/\partial E$ [mΦ_0/keV]	ΔE_{FWHM} [eV]
30	1	1.3	171	1.3	1.76	293	40	41.5	2.6
30	1	1.5	245*	1.1	3.58	252	31	40.6	2.7
30	10	9.8	245*	1.5	3.58	663	56	20.0	6.9
50	1	1.4	172	1.3	1.76	340	60.0	26.4	4.4
50	1	1.7	245*	1.1	3.58	294	49	25.4	4.5
50	10	9.8	245*	1.5	3.58	242	80	13.7	10.9

Both for 30 mK and 50 mK the first two lines represent the optimization for $C_a = 1\,$pJ/K absorber heat capacity. In the first line the meander area was varied freely, whereas in the second line a minimal sensor side length of $l_s = 245\,\mu$m was chosen as a boundary condition.

Assuming a heat capacity of the absorber of $C_a = 1\,$pJ/K a theoretical energy resolution ΔE_{FWHM} below 3 eV or below 5 eV can be reached at 30 mK and 50 mK, respectively.

Even if a ten times larger heat capacity of $C_a = 10\,$pJ/K is assumed the achievable energy resolution would be below 7 eV or 11 eV, respectively. Such a detector would perfectly meet the requirements for a rhenium experiment defined in chapter 1.

The detector showing the lowest energy resolution has a meander side length of $l_s \approx 170\,\mu$m. As discussed before, a larger area detector is preferred. Therefore the influence of the detector area on the energy resolution is studied and the results are also presented in table 4.1.

From the results it is evident that, although the best achievable energy resolution of $\Delta E_{FWHM} = 2.7\,$eV is found for a geometry where the sensor and meander have a side length of approximately $l_s = 170\,\mu$m, a similarly good result is achieved for a meander with a side length given by the lower bound of $l_s = 245\,\mu$m. Here, the energy resolution is degraded by less than 5%, solely a different sensor thickness, erbium concentration and field generating current is required to reach this value.

The same analysis was done for the large absorber heat capacity of 10 pJ/K. Here equivalent observations were made; the minimum of the achievable energy resolution with respect to meander side length is extremely flat and setting a boundary condition by fixing the side length to $l_s = 245\,\mu$m changes the theoretically achievable energy resolution by a few percent only.

Lead by this analysis a detector design was elaborated that has a meander side length of $l_s = 245\,\mu$m simplifying the process of absorber attachment.

Another conclusion that can be drawn from the optimization results presented above is the fact that a detector of this dimension will exhibit good performance over a wide range of absorber heat capacities. For this only the heat capacity of the Au:Er sensor needs to be adapted, namely by changing its concentration and thickness. Thus the same set of masks for micro-fabrication is suitable for a variety of absorber heat capacities.

4.1.2 Detector design

Rhenium experiment

Driven by the results of the optimization, a mask layout for the photo-lithographic micro-fabrication was developed. In this section the detector design is described.

A schematic of the detector layout is depicted in figure 4.1. The detector chip has a size of $3.5 \times 3.5\,\mathrm{mm}^2$ and the detector itself consists of two meander-shaped pick-up coils that form a gradiometric loop (like in the schematic of figure 2.5a)). Each meander fills a square with a side length of $l_s = 245\,\mu$m. The two loops can be covered with one or two paramagnetic Au:Er sensors and can be connected to the input coil of a SQUID via superconducting aluminum wire bonds from the labelled SQUID bond pads.

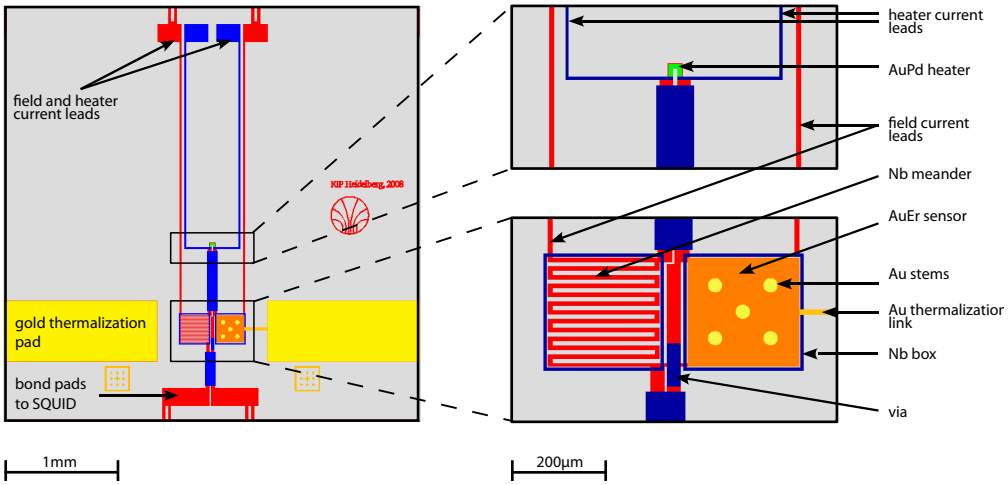

Figure 4.1 Schematic of the developed MMC design. Structures depicted in different colors are fabricated in different layers.

As mentioned before, the superconducting niobium pick-up coil is not only used to read out changes in magnetization but also to store a persistent current I_f that provides the necessary magnetic field for the sensor. In order to prepare this persis-

tent current, a thermal switch is needed that can interrupt the superconducting loop as well as another set of leads to connect a current source.

A resistive heater is used for switching. It is located above an extension of the meander circuit and is electrically insulated from it. The heater consists of nine squares of a resistive gold palladium alloy. By driving a current – typically a few milliamperes – through this heater, the meander's structure located underneath the heater is locally heated above the critical temperature of niobium of $T_C = 9\,\mathrm{K}$, thereby allowing flux penetration into the superconducting loop while a current I_f is injected through the field current leads. Specifically for this design the heater is relatively far away ($500\,\mu\mathrm{m}$) from the meander so that during the heating procedure the rhenium crystal – located above the meander – is not heated to the normalconducting regime.

The decay time of the detector temperature after absorption of a particle is determined by the total heat capacity and by the thermal conductance between the sensor and the thermal bath. This thermal link is realized with a narrow metal link made of sputter deposited gold between the sensor and a large gold pad. As the mask determines the width and length of this stripe the thickness of the metallic link can still be varied in order to achieve the desired decay times. The mentioned gold pad is designed to have a sufficient heat capacity to act "almost" as a thermal bath itself but additionally it can be thermally coupled to the metal chip holder by gold wire bonds.

Moreover, the detector design features a superconducting box around the meanders that should provide shielding against external magnetic fields. Stray inductances, effectively reducing the signal coupled to the SQUID, are kept as low as possible by covering any leads in the first niobium layer by a superconducting ground plane in the second niobium layer.

An additional feature can be found on the sensor. Five gold stems arranged like the number "5" on a dice are electroplated onto the sensor. Each stem has a diameter of $d = 30\,\mu\mathrm{m}$. The center-to-center side length of the square formed by the outer four stems is $120\,\mu\mathrm{m}$. These stems were designed to provide defined contact areas where absorbers can be welded to. Placing the absorber on stems, effectively reducing the contact area from absorber to sensor, will furthermore reduce the probability of losing athermal phonons to the substrate. In the development of MMCs for high resolution spectroscopy it was observed that this phonon loss can lead to low energy tails of mono-energetic lines in recorded energy spectra. It has been shown that reducing the contact area is an effective method to reduce this low energy tail and thus to improve the performance of high-resolving detectors [Fle09a]. In this specific design a small contact between the absorber and the sensor might be of enormous importance as the thermalization in a superconducting absorber might involve an initial thermalization phase where a large number of athermal phonons are produced.

4.2 Design of a four pixel detector – Hydra

The position sensitive devices discussed here were developed at the NASA Goddard Space Flight Center (GSFC). The underlying working principle is the same as for the detectors discussed in the previous section. Some differences should be pointed out. First, this MMC is given by a temperature sensor on a single meander that directly couples to the input coil of a SQUID. Second, the detector is designed to be fabricated on thin membranes to reduce the amount of heat lost to the substrate on the relevant time scales. A schematic of a position sensitive device featuring four absorbers is shown in figure 4.2.

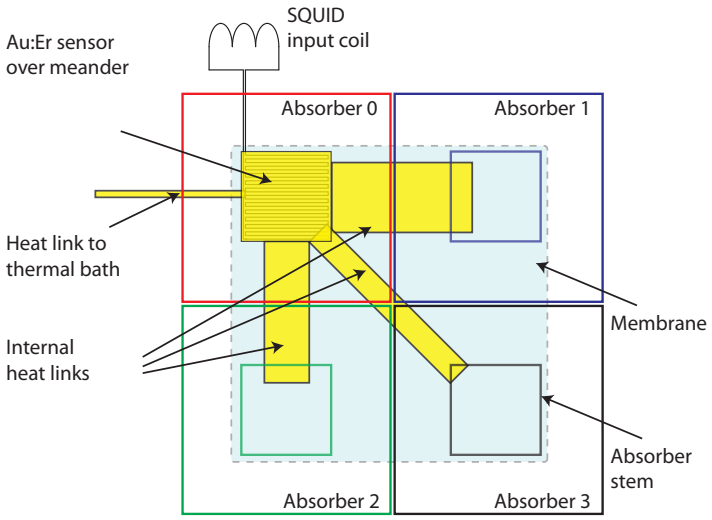

Figure 4.2 Schematic of the developed four-absorber Hydra.

The detector is based on a single meander-shaped pick-up coil covering an area of $100\,\mu\text{m} \times 100\,\mu\text{m}$ and with a center-to-center distance of the stripes of $p = 5\,\mu\text{m}$. The same meander has also successfully been used for single absorber magnetic calorimeters [Ban09, Hsi09]. The Au:Er sensor is located above the meander, with a 300 nm thin Al_2O_3 insulation layer in between. For the Hydra, four electroplated absorbers $250\,\mu\text{m} \times 250\,\mu\text{m} \times$ Au($1\,\mu$m)/Bi($6\,\mu$m) are thermally connected to the sensor via heat links of different thermal conductances. Absorber 0 is fabricated as an overhanging absorber directly on top of the sensor making it the absorber most strongly thermally coupled to the sensor. The three other absorbers are deposited directly on the $450\,\mu\text{m} \times 450\,\mu\text{m} \times 0.5\,\mu\text{m}$ silicon-nitride membrane. The link between the absorbers (1, 2 and 3) and the sensor as well as the thermal link of the sensor to the heat bath are made of evaporated gold. The thermal conductance of each link can be parameterized by the number of fabricated squares $n_\square$ the link consists of

$$n_\square = \frac{l}{w}, \tag{4.2}$$

Table 4.2 Design parameters of the thermal links.

Link	**Number of squares**	**Ratio to $G_{\mathbf{bath}}$**
Abs. 0 to bath	35	1
Abs. 0 to sensor	$\sim 5 \times 10^{-4}$	70000
Abs. 1 to sensor	1.7	20.6
Abs. 2 to sensor	3.4	10.3
Abs. 3 to sensor	8	4.4

with l and w denoting the length and the width of the link, respectively. Table 4.2 summarizes the lengths of the links in units of squares, and the ratio of the corresponding thermal conductance in comparison to the link to the bath.

Chapter 5

Fabrication and Detector Setup

5.1 Micro-fabrication

The micro-fabrication techniques used in the production of the devices for the rhenium experiment in Heidelberg and the position sensitive devices fabricated at the Goddard Space Flight Center (GSFC) are very similar for most layers. A brief description of the micro-fabrication of devices in Heidelberg is given here, as well as some distinctive features of the GSFC fabrication.

5.1.1 Rhenium detector

The detectors were fabricated on the polished side of 2 inch sapphire wafers[1] with a thickness of 330 μm. The detector design comprises of 8 photolithography masks and the entire detector consists of seven deposited layers, not counting the sticking or sacrificial layers that do not have a specific functionality to the detector itself. Most layers are deposited using a commercial ultra high vacuum sputtering-system[2]. Scanning electron microscope pictures of the fabricated devices for the rhenium experiment are shown in figure 5.1, details are given within the caption.

The first layer is a continuous, 400 nm thick sputtered layer of niobium. The meander-shaped pick-up coils are structured by means of wet etching. To achieve electrical insulation from all succeeding layers except for areas functioning as vias or bond pads, all first layer structures are anodized and covered with a 200 nm thick SiO_x insulation layer. The critical currents of the 2.5 μm $-$ 3 μm wide lines have been measured to exceed values of $I_c = 150\,\mathrm{mA}$, which can be translated into critical current densities beyond $i_c = 15\,\mathrm{MA/cm^2}$ and is more than two times larger than what is required for optimal performance of the MMCs discussed within this thesis.

The injection of the field generating persistent current is enabled by a persistent current switch. The switch is formed by positioning a resistive heater on top of the

[1] CrysTec GmbH, Berlin, Germany.
[2] DCA instruments Oy, Turku, Finland.

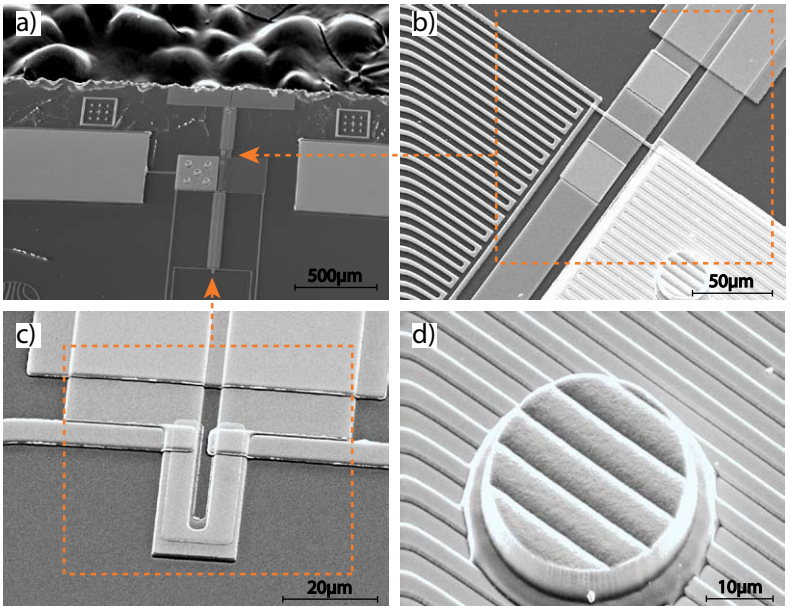

Figure 5.1 Scanning electron microscope pictures of fabricated devices. **a)** Overview of chip. **b)** Zoomed-in view showing the meander stripes of a bare niobium meander and a meander covered with Au:Er sensor as well as two via structures. **c)** Close-up view showing persistent current switch heater. **d)** Zoomed-in image showing one of the five electroplated gold stems. An imprint of the underlying niobium stripes is visible.

end of a prolongation of the niobium meander structure. The prolongation has the shape of a U with a length of approximately $500\,\mu$m. The heater is positioned on the turning point of the U and is meant to heat the subjacent niobium above its transition temperature ($T_\mathrm{c} \simeq 9\,\mathrm{K}$). The minimal heating should be employed to prevent driving the entire meander in the normal conducting state. The heater is deposited in the third layer and is a nominally 75 nm thick gold-palladium structure which is sputter-deposited on a 5 nm thick titanium sticking layer. The fabricated heaters extend over nine squares and typically show resistances between 30Ω and 50Ω. To heat the niobium above its critical temperature, heater currents of $I_\mathrm{h} = 2 - 4\,\mathrm{mA}$ are usually needed.

The second niobium layer is sputtered in the fourth layer. It is approximately 400 nm thick and structured using a liftoff process. Necessary leads, ground planes for lines in the first niobium layer as well as the top parts of vias are fabricated in this layer.

In the fifth layer, gold is sputtered onto a few nm thick niobium sticking layer. The structures in this layer are used to define the thermal link between the Au:Er sensors and a large area gold pad. The thermal heat sinks are 20 squares long and have a nominal thickness of 200 nm for these devices. Furthermore, the structures function both as an electrical lead and a seed layer for subsequent electroplating.

The Au:Er sensors are simultaneously sputtered from a pure (5N) gold target and a Au:Er target with an erbium concentration of 850 ppm, here the erbium concentration of the sensor material is varied by adjusting the ratio of the power used for the sputter guns. The gold erbium sputter target was produced in our group from 5N purity gold[3] and isotopically enriched ^{166}Er[4]. To improve adhesion to the insulating dielectric below the sensors are deposited on a 1 nm − 2 nm thick niobium sticking layer. In the seventh and last layer, 5 μm to 10 μm thick gold stems and the large thermalization pads are electroplated into photoresist molds using a commercial electrolyte[5].

5.1.2 Hydra detector

The fabrication of the Hydra detector is very similar. Pointing out all of the differences will not contribute to an understanding of the device, therefore, only additional features are discussed. A summary of the fabrication of the device can be found in [Hsi09]. Electron microscope images and a light microscope picture of the position sensitive device discussed within this thesis are shown in figure 5.2.

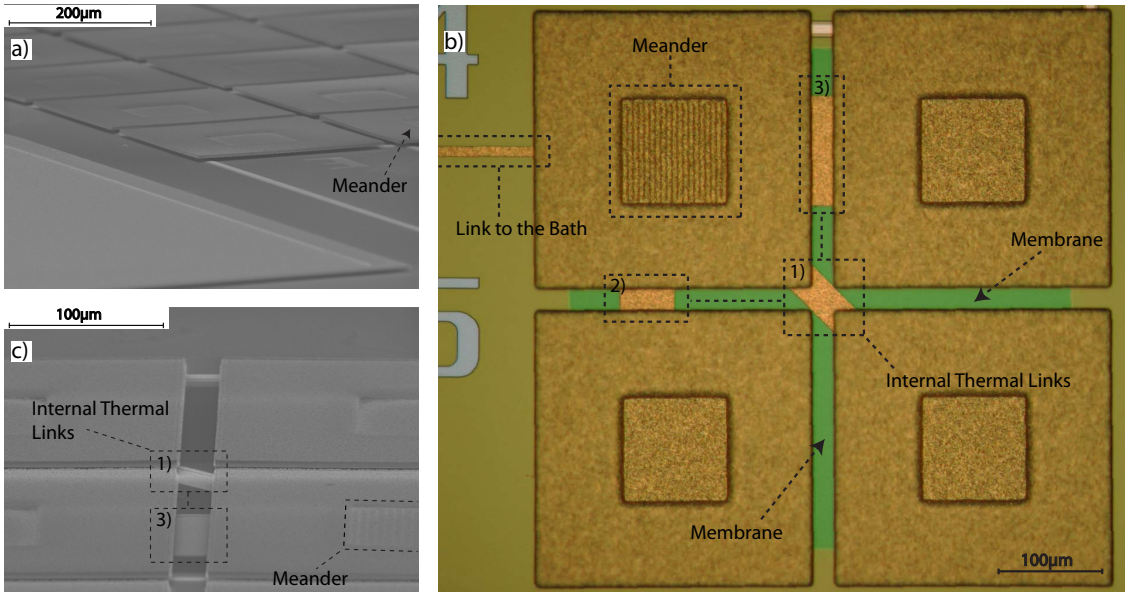

Figure 5.2 **a+c)**: SEM images of Hydra detectors with mushroom shaped overhanging absorbers. **b)** Light microscope picture of a 4 absorber Hydra detector. The numbers (1,2,3) refer to the internal thermal links, also the region of the meander is highlighted in each picture.

[3]Heraeus Holding GmbH, Hanau, Germany.
[4]Oak Ridge National Laboratory, Oak Ridge, TE, USA. Manufacturer information on isotopic composition: ^{168}Er : 97.75%, ^{167}Er : 1.21%, *Rest* : 1.04%.
[5]Techni-Gold RTU 25E, Technic Inc., RI, USA.

A special feature should be mentioned here. The thermal coupling of the individual absorbers to the thermal bath should be kept to a minimal in these devices. The idea is to structure each detector on a thin silicon nitride (SiN) membrane, which has poor thermal conductance to the thermal bath. The membranes are $450 \times 450\,\mu\text{m}^2$ in area and only $0.5\,\mu$m thick. Deep reactive ion etching techniques are used to etch straight from the back of a SiN coated silicon wafer to just leave the SiN membranes.

The absorbers in these devices are overhanging mushroom-like structures made from electroplated gold and bismuth. The cantilevered region underneath the overhanging part of the absorber is highly desirable because it allows for a high filling factor of area coverage, to maintain high collecting efficiency while allowing for wiring underneath the absorbers. To fabricate such a large overhanging absorber structure, a two-step photo-lithographic process has been used similar to the one described in [Bro08]. The stem regions are defined using a positive photoresist mold. A 200 nm gold seed layer is then electron-beam deposited on top of a 20 nm Ti adhesion layer. First a $1\,\mu$m thick Gold film and then a $6\,\mu$m thick bismuth film is then electroplated continuously across the entire area. Subsequent to the deposition of the metal absorber, a second positive photoresist layer is patterned to define the outline of the overhanging absorbers. The exposed metal absorber is mechanically etched using Ar^+ ions. Afterwards the photoresist is removed via oxygen plasma ashing.

5.2 Diffusion welding of rhenium absorbers to the Au:Er sensors

The micro-fabrication of the MMCs has been described in the last section. A further crucial point in measuring the β-spectrum of rhenium with an MMC is to metallically attach a rhenium absorber to the micro fabricated device. This section will focus on this fabrication step that was realized by diffusion welding.

5.2.1 Diffusion in copper-gold

In the past, the diffusion of copper in gold has been studied extensively, see [But74] and references therein. Most experiments were carried out at temperatures above 400 °C and show inter diffusion coefficients of the order of $D \simeq 10^{-8} - 10^{-12}\text{cm}^2/\text{s}$ in a temperature range from 400 °C to 800 °C. These diffusion rates would certainly be enough to achieve metallic contacts between the two metals within a decent time. However, these temperatures are not compatible with the fabrication process, as the Au:Er sensor is already deposited and the alloy should not be heated to temperatures above 250 °C in order to preserve the thermodynamic properties. A few earlier works have measured inter diffusion of copper and gold at lower temperatures [Pin72], even as low as room temperature [Hal77]. These works

agree with low temperature extrapolations of [But74] and diffusion coefficients of $D \simeq 4 \times 10^{-16}\mathrm{cm}^2/\mathrm{s}$ are reported at temperatures around 250 °C. Based on the formula for the diffusion length

$$\ell = \sqrt{2Dt}, \tag{5.1}$$

where t denotes the duration of diffusion. For the given values at 250 °C a diffusion length of $\ell \simeq 12\,\mathrm{nm}$ can be achieved in a duration of $t = 30\,\mathrm{min}$. This should be sufficient to establish an inter-metallic contact given the fact that this length extends over several atomic layers. These promising values for the inter diffusion of copper and gold is the basis for choosing these materials to develop a diffusion welding process, besides the fact that neither gold nor copper are known to degrade detector performance in any respect.

Realization

The starting material of the rhenium absorbers was a commercially available[6] single crystal disk with a diameter of $d = 8\,\mathrm{mm}$ and a thickness of $h = 500\,\mu\mathrm{m}$. It was cut into cuboids of approximately $240\,\mu\mathrm{m} \times 240\,\mu\mathrm{m} \times 500\,\mu\mathrm{m}$ with a wire saw[7].

In the next processing step, one face of the cuboids was cleaned by ion milling. This face was then sputtered with a $0.5\,\mu\mathrm{m}$ thick copper layer and a 10 nm thick gold layer as an oxidation protection layer for the copper.

These rhenium cuboids were diffusion welded to the electro-plated gold stems on the detector chips using the custom-made apparatus shown in figure 5.3.

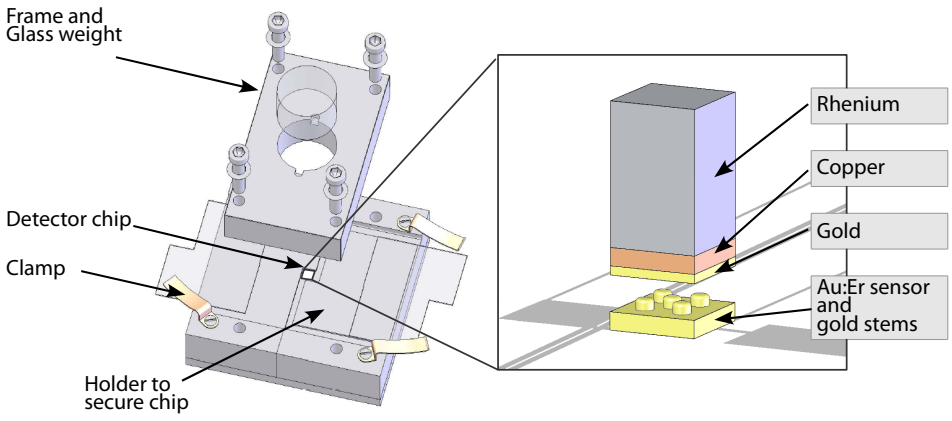

Figure 5.3 **Left:** Schematic of apparatus for diffusion welding. **Right:** Zoom showing details of the layers and detector parts involved.

[6]Goodfellow GmbH, Bad Nauheim, Germany. Purity stated by the manufacturer: 99.999%.
[7]Type WS22, K.D. Unipress, Warsaw, Poland.

In this apparatus a detector chip can be mounted and is held in place by two steel plates. The prepared absorber is positioned on the gold stems with a tweezer laterally held in place by two glass plates. A guiding frame is used to precisely place a glass cylinder on top of the absorber. Additional weights can be placed on top of the glass cylinder to achieve higher pressures. The entire apparatus is placed on a non-vibrating, temperature regulated hot plate.

In tests without heating the samples, it was shown that an applied pressure of $p \approx 10\,\mathrm{kbar}$ (assuming full contact on all stems) was sufficient to indent the gold stems and increase their surface area. The best reproducibility of the welding process could be achieved for welding durations of $t = 30\,\mathrm{min}$ at a temperature of $T = 245\,^{\circ}\mathrm{C}$. Here, more than 50% of the welding attempts were successful.

Figure 5.4 shows a double meander, where a sensor and multiple stems were fabricated on the top of both meanders. A cuboid was welded to the left meander and afterwards removed forcefully. It can clearly be seen, that the welding was successful as parts of the sensor were ripped off the substrate while removing the crystal. The underlying niobium meander stripes can clearly be seen on the transparent sapphire substrate. This demonstrates that the crystal to stem contact is stronger than the sticking of the Au:Er sensor to the substrate. The fact that substantial amounts of the sensor could be found on the surface of the rhenium crystal further supports this interpretation. In comparison, no welding attempt was undertaken for the right meander and all structures are still intact, despite some minor damages from handling.

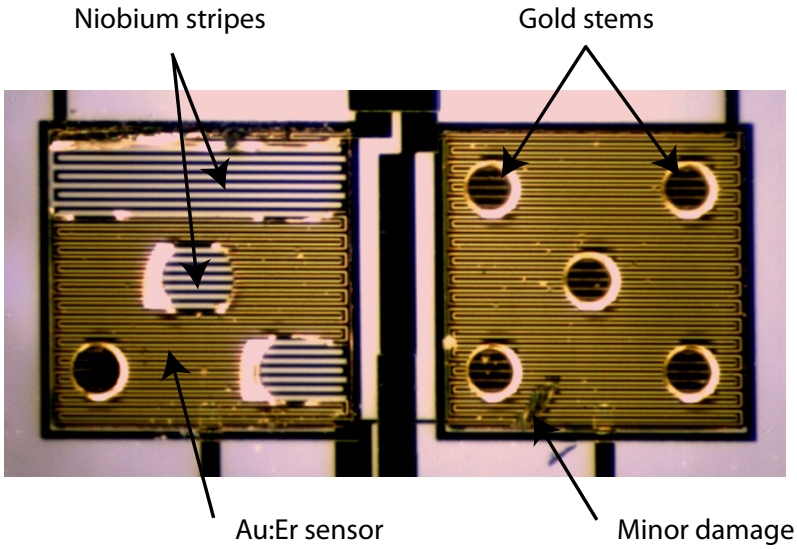

Figure 5.4 Photograph of a double meander. Missing parts of the gold layer prove welding has been successful.

Figure 5.5 shows the magnetization of two Au:Er films as function of inverse temperature from $T = 200\,\mathrm{mK}$ down to $T = 30\,\mathrm{mK}$. Data is shown for two devices that were fabricated on the same wafer. The open circles represent data from a device that did not undergo a diffusion welding process, whereas the crosses represent measured data for an Au:Er sample that has been heated to 245 °C for half an hour. The dashed lines represent the expected magnetization from numerical calculations.

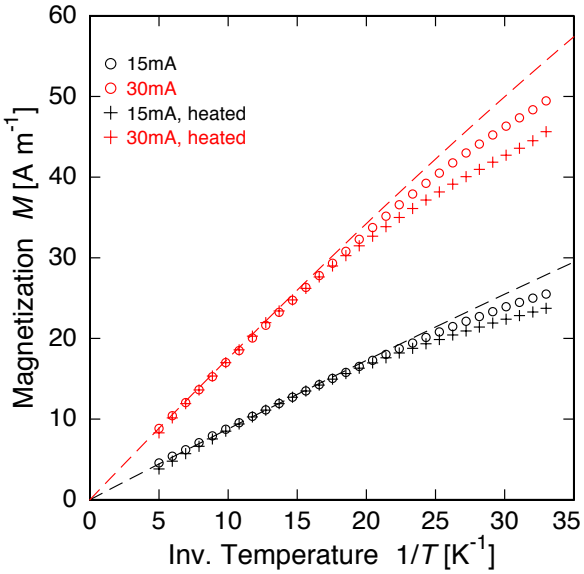

Figure 5.5 Single event in the detector.

This data is taken as proof that the envisaged diffusion welding process will not compromise detector performance. Small deviations towards low temperatures can be explained by differences in the details of the experimental setups. A higher parasitic heating caused by the readout SQUIDs was observed for the samples which were heated before cool down. This is most likely the reason for a stronger decoupling at very low temperatures.

5.3 Detector setup – rhenium experiments

Figure 5.6 shows a sketch of typical detector setup for rhenium experiments. The entire setup is based on a brass holder that is approximately 50 mm long and 20 mm wide. The detector chip as well as the SQUID chip are glued to this brass holder with varnish[8]. A circuit board with copper leads is glued next to the SQUID chip. The connections from the circuit board to the SQUID are realized by ultrasonically wedge bonding aluminum wires. The wire bonds have a diameter of $\mathrm{d} = 25\,\mu\mathrm{m}$. The wiring to the room-temperature electronics is connected using a 12-pin connector.

[8]GE Varnish 7031, Lake Shore Cryotronics, Inc., Westerville, USA.

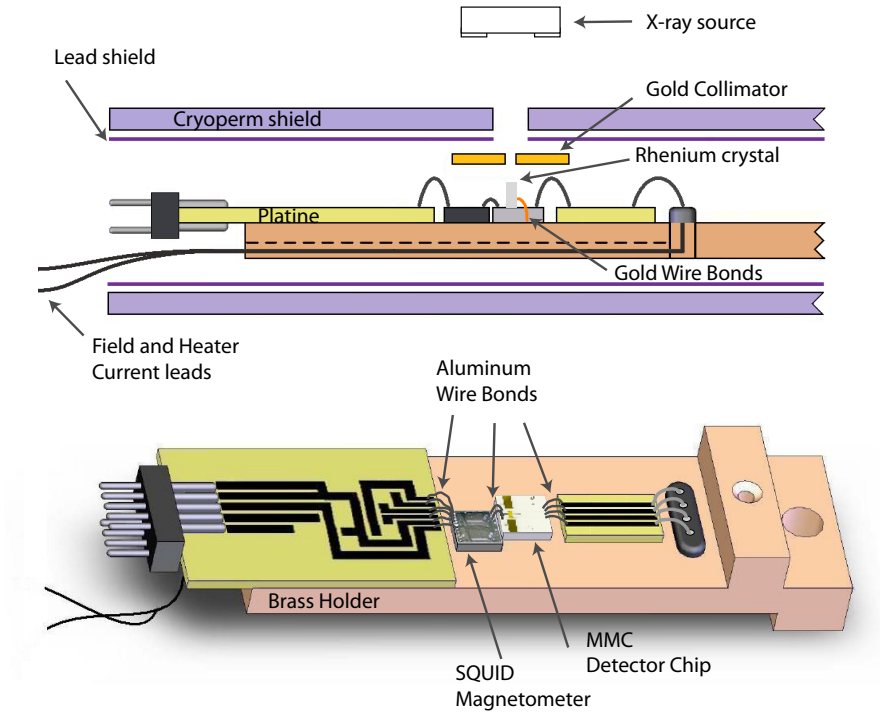

Figure 5.6 Sketch of the detector setup described in detail within the text.

The readout connection from the double meander to the input coil of the SQUID is also realized by aluminum wire bonds, which are kept as short as possible to keep their stray inductance small. Each connection is realized with a pair of wire bonds to further reduce stray inductance. The current leads for the field and the heater current are also connected to the detector chip using aluminum wire bonds.

The leads to supply the field generating current and the persistent current switch heater were achieved in a different way. The currents needed for those parts of the detector are comparably large. To reduce parasitic heating, the connections need to be superconducting. Four NbTi/CuNi[9] wires of 100 μm diameter were guided through a hole in the brass holder and anchored there with adhesive[10]. The wires are filed down parallel to the surface plane of the brass holder to create bond pads for successive wire bonding to the detector chip. The other ends of the wires are soldered to support lines in the cryostat.

Both, the detector and the SQUID chip are thermally anchored to the brass holder in addition to the glue connection. This is achieved by connecting thermalization bond pads on the chips with gold wires of 25 μm diameter directly to the brass holder. The SQUID chip is anchored with approximately 12 wires. The detector chip is anchored with 20 wires from each of the two gold thermalization pads.

[9]The superconducting niobium-titanium filaments are incorporated into a copper-nickel matrix.
[10]A two component epoxy was used: Stycast 2850 FT, by Emerson & Cuming.

To avoid X-ray absorption in the substrate and to collimate X-rays to the absorber area of the detector chip a gold collimator is placed above the detector chip supported by a bridge-like brass piece glued to the brass holder.

The entire brass holder is enclosed by a superconducting lead shield to avoid flux changes at the location of the detector at low temperatures. An additional annealed Cryoperm[11] shield of high permeability can be placed around the entire setup to reduce the absolute value of magnetic stray fields. The entire setup is screwed to the experimental platform of the cryostat.

5.4 X-ray source

To provide X-rays for the characterization of the detectors reported in this thesis, a ^{55}Fe X-ray source was installed in the cryostat. The commercially available source[12] had a nominal activity of $\simeq 18\,\mathrm{MBq}$.

^{55}Fe is an unstable isotope of iron, with a half life of 2.7 y. It decays to $\simeq 88\%$ via electron capture decay of an inner shell (K) electron. The nucleus combines with one of the shell electrons, turning a proton into a neutron and emitting a neutrino. The ^{55}Fe nucleus is transformed to ^{55}Mn and an outer electron fills the vacant state in the K shell, emitting an X-ray photon in the process. The emitted X-rays reflect the fine structure of the manganese atom as the X-ray energy depends on the initial state of the down-converting electron. The lines relevant for the work discussed here are the $\mathrm{Mn}_{\mathrm{K}_\alpha}$ with an energy of $E = 5895\,\mathrm{eV}$ and the $\mathrm{Mn}_{\mathrm{K}_\beta}$ with an energy of $E = 6490\,\mathrm{eV}$, which make up 90% and 10% of the events observed at the detector, respectively [Höl97].

The sources that are installed in the cryostats are stainless steal cylinders of approximately 8 mm diameter and 5 mm height. The active material is glued onto an inset that is then covered by a beryllium window which is brazed to the stainless steal body. The backside of the cylinder is a spring steel lid that is welded to the cylinder.

[11] Vacuumschmelze GmbH & Co. KG, Hanau, Germany.
[12] qsa globel, Braunschweig, Germany.

Chapter 6

Experimental Results

6.1 Implementation of superconductors in MMCs

For a neutrino mass experiment using superconducting rhenium absorbers the thermodynamical properties and thermalization of energy of superconducting absorbers are of vital importance. A brief summary of the results achieved with superconducting absorbers studied in Heidelberg over the last years will be given here.

The corresponding experiments were performed before the development of the optimized detector layout discussed in this thesis and they made use of a dc-SQUID with integrated double meander as described in [Hau06, Por07, Höh08].

As the readily diced chips, carrying Josephson junctions that degrade when heated above 150 °C, were the basis of these early detectors, the options of post-processing the chips to attach absorbers were limited and the different components of the detector (bottom to top), i.e., SQUID chip, Au:Er sensor, gold spacer and rhenium absorber were glued together with different number of glue layers as described below.

In fact the starting point for studying superconducting absorbers in our group was the first detector studying the rhenium β-spectrum [Hau06]. This MMC used a single crystal rhenium absorber that was glued to a 5 μm thick gold foil that served as spacer, which in turn was glued to the Au:Er temperature sensor. The temperature sensor was again glued to the planar meander-shaped pick-up coil. First beta events could be acquired and the superconducting absorber was characterized with an X-ray source. The energy resolution was found to be degraded ($\Delta E_{\mathrm{FWHM}} = 180\,\mathrm{eV}$ at 5.9 keV) compared to a detector that had no rhenium absorber and no spacer, where the X-rays were stopped directly in the Au:Er sensor ($\Delta E_{\mathrm{FWHM}} = 41\,\mathrm{eV}$ @ 3.7 keV).

Furthermore the signal rise of X-ray events stopped in the rhenium crystal was composed of a fast rise of $\simeq 150\,\mu$s to approximately 25% of the maximum amplitude followed by a slower exponential rise with a time constant of $\simeq 1.3$ ms. Also the signal decay was found to be not single exponential as described in [Hau06].

Due to the weak resolving power of the devices used no strong statements on

possible energy loss could be made, but within the errors it was found that no energy was stored longer than on a 10 ms timescale.

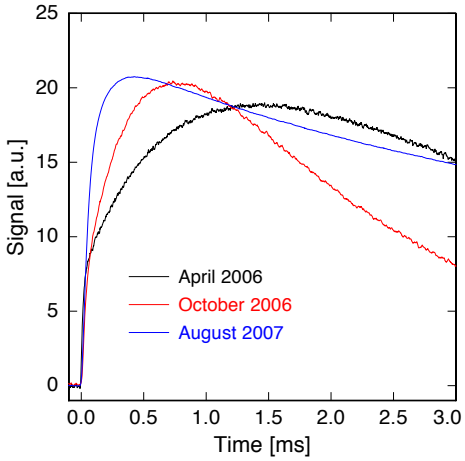

Figure 6.1 Signal rise time of MMCs with rhenium absorber over the past years.

In the following two years more effort was put into fabricating more "hand made" devices. The biggest improvements were made concerning the speed of the signal rise. By reducing the amount of glue between the absorber, spacer and the Au:Er sensor it was possible to accelerate the rise time down to a few hundred microseconds [Por07]. The fraction of deposited energy that is initially stored in athermal systems was found to be approximately one-third, independent of temperature in the investigated temperature range. The second decay time of the observed pulses was roughly an order of magnitude longer than the one of similar MMCs without superconducting absorber and could correspond to the recombination of quasiparticles in the absorber, even if these time constants are several orders of magnitude faster than expected for rhenium single crystals [Por08]. In these experiments the entire energy deposited by the X-ray contributed to the calorimeter signal on time scales shorter than 100 ms. Furthermore, a first analysis of the involved heat capacities was done, showing a heat capacity of the system assigned to the rhenium absorber that was far higher than expected from BCS theory, namely in the order of 3 pJ/K [Por08], but still approximately a factor of 2 smaller than the heat capacities of the Au:Er sensor and the gold spacer ($\simeq 7$ pJ/K). Another way to put this into perspective is comparing the found heat capacity to that of a completely normalconducting piece of rhenium of same volume at a temperature of $T = 60$ mK. In the normalconducting state the absorber would have a heat capacity of $C_{\mathrm{Re}} \simeq 270$ pJ/K which is approximately a factor of 100 larger than the additional contribution observed in this experiment.

In the next iteration a metallic contact between sensor and absorber was achieved by sputter depositing a pure 4 μm thick gold spacer and the 3 μm thick Au:Er sensor directly on the surface of the rhenium absorber [Höh08]. The rise time was found to be well below 100 μs and probably bandwidth limited by the readout chain [Gas09]. Comparing the signal shape observed in the two detector generations the rise time of

the pulses from the phononically coupled absorber of 1 ms was found to be dominated by the weak thermal link between absorber and sensor.

In parallel to the efforts on rhenium as absorber material, aluminum was studied as a superconducting absorber with respect to its thermalization behavior. In setups similar to the one with rhenium, MMCs with aluminum absorber also exhibited very long decay times. Motivated by theoretical work [Kap76, Koz00] on the energy down-conversion in superconductors, where quasiparticles that are energetically relaxed to the upper gap boundary are supposed to have very long life times, yet another absorber system was studied. By doping the superconductor with magnetic impurities the superconductor's gap should be filled with energy levels that might allow for a quicker recombination of quasiparticles and thus lead to a different thermalization behavior. Aluminum doped with manganese was chosen as a candidate and was studied in [Wel08] and [Ran09]. One surprising result was that the signal decay in this alloy did not deviate strongly from the one in pure aluminum, which might find an explanation in the system being a Kondo system and thus showing a strong screening of the magnetic moments possibly suppressing the formation of inter-gap states as intended. As a consequence the current investigation moved on to studying absorbers made of zinc and zinc doped with manganese. This is under current investigation.

6.2 Rhenium detector

In this section measurements with detectors of the developed detector platform are presented. First the characterization of an X-ray detector without rhenium absorber is presented. The resulting magnetization, heat capacity and thermal conductances are discussed first, showing that almost all properties are close to the design values and a good resolving power is proven.

Besides the development of the detector platform for a rhenium based neutrino mass measurement, one central aim of this thesis was the comparison of the detector properties using polycrystalline rhenium and single crystal rhenium as an absorber, respectively. A 30 μm thick polycrystalline rhenium foil was attached metallically to the temperature sensor and in a second detector discussed here a large volume single crystal rhenium cuboid was attached as an absorber. A pulse shape analysis for events in these detectors is presented, which allows to investigate the energy thermalization for events in rhenium. The difference in the detector response is discussed.

6.2.1 Performance of micro-structured detectors

Before discussing the properties of complete detectors including a superconducting rhenium absorber, for which the signal shape is more complex, due to the more complicated down-conversion and thermalization of energy inside the superconductor, we want to present and discuss data on the properties of an identically fabricated MMC without rhenium absorber.

As the MMCs designed for the rhenium experiment posses five gold stems to interface the rhenium absorber but no additional gold layer that could serve as X-ray absorber, we discuss here instead, the properties of an MMC with a $V = 250\,\mu\text{m} \times 250\,\mu\text{m} \times 5\,\mu\text{m}$ X-ray absorber made of electroplated gold. This detector was produced with the same micro-fabrication techniques as the detector chips for experiments with rhenium. The sensor is very similar in height and erbium concentration, just the lateral dimensions of $160\,\mu\text{m} \times 160\,\mu\text{m}$ are significantly smaller than for the rhenium chip. Furthermore, this device is fabricated on a different substrate material, namely thermally oxidized silicon in stead of sapphire. Also the metallic thermalization link forming the thermal conductance from the sensor to the thermal bath is 25% shorter.

Noise and flux coupling

The magnetic flux noise in the primary SQUID of a detector at a temperature of $T = 4.2\,\text{K}$ is very instructive for detector characterization. It can reveal possible failures of the pick-up loop and gives important information on the total inductance of the flux transformer.

Before discussing data, we have look on the equivalent circuit for this measurement that is shown in the right panel of figure 6.2. The circuit consists of two superconducting inductors L_m in parallel representing the meander-shaped pick-up coils, that are connected to the superconducting input coil L_i of a current sensor SQUID via aluminum wire bonds. The transition temperature of aluminum is $T_\text{C} = 1.17\,\text{K}$, whereas the niobium films show a transition temperature of $T_\text{C} \simeq 9\,\text{K}$. Thus, at the measuring temperature of $T = 4.2\,\text{K}$ the wire bonds are the only resistive element in the circuit.
The resistance R_b of the wire bonds causes a current noise in the circuit according to $S_\text{I} = 4k_\text{B}T/R_\text{b}$. Given the sensitivity of the SQUID this current noise is converted to a flux noise that is considerably higher in spectral power density than the intrinsic noise of the SQUID. Furthermore, the circuit acts as a low pass filter with a characteristic cutoff frequency

$$f_0 = \frac{1}{2\pi}\frac{R_\text{b}}{L_\text{tot}}, \tag{6.1}$$

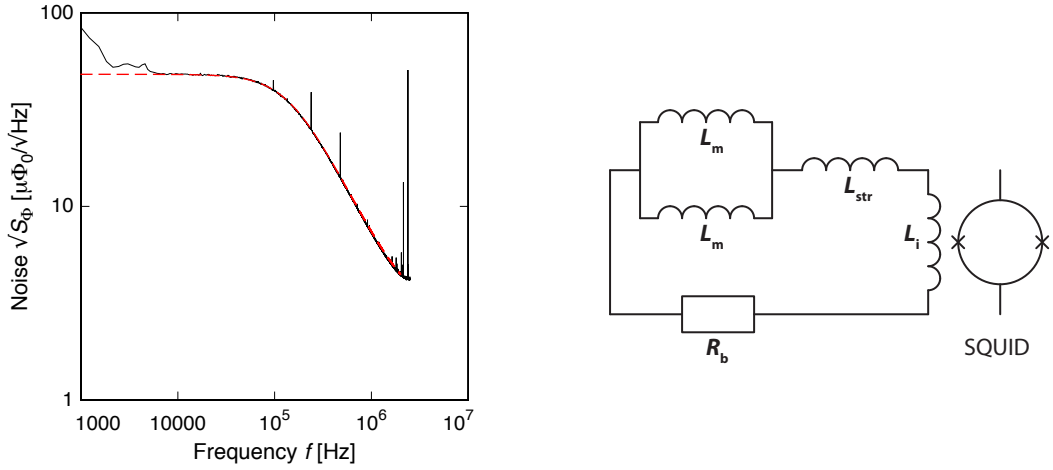

Figure 6.2 **Left:** Measured flux noise in the first-stage SQUID at a temperature of $T = 4.2\,\mathrm{K}$ (solid black line). The dashed red line shows a fit to the functional form of (6.2). **Right:** Sketch of equivalent circuit.

given by the total inductance $L_{\mathrm{tot}} = 1/2L_{\mathrm{m}} + L_{\mathrm{str}} + L_{\mathrm{i}}$ of the circuit and the resistance R_{b} of the aluminum wire bonds. The magnetic flux noise in the SQUID is

$$S_{\Phi}(f) \propto \frac{4k_{\mathrm{B}}T}{R_{\mathrm{b}}} \frac{1}{1 + (f/f_0)^2}, \tag{6.2}$$

where the proportionality factor is given by the input sensitivity of the SQUID used. It is worth to notice that, as discussed in section 2.4.3, this total inductance also forms the denominator in the fraction of flux coupled from the meander to the SQUID

$$\frac{\partial \Phi_{\mathrm{S}}}{\partial \Phi} = \frac{M_{\mathrm{is}}}{L_{\mathrm{m}} + 2(L_{\mathrm{i}} + L_{\mathrm{str}})}. \tag{6.3}$$

Therefore an important factor in the flux coupling of an MMC can be independently derived from the flux noise measurements discussed here.

On the left of figure 6.2 the magnetic flux noise measured in the primary SQUID of the detector discussed in this section is shown. The data measured a liquid helium temperature $T = 4.2\,\mathrm{K}$ is shown as a solid black line. A fit to the function of equation (6.2) is overlaid (dashed red) with fit parameters $R_{\mathrm{b}} = 3.5\,\mathrm{m\Omega}$ and $L_{\mathrm{tot}} = 3.8\,\mathrm{nH}$. The input inductance of the SQUID has been measured independently with the same technique but a resistively shorted input coil and found to be $L_{\mathrm{i}} = 1.8\,\mathrm{nH}$. From other measurements of the setup discussed here the stray inductance is estimated to be smaller than $L_{\mathrm{str}} < 0.5\,\mathrm{nH}$. This leads to a meander inductance of

$$L_{\mathrm{m}} = 2 \times (3.8 - 1.8 - 0.5)\,\mathrm{nH} = 3.0\,\mathrm{nH}. \tag{6.4}$$

Compared to 2D and a 3D finite element simulations this exceeds the expected value by almost a factor of 2. In fact, this measurement meanwhile became a standard

procedure in detector characterization, and the meander inductance was always found to be larger than expected. Usually a discrepancy between 30 % and 60 % was found. The flux coupling deduced from the noise measurements at 4.2 K fit well with for example the magnetization measurements of the Au:Er sensor at millikelvin temperatures for all detectors. The flux coupling deduced from this procedure will be used for the rest of the discussion.

The reason for the increased inductance is not fully understood yet. Generally an additional stray inductance of on-chip wiring, wire bonds or the input coil of the SQUID could cause such a signature, interpreted as increased meander inductance. Even though we have collected a large number of data sets for a variety of chip designs and SQUIDs there is no finite conclusion yet. As the found reduction of flux coupling effects the signal sizes and hence the achievable noise equivalent powers, this phenomenon is under further investigation and designated micro-structures are developed to study potential reasons for the increased inductance.

Magnetization and signal size

The magnetic and thermodynamic properties of the sensor and the absorber form the basis for a good performance of an MMC. Figure 6.3 shows the measured flux in the first-stage SQUID caused by the change in magnetization of the Au:Er sensor as a function of inverse temperature and the pulse height per keV X-ray energy as a function of temperature for three different field generating currents in the meander. The latter were extracted by analysis of the flux signal in the SQUID corresponding to the absorption of 5.9 keV X-rays. For this measurement an external ^{55}Fe source was used.

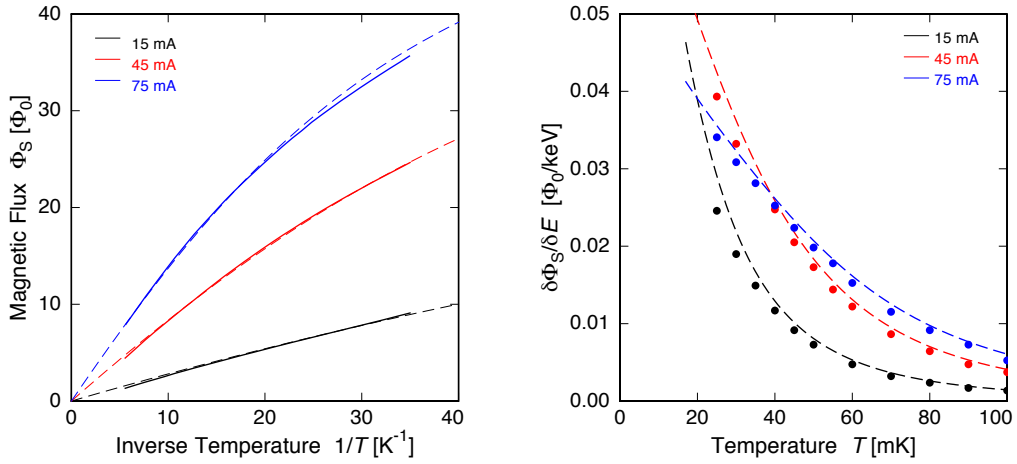

Figure 6.3 **Left:** Magnetic flux measured in the first-stage SQUID versus inverse temperature. **Right:** Pulse height versus temperature . For both plots the dashed lines represent results of the numerical calculations for the three field generating currents denoted.

The dashed lines in figure 6.3 (left) represent the magnetic flux in the SQUID as a function of temperature as calculated from the expected magnetization of Au:Er using an erbium concentration of 315 ppm and a flux coupling as described above. The dashed lines in figure 6.3 (right) represent the expected signal size in the SQUID per unit energy deposited in the absorber combining the expected magnetization of the Au:Er sensor and the expected heat capacity of the Au:Er sensor and the gold absorber.

From the plots it can be appreciated that the experimental results are in very good agreement with theoretical expectations for all persistent currents. In particular this underlines that the magnetization of the Au:Er sensor, the heat capacity of sensor and absorber and the flux coupling from meander to SQUID can be well understood.

Thermal conductance

For a field generating current of $I_\mathrm{f} = 45\,\mathrm{mA}$ the pulse shapes of averaged detector signals upon the absorption of 5.9 keV X-rays were analyzed for various temperatures. The decay time describing the relaxation back to the bath temperature of the pulses were obtained by fitting the signal decay with a single exponential e^{-t/τ_1}. The thermal decay time is given by $\tau = C_\mathrm{tot}/g_\mathrm{b}$, where g_b is expected to depend on temperature as:

$$g_\mathrm{b}(T) = aT + h_\mathrm{k}/AT^3. \tag{6.5}$$

Here the first term represents the thermal conductance through the metallic link. The pre-factor a of the linear part can be calculated from the geometry and the electrical resistivity using the Wiedemann-Franz law

$$g_\mathrm{b} = L\frac{1}{\rho}\frac{hw}{l}, \tag{6.6}$$

here h, w and l are the height, width and length of the link structure, respectively. The second term of (6.5) represents the conductance from the Au:Er sensor to the substrate. It is determined by the thermal boundary resistance between the materials. Theoretically, the pre-factor to the cubic term h_k/A is accessible from acoustic mismatch theory [Swa89].

Figure 6.4 shows the thermal conductance between the Au:Er sensor and the bath as a function of temperature. In the plot the measured data are represented by symbols and a fit to the functional form of equation (6.5) is depicted by the dashed red line.
From the fit the pre-factors are found to be $a = 17\,\mathrm{nW/K^2}$ and $h_\mathrm{k}/A = 630\,\mathrm{W/m^2/K^4}$. These values are in good agreement with expectations. The electrical resistance of the gold layer used as a thermal link was measured at 4.2 K to be $\rho_{4\,\mathrm{K}} = 2.5\times10^{-8}\Omega\mathrm{m}$

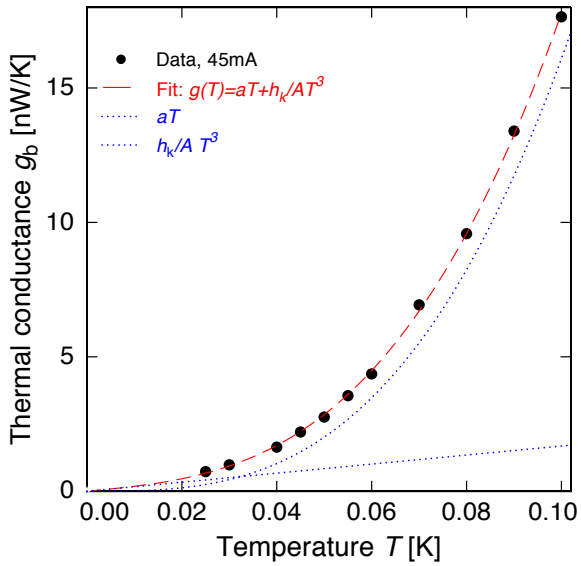

Figure 6.4 Thermal conductance from the senor to the bath as a function of temperature.

and using this value a pre-factor of $a = 18.3\,\mathrm{nW/K^2}$ is expected. In literature a silicon to gold interface is expected to exhibit a thermal boundary conductance according to $h_\mathrm{k}/A = 650\,\mathrm{Wm^2/K^4}$ [Swa89]. Both, the linear and cubic contributions are also shown as dotted blue lines.

X-ray spectrum

For this detector also X-ray spectra of an external ^{55}Fe source were acquired. Figure 6.5 shows a spectrum of the $^{55}\mathrm{Mn}_{\mathrm{K}_\alpha}$ line measured for a field generating current of $I_\mathrm{f} = 32\,\mathrm{mA}$ at a bath temperature of $T = 23\,\mathrm{mK}$. Superimposed to the measured spectrum is the natural lineshape [Höl97] convoluted with a gaussian detector response (solid red line). The contributions of the K_{α_1} and K_{α_2} lines are also depicted. The characterized detector shows an instrumental energy resolution of $\Delta E_\mathrm{FWHM} = 4.0\,\mathrm{eV}$ at $5.9\,\mathrm{keV}$.

It is worthwhile to note that the shown spectrum does not exhibit a significant "tail" towards low energies. This effect has been observed for some devices before and could be eliminated on the level of this energy resolution by reducing the contact area of absorber to sensor. This is achieved by fabricating the electroplated absorbers on 25 stems with $10\,\mu\mathrm{m}$ diameter, reducing the contact area by more than a factor of 10.

In comparison to the MMCs used for rhenium experiments before this marks a large progress, not only is the energy resolution vastly improved, also all accessible micro-fabrication techniques are successfully implemented.

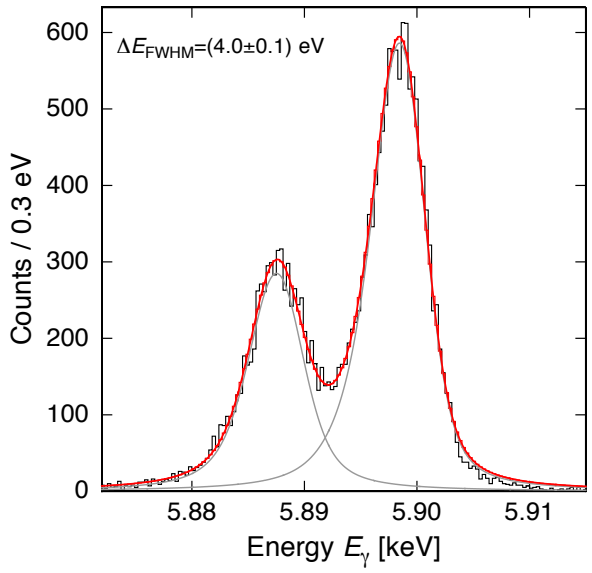

Figure 6.5 Energy spectrum of Mn_{K_α} line. The solid red line represents the convolution of the natural lineshape with a gaussian of width $\Delta E_{\mathrm{FWHM}} = 4.0\,\mathrm{eV}$. The solid grey lines show the contribution of the K_{α_1} and K_{α_2} line, respectively.

6.2.2 Detector with a polycrystalline rhenium foil absorber

Based on the performance of the micro-fabricated device discussed in the previous section, in one of the next development steps a rhenium absorber was attached to the micro-fabricated detector as described in section 5.1. For this a $30\,\mu$m thick polycrystalline rhenium foil was coated with 500 nm of copper and $\simeq 10\,$nm of gold and was diffusion welded to the electroplated gold stems covering the entire sensor area of $A = 245\,\mu\mathrm{m} \times 245\,\mu\mathrm{m}$. The detector was read out by a two-stage SQUID integrated on one chip[1]. The entire experimental setup was shielded with a tempered Cryoperm shield to suppress stray magnetic fields. An additional superconducting lead shield was mounted inside the Cryoperm shield. The experiments were carried out in the adiabatic demagnetization refrigerator in Heidelberg, described in section 3.1.1.

Magnetization

Figure 6.6 shows the measured flux in the first stage SQUID caused by the change in magnetization of the Au:Er sensor as a function of inverse temperature as well as the expected magnetization for this sensor assuming an erbium concentration of $x = 245$ppm. The meander to SQUID loop coupling was assumed as measured via the flux noise at $T = 4.2\,\mathrm{K}$ by the method described in section 6.2. Besides some deviation for temperatures below $T = 50\,\mathrm{mK}$ the measured magnetization shows the expected behavior. The deviation for lower temperatures can be caused by two reasons.

[1] C4X116W, by D. Drung, Physikalisch-Technische Bundesanstalt, Berlin, Germany.

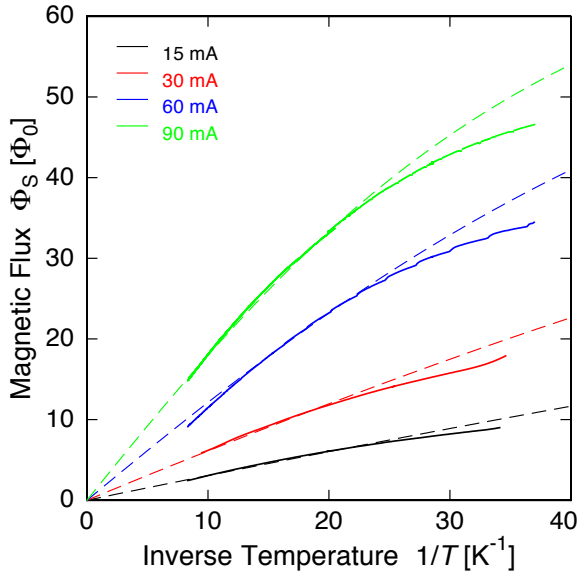

Figure 6.6 Magnetic flux measured in the first stage SQUID as a function of inverse temperature. The solid lines represent measured data, the dashed lines correspond to calculated expectations.

First, the power dissipation on the SQUID chip adjacent to the detector chip leads to parasitic heating of the temperature sensor. This observation has been made in several other experiments and is already suppressed by carefully heat sinking both chips with several gold wire bonds. Nevertheless, a non-negligible effect of the power dissipation on the SQUID chip is observed for this detector. Up to now, the parasitic heating could only be further reduced, in setups where less power was dissipated in the close vicinity of the temperature sensor. This can for example be achieved by using a readout system, where both SQUID stages are located on separate chips. If this is the case the first stage SQUID can be mounted as close as possible to the pick-up coil of the MMC, whereas the second stage can be mounted spatially separated from that.

Second, observing the SQUID signal and the temperature measured by the thermometer on the experimental platform while ramping down in temperature it became obvious that even in phases where the temperature of the experimental platform was stable, the detector was still getting colder. This can be interpreted as a heat load on the detector that fades away slower than the cooling rate of the cryostat. In the discussed setup this behavior must be attributed to the high-permeability Cryoperm shield the detector was located in. However, the overall detector performance will not be highly degraded by the thermal decoupling. Nevertheless, in subsequent experiments, the heat sinking of the Cryoperm shield was further improved and heating effects on the detector were investigated.

Comparing the measured to the calculated data, a sensor temperature can be extracted, this correction will be applied for all further analyses as it is important for extracting and comparing other quantities, e.g. the thermal conductance and the heat capacities, to expected values.

Signal size

The left hand plot of figure 6.7 shows a comparison of the measured signal sizes (symbols) to the expected ones (solid lines) as a function of temperature for four field generating persistent currents. The signal size was determined by extrapolating the exponential decay of the pulse to the time of the first point in the rise. It can clearly be seen that the signal sizes are reduced. For a temperature of $T = 50\,\mathrm{mK}$ the signal size is reduced by approximately 50% and the deviation is somewhat larger for lower temperatures.

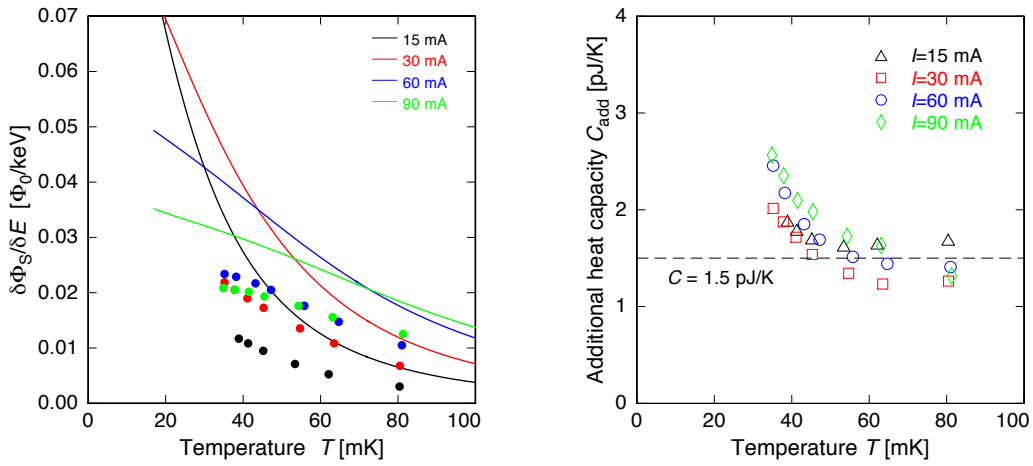

Figure 6.7 **Left:** Measured pulse heights (symbols) in comparison to numerically calculated data (lines) as a function of temperature for four field generating currents. **Right:** Hypothetical additional heat capacity as a function of temperature.

Against the background of previous measurements [Hau06, Por07, Höh08], that were summarized above, the observation of reduced signal heights can be explained by at least two scenarios: (i) The rhenium absorber introduces an additional heat capacity that reduces the maximal temperature rise and thus the signal amplitude. (ii) Not the entire photon energy is thermalized in the sensor within the time scale of the signal rise, similar observations have been made for superconducting absorbers [Cos93].

In the following we want to test, which of those two effects dominated the reduction of the signal size in this experiment by using the following three relations

1. Assuming that all the energy that is deposited in the detector by an energetic particle is down-converted to thermal excitations and bearing in mind the thermal design of the detector, all this heat will eventually flow though the sensor and the thermal link g_b that connects the sensor with the bath. The corresponding temperature pulse $\Delta T(t)$ describes the temperature evolution of the sensor with time. The heat flow $\dot{Q}$ through the thermal link g_b is given by

$\dot{Q} = g_\mathrm{b}\Delta T(t)$ and thus the deposited energy E, the thermal conductance g_b and the integral of the temperature pulse obey the relation

$$E = g_\mathrm{b} \int_0^\infty \Delta T(t)\mathrm{d}t. \tag{6.7}$$

where $\Delta T(t)$ can be determined from the measured pulse in units of flux $\Delta\Phi(t)$ using the slope of the measured magnetization curve at given temperature $\partial\Phi/\partial T$.

2. The discussed signal size $\Delta\Phi_\mathrm{i}$ is given by the initial flux signal upon the absorption of X-rays, extrapolated to the first time in the rise. The flux signal size $\Delta\Phi_\mathrm{i}$ can be converted to a temperature rise ΔT_i using the derivative $\partial\Phi/\partial T$ of the measured magnetization. This initial temperature rise together with the total heat capacity that thermalizes within the rise time can be related to the deposited energy

$$C_\mathrm{tot} = \frac{E}{\Delta T_\mathrm{i}}. \tag{6.8}$$

3. The thermal conductance to the bath g_b, the thermal decay time τ of the pulse (that was fitted with an exponential) and the expected heat capacity C_tot of the Au:Er sensor, the copper layer on the crystal and the gold stems are related by

$$g_\mathrm{b} = \frac{C_\mathrm{tot}}{\tau}. \tag{6.9}$$

As an example we will consider signals recorded with a field generating current of $I_\mathrm{f} = 30\,\mathrm{mA}$ at a corrected temperature of the sensor of $T = 34.5\,\mathrm{mK}$. From (1) the thermal conductance to the bath is found to be $g_\mathrm{b}(34.5\,\mathrm{mK}) = 0.56\Phi\,\mathrm{ms}/5.9\,\mathrm{keV} = 0.76\,\mathrm{nW/K}$. Although this value of g_b is more than a factor of 2 lower than expected from acoustic mismatch theory $g_\mathrm{AMM}(34.5\,\mathrm{mK}) = 1.7\,\mathrm{nW/K}$ given the contact area of the Au:Er sensor to the sapphire substrate, a similarly low value has been observed in a separate experiment.

In this experiment a detector fabricated on the same wafer was studied. The detector had no absorber and a smaller contact area between the Au:Er sensor and the sapphire substrate of $A = 190\,\mu\mathrm{m} \times 190\,\mu\mathrm{m}$ and the detector did not have a metallic link from the sensor to the bath. X-ray signals were recorded at $T = 20\,\mathrm{mK}$ and assuming a known heat capacity of the sensor, the thermal conductance from the sensor to the bath was found to be $g_\mathrm{b}(20\,\mathrm{mK}) = 0.05\,\mathrm{nW/K}$, approximately 30% of the value expected from acoustic mismatch theory.

Scaling the thermal conductance found in the separate experiment by area and cubic in temperature, the contribution of the thermal conductance to the bath

through the substrate for the rhenium detector is expected to be $g_b(34.5\,\mathrm{mK}) = 0.38\,\mathrm{nW/K}$. Additionally, the thermal conductance of the metallic link is expected to be $0.39\,\mathrm{nW/K}$. The total thermal conductance from these considerations is thus expected to be $\simeq 0.77$ with an error of approximately 15%. In other words, the measured thermal conductance from the sensor to the bath is significantly lower than expected from first principles, but considering results of other measurements it shows a good agreement with expectations.

From (2) the total heat capacity is found to be $C_{\mathrm{tot}} = E/\Delta T_{\mathrm{i}} = 5.9\,\mathrm{keV}/0.26\,\mathrm{mK} = 3.7\,\mathrm{pJ/K}$. This heat capacity is more than twice the expected value of $1.7\,\mathrm{pJ/K}$, and an additional heat capacity of $C_{\mathrm{add}} = 2\,\mathrm{pJ/K}$ needs to be introduced at this temperature. The right hand side of figure 6.7 shows the suggested additional heat capacity, derived in this way, as a function of temperature for all measured field generating currents. For temperatures above $T = 50\,\mathrm{mK}$ this heat capacity is found to be around $C_{\mathrm{add}} = 1.5\,\mathrm{pJ/K}$ independent of field current or temperature. Towards lower temperatures the determined additional heat capacity is increasing to maximally $C_{\mathrm{add}} = 2.7\,\mathrm{pJ/K}$ for the highest field current $I_{\mathrm{f}} = 90\,\mathrm{mA}$ at the lowest temperature of $T = 30\,\mathrm{mK}$.

Relation (3) allows to test the findings made from (1) and (2). Inserting the values found above the decay time expected from this is $\tau = (3.7\,\mathrm{pJ/K})/(0.8\,\mathrm{nW/K}) = 4.5\,\mathrm{ms}$. Within the error this indeed is in agreement with the observed thermalization times with the bath, that are shown on the left of figure 6.8.

A more detailed model including diffusion in the sensor and the introduced additional heat capacity C_{add} with a thermal link g_{as} from absorber to the sensor might further improve this agreement. In case that such a model would require to assume

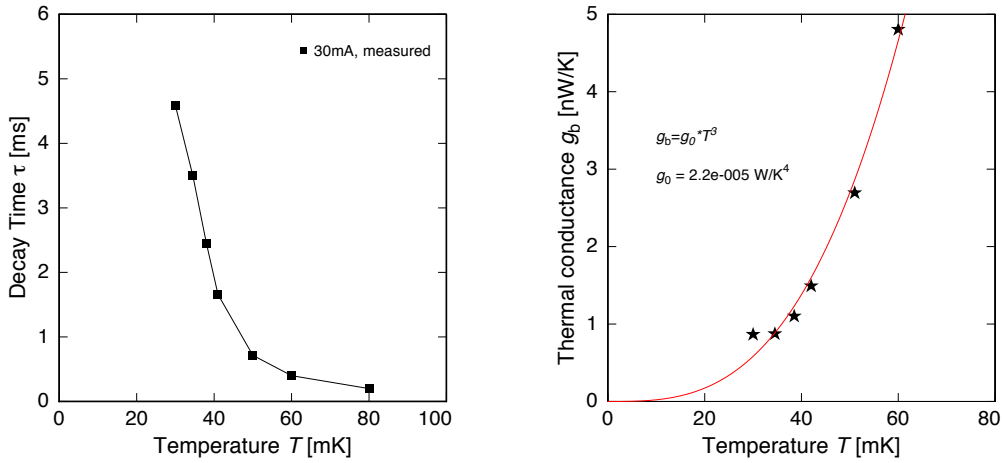

Figure 6.8 **Left:** Measured thermalization time as a function of temperature for a field generating current of $I_{\mathrm{f}} = 30\,\mathrm{mA}$. **Right:** Thermal conductance from the sensor to the bath as a function of temperature determined using equation (6.7).

that only a fraction η of the energy deposited in the absorber leads to a measurable contribution to the temperature pulse. The fraction $(1-\eta)$ of the quasi-lost energy would probably not exceed the $5\% - 10\%$ level.

In conclusion, most of the reduction in signal size $\Delta\Phi$ is caused by an additional heat capacity C_{add}, this finding is further supported by the fact that the relative reduction in signal size is smaller for larger sensor heat capacity, i.e. for higher field generating currents.

It remains the question for the origin of the additional heat capacity. With the discussed data set, this cannot be answered. A possible reason could be a normal conducting region within the rhenium absorber that could for example be caused by magnetic fields. Given rhenium's high Sommerfeld coefficient a volume of $V = (60\,\mu\mathrm{m})^3$ normal conducting rhenium would be sufficient to contribute with a heat capacity of $C_{\mathrm{add}} = 2\,\mathrm{pJ/K}$. For this sample this would correspond to approximately 10% of the rhenium absorber volume.

Signal shape

As discussed before, the rise time will be a crucial parameter to a rhenium experiment. The detector presented here is the first to feature a diffusion welded metallic contact from the rhenium absorber, copper plated on one face, to the paramagnetic temperature sensor. Figure 6.9 shows the detector response focusing on the signal rise.

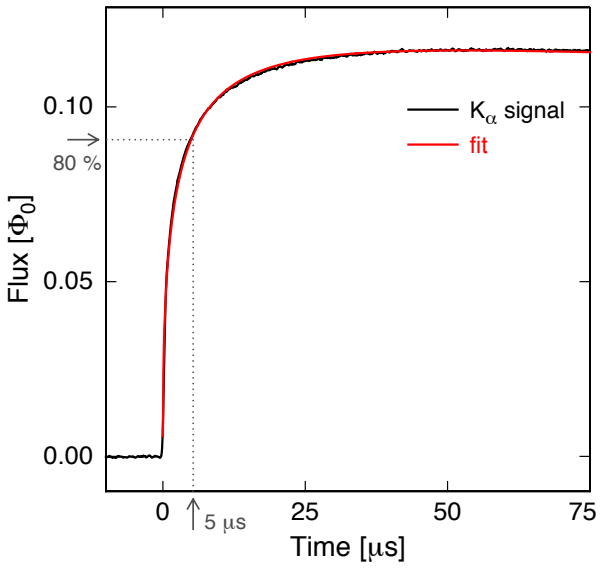

Figure 6.9 Averaged pulse shape in units of magnetic flux in the SQUID upon the absorption of a 5.9 keV X-ray in the rhenium foil. The signals were measured at $T = 30\,\mathrm{mK}$ with a field generating current of $I_{\mathrm{f}} = 30\,\mathrm{mA}$.

80% of the maximum signal height is reached within the first $5\,\mu\mathrm{s}$, the signal rise cannot be described by a single exponential but by a functional form

$$s(t) \propto Ae^{\sqrt{-t/\tau}}. \tag{6.10}$$

The functional form that was found suggests a diffusion like heat transport to the temperature sensor. Considering the polycrystalline nature of the absorber this assumption appears plausible. The rise time observed for this device is not limited by the bandwidth of the readout chain, it reflects the intrinsic thermalization time of absorber and sensor. However, a strong pulse shape variation was found for this device. The variation in pulse shape is illustrated on the left of figure 6.10. Here, three different averaged signals are shown that are all attributed to the absorption of Mn_{K_α} X-rays in the absorber. From the inset it can clearly be seen that a strong pulse shape variation is present in the first 600 μs of the pulse. The main plot suggests that the signal shape converges for $t > 1$ ms.

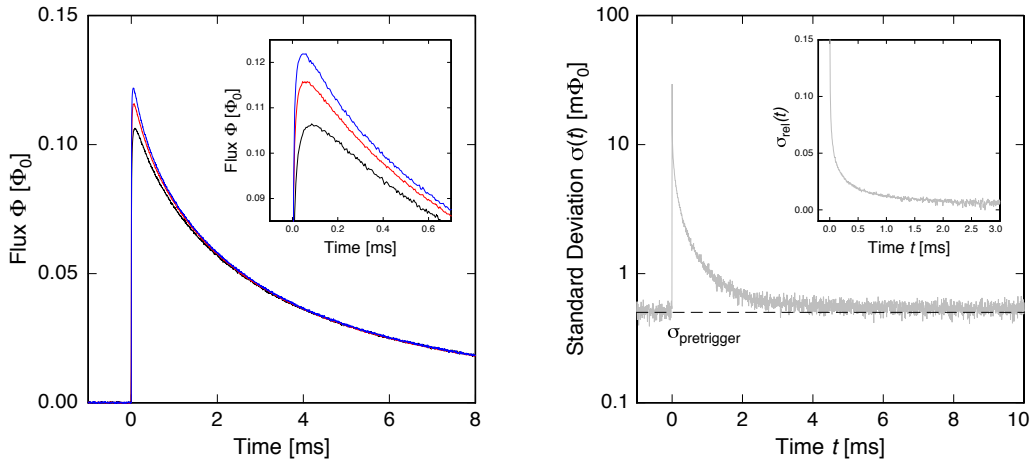

Figure 6.10 **Left:** Varying pulse shapes of signals attributed to the absorption of 5.9 keV photons. **Right:** Standard deviation of signals as a function of time, the inset shows the relative standard deviation as defined in the text.

It is worth to note that the different signals do not cross within the time window of 8 ms. This is expected, as the energy input E is the same for all signals and considering the relation $E = g_\mathrm{b} \int_0^\infty \Delta T(t)$, used before, the integral over time of the different measured signals should yield the same value. Up to a time in the pulse of 20 ms the absolute difference in the value of the integral summed up in the first millisecond of the different pulses appears to remain approximately constant. For longer times this value is impacted by noise. The variation of the integral value is in the range of a few percent. This observation cannot be explained by diffusion, as for such a mechanism the integrals should converge. From this it appears plausible that, at least for the signals smaller in amplitude, a fraction of the energy is stored on long time scales or is lost.

The pulse shape variation was studied by comparing M individual signals $\phi(t)$ to an average signal $\overline{\phi}(t)$ of this set. For this the standard deviation $\sigma(t_i)$ of each

voltage sample i was calculated by

$$\sigma(t_i) = \sqrt{\frac{1}{M}\sum_{j=1}^{M}[\phi(t_i) - \overline{\phi}(t_i)]^2}. \tag{6.11}$$

On the right of figure 6.10 the resulting standard deviation as a function of time is shown logarithmically. The value of the standard deviation before the trigger point $\sigma(t < 0) = 0.5\,\mathrm{m}\Phi_0$ is caused by the random noise of the detector signal without systematic pulse shape variation. The standard variation should be constant in time with this value except for trigger jitter effects, that would cause a short spike, a few samples in length [Fle98]. At the time of the trigger (t=0) a peak can be observed that reaches a maximum of approximately $\sigma_{\max} = 30\,\mathrm{m}\Phi_0$, about 25 % of the absolute signal size. Later in the pulse the standard deviation decays to nearly the pretrigger value. The inset shows the relative standard deviation defined as

$$\sigma_{\mathrm{rel}}(t) = \frac{\sqrt{\sigma^2(t) - \sigma^2_{\mathrm{pretrigger}}(t)}}{\Delta\Phi(t)} \tag{6.12}$$

as a function of time. At the time of the trigger a peak is observed that only slowly decays towards a value of $\sigma_{\mathrm{rel}} = 5 \times 10^{-3}$. The relative standard deviation as defined above can directly be interpreted as a measure for the achievable energy resolution. The standard deviation as determined above will translate into a broadening of the measured linewidth at an energy of 5.9 keV according to $\Delta E_{\mathrm{FWHM}} = 69\,\mathrm{eV}$.

X-ray spectrum

A measured energy spectrum of X-rays of the $^{55}\mathrm{Mn}_{\mathrm{K}_\alpha}$ line stopped in the rhenium foil is shown in figure 6.11. The data was acquired at bath temperature of $T = 35\,\mathrm{mK}$ and with a field generating current of $I_{\mathrm{f}} = 30\,\mathrm{mA}$.

Guided by an analysis of the pulse shape variation as discussed previously, those parts of the pulse that show the lowest relative standard deviation were emphasized. In particular, a weight function for the time domain fit was used that masks the first millisecond of each pulse and emphasizes those parts of the signal, where little pulse shape variation was found.

Obviously, using only fractions of the signals, the full signal-to-(stationary)-noise ratio of the detector cannot be fully exploited. As parts of the signal with large signal amplitude are discarded the signal to noise ratio is strongly reduced. Nevertheless, an energy resolution of $\Delta E_{\mathrm{FWHM}} = 46\,\mathrm{eV}$ could be obtained with this device. Analyzing the so called baseline resolution, signal traces that were not triggered and are attributed to zero energy are analyzed using the same algorithm and set the best achievable energy resolution that is expected with this detector and the chosen data

analysis. The baseline resolution was found to be $\Delta E_{\mathrm{FWHM}} = 36\,\mathrm{eV}$, which cannot fully explain the broadening of $\Delta E_{\mathrm{FWHM}} = 46\,\mathrm{eV}$ found in the energy spectrum. The reason for most of the further broadening can however be found in the pulse shape variation already discussed above. For the spectrum shown, the relative standard deviation for signals in the K_α-line was found to be $\sigma_{\mathrm{rel}} = 1.5 \times 10^{-3}$ leading to an additional broadening of $\Delta E_{\mathrm{FWHM}} = 21\,\mathrm{eV}$. Summing the two discussed contributions in quadrature an energy resolution of $\Delta E_{\mathrm{FWHM}} = \sqrt{(36\,\mathrm{eV})^2 + (21\,\mathrm{eV})^2} = 42\,\mathrm{eV}$ is expected and is in good agreement to the one found.

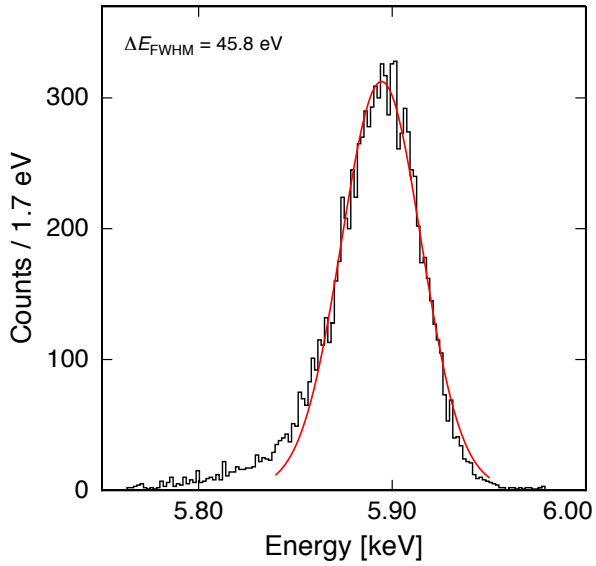

Figure 6.11 Spectrum of $\mathrm{Mn}_{\mathrm{K}_\alpha}$ line complex recorded at $T = 35\,\mathrm{mK}$ with a field generating current of $I_{\mathrm{f}} = 30\,\mathrm{mA}$.

In the spectrum shown in figure 6.11 also a tail on the low energy side of the $\mathrm{Mn}_{\mathrm{K}_\alpha}$ line is observed. Whenever events contribute to this region of the histogram not the full energy could be attributed to the signals. This can potentially be explained by the findings from above, where some signals not only exhibited a slower rise time, but also integrating the pulse over time yielded a smaller value. The nature of this will require further investigation.

In conclusion this detector by far marks the best energy resolution obtained so far using an MMC with a rhenium absorber. The detector performance is limited by the observed pulse shape variation. The observed pulse shape variation can possibly be explained by a diffusive propagation of the heat in the polycrystalline absorber. But in addition to that for slower rise times a potential loss of energy is observed. The overall detector performance is promising and encourages to move on to an MMC with large crystalline absorber.

6.2.3 Detector with a large volume rhenium crystal absorber

In a follow up experiment the comparison of a polycrystalline foil to a large volume singe crystal rhenium absorber was aspired. For this one surface of a single crystal rhenium[2] cuboid, of volume $V \simeq 220\,\mu\text{m} \times 220\,\mu\text{m} \times 500\,\mu\text{m}$ was covered with a $\simeq 500\,\text{nm}$ thick copper layer and a $\simeq 10\,\text{nm}$ thick gold layer. The crystal was diffusion welded to the electroplated gold stems of the micro-fabricated detector chip. This detector was fabricated on a different wafer than the one discussed in the previous section, all dimensions and other fabrication parameters were identical.

The detector was read out by a two-stage SQUID setup. Only the single first-stage SQUID[3] was located adjacent to the detector chip. The entire experimental setup was shielded with a superconducting lead shield. No Cryoperm shield was used in this setup. The experiments were carried out in the dilution refrigerator described in section 3.1.

Magnetization

The flux in the first-stage SQUID caused by the change in magnetization of the Au:Er sensor as a function of temperature was measured for three different field generating currents. The magnetic flux measured in the first stage SQUID as function of inverse temperature is shown in figure 6.12 as solid lines. The expected magnetization signals are shown as dashed lines. The calculated lines are obtained assuming an erbium concentration of 305 ppm in the Au:Er sensor. This value was determined in a separate experiment where the magnetic susceptibility of a sample of the sputter deposited Au:Er film was measured from room temperature to 2 K in a dc-magnetic field of 1T in a commercial magnetometer[4]. The flux coupling from the meander-shaped pick-up coil to the SQUID used for the calculation was determined in a noise measurement at $T = 4.2\,\text{K}$ as discussed in section 6.2.

Deviations from the theoretically expected shape are only observed for temperatures below 35 mK. This behavior can be explained by a marginal thermal decoupling of the sensor from the bath. Similar observations have been made in the past and the most likely source of this thermal decoupling is a parasitic heat input from the readout SQUID. In this experiment, as only the first-stage SQUID was mounted on the same experimental brass holder as the detector chip, the difference between sensor temperature and bath temperature was small.

In conclusion, the magnetic properties of the Au:Er sensor are as expected, which is important, as they form the basis of a well functioning MMC.

[2]Goodfellow GmbH, Bad Nauheim, Germany. Purity stated by the manufacturer: 99.999%.
[3]C4X1, D. Drung, Physikalisch-Technische Bundesanstalt, Berlin, Germany.
[4]MPMS, Quantum Design, San Diego, CA, USA.

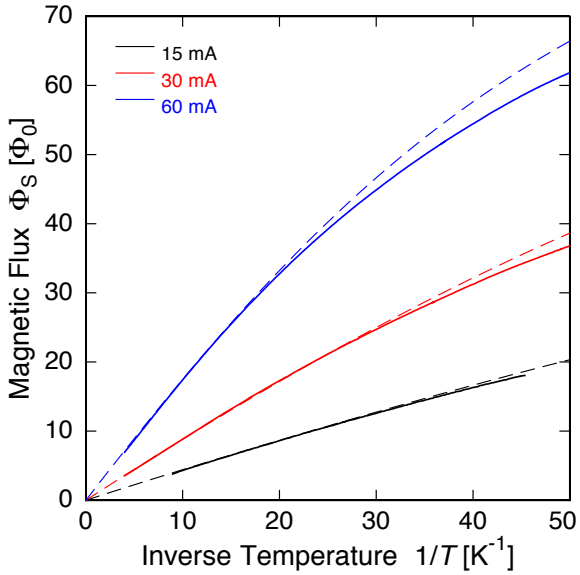

Figure 6.12 Magnetic flux measured in the first-stage SQUID versus inverse temperature. The solid lines represents measured data, dashed lines represent results of numerical calculations.

Signal size

The expected signal size for this detector, in units of flux in the readout SQUID per keV of deposited energy, is shown as a function of temperature on the left of figure 6.13. Depending on the field generating current and temperature a signal height between $0.01\,\Phi_0$/keV and $0.07\,\Phi_0$/keV is expected. The plot on the right of figure 6.13 in contrast shows the measured signal sizes for three different field generating currents as function of temperature. The data was acquired while sweeping the

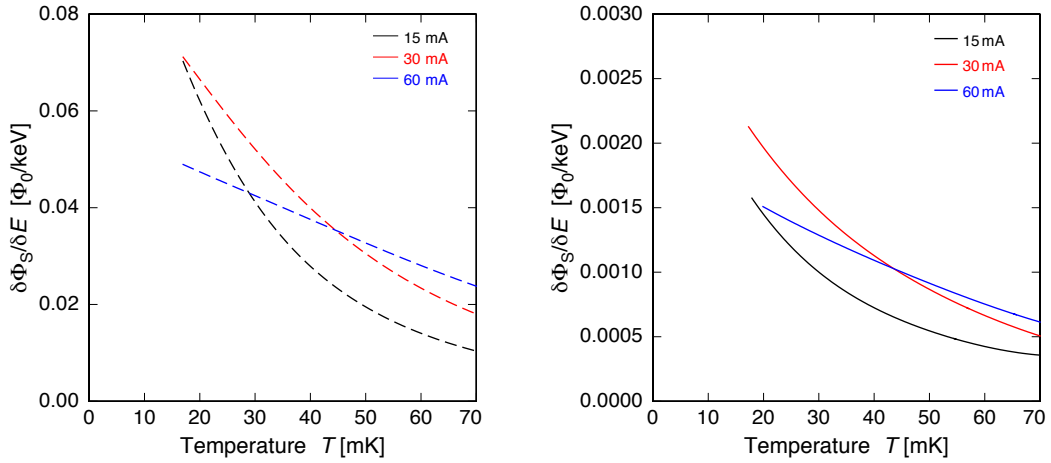

Figure 6.13 **Left:** Expected signal size in the first-stage SQUID per unit of energy input for the detector as a function of temperature for three field generating currents. **Right:** Measured signal size of the detector for the same field generating currents.

cryostat temperature with a rate of approximately $\dot{T} = 1.3\,\mathrm{mK/min}$. The signal size is obtained by determining the maximum pulse height of each event applying a suitable smoothing algorithm.

The measured signal sizes, while showing a qualitative agreement among the three field generating current, is substantially reduced. The signal sizes fall short of achieving the expected ones by a factor of approximately 30. A reduction of signal size of this magnitude has never been observed in rhenium absorbers so far. As the magnetization of the paramagnetic temperature sensor shows the expected behavior, the reason cannot be found in the thermodynamic properties of the sensor. Based on the discussion in the previous section, two possible reasons for the reduced signal size could be considered.

Heat capacity The superconducting rhenium might exhibit an extraordinary large heat capacity that can thermalize with the sensor on a time scale similar to the rise time, and thus the temperature rise of the sensor is reduced accordingly. This reason can be ruled out by pulse shape analysis, in particular by the measured signal decay time, which is determined by the ratio C_{tot}/g. Assuming that the thermal conductance g_{b} from the sensor to the bath is known from the data presented in the previous section, an increased heat capacity would result in an increased signal decay time. As the heat capacity needs to be a factor of 30 higher than expected, to explain the reduction of the pulse height, the signal decay would be elongated by the same factor. This cannot be observed in the data. As can be seen in figure 6.14, besides a long tail with small amplitude, the time it takes the signal amplitude to decrease to $1/e$ times it's maximal value is $\tau \simeq 8\,\mathrm{ms}$. Combined with the estimated thermal conductance from the sensor to the bath at this temperature this does not allows for an additional heat capacity of $C_{\mathrm{add}} > 1\,\mathrm{pJ/K}$.

Furthermore an additional heat capacity of that size would implicate that pulse heights become larger, the larger the sensor heat capacity gets, i.e., the larger the field generating current is. This behavior can clearly not be seen in the data shown in figure 6.13. In the measured data even crossing points between the lines representing the signal size versus temperature data for the different field generating currents are observed. This strongly indicates that the absorber heat capacity is at most of the same order of magnitude as the well understood heat capacity of the Au:Er sensor.

Energy loss A fraction $(1 - \eta)$ of the incoming X-ray energy does not thermalize on the timescale of a complete pulse, i.e., $\approx 100\,\mathrm{ms}$, in the temperature sensor and thus cannot be observed. Assuming that all the energy that is deposited in the detector upon the absorption of a 5.9 keV photon from the calibration source is down-converted to thermal excitations, all this heat will eventually

flow though the sensor and the thermal link g_b that connects the sensor with the bath. Applying equation (6.7) using the slope $\partial\Phi/\partial T$ of the measured magnetization at a given temperature and the thermal conductance to the bath g_b the energy E_d that was detected in the MMC can be calculated. As the device studied here is identical in design and fabrication to the one discussed in the previous section the thermal conductance from the sensor to the bath is used as determined there. The energy that is measured by the detector within the first 40 ms is $E_d = (250 \pm 30)$ eV. This suggests that approximately 95% of the incoming energy cannot be measured by the temperature sensor within a time of 40 ms.

As the additional heat capacity cannot be used as the only reason for the reduced signal sizes, we will now focus on the possible energy loss. The observation, that only a small fraction η of energy can be measured by the temperature sensor again can be interpreted in several ways.

(i) A reason for the observed reduced signal size could be the existence of long living states in the superconducting absorber. A potential mechanism is seen in a system that is able to store energy on time scales as fast as the signal rise but do not release this stored energy on time scales of the signal decay.

(ii) The energy possibly never reaches the sensor, for this the energy would need to be stored in an "energy carrier" that can leave the crystal. This does not seem plausible, as after the absorption the energy will most likely be transferred to first electrons and then phonons. The probability of the electron to leave the rhenium crystal is negligible. Thermal phonons in turn lead to a temperature rise in the detector that will be observable as a signal.

(iii) Potentially a large fraction of energy will be transferred to high energetic ballistic phonons, that can travel from the absorber to the thermal bath without thermalizing in the temperature sensor. As the rhenium absorber is welded on stems the effective contact area between the absorber and the sensor is reduced and therefore the probability for phonons to exit to the thermal bath is reduced as well. Although an effect of that size has never been observed with rhenium absorbers read out by an MMC before, this potential explanation cannot be ruled out at this point.

The effect described in (i) was investigated by focusing on the decay of the signal on long times scales. The signals attributed to the Mn_{K_α} X-rays stopped in the rhenium absorber do not provide a sufficient signal to noise ratio in the experiment discussed here to investigate the potential existence of tails on long time scales. For an analysis of this effect rare arbitrarily large signals, likely caused by the internal bremsstrahlung generated within the X-ray source, were acquired. The maximum time interval that can be used to investigate this effect is the time between two events. For this experiment, due to a high rate of external X-ray events, the investigation was limited to approximately 100 ms. Signals were acquired with 160 ms long time

windows. Figure 6.14 shows a rare high energetic event in the first 100 ms after the absorption.

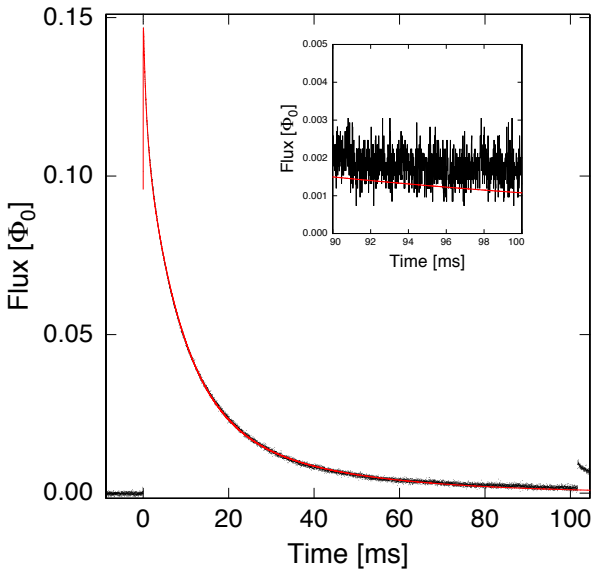

Figure 6.14 Single event recorded in a long time window. The inset illustrates the presence of a long tail.

The signal clearly does not equilibrate back to the pretrigger value within the interval to the next event. The inset of figure 6.14 illustrates that even after 100 ms the temperature sensor still measures an elevated temperature. The solid red line represents a fit to the pulse, where the longest of three decay time constants is found to be $\tau_3 = 30.3\,\mathrm{ms}$. Still, the measured pulse exceeds the value of this fit function at a time of 100 ms.

The observation above can be combined with the determination of the measured energy integrating the pulse over time. As the signal shown in 6.14 appears to be identical in shape to the ones attributed to the 5.9 keV K_α line of ^{55}Mn, an estimate on the necessary lifetime of possible long living states can be given.

The difference in the amplitude of the fitted decay to the amplitude of the signal decay at $t = 100\,\mathrm{ms}$ for the event shown in figure 6.14 is found to be $\Delta\Phi_\mathrm{d} = 7 \times 10^{-4}\Phi_0$. Assuming the fraction $(1-\eta)$ of energy that is not measured within the first 100 ms is only getting to the sensor on long time scales, an area corresponding to the missing energy is expected under the signal on long time scales. An area of $1/(1-\eta) \simeq 20$ times the measured area $\int_0^{100\,\mathrm{ms}} \Delta T(t)\mathrm{d}t$ is expected. A rough estimate for a lower limit of the time needed for this energy to thermalize and traverse the temperature sensor is given by

$$t > \frac{2 \times 20 \times \int_0^{100\,\mathrm{ms}} \Delta T(t)\mathrm{d}t}{\Delta\Phi_\mathrm{d}}. \tag{6.13}$$

For the described pulses this time is found to be as long as $t > 100\,\mathrm{s}$.

Potential mechanisms for these observations are seen in a system that is able to get charged with energy on time scales as fast as the signal rise in the discussed MMCs but do not release this stored energy on time scales of the signal decay. Systems that need to be studied theoretically are e.g. the creation and "storage" of flux vortices in the superconductor and the creation and recombination of quasiparticles. The findings discussed here might encourage theoretical work that exceeds the scope of this work.

The observation that a large fraction of the energy deposited in the rhenium cannot be measured does not agree with what has been observed before as described in section 6.1. As mentioned before the crystals used in early measurements were provided by the group of Prof. Gatti from Genua University. The quality of those crystals was tested in experiments by this group and were found to be suitable for a measurement of the β-spectrum of ^{187}Re[Gat06a]. The crystal used in this detector was produced by cutting a cuboid from a commercially available single crystal According to the specification the purity was as high as 99.999%. Nevertheless, the presence of defects could in principle degrade the thermal properties of the crystal.

As the rhenium crystals are known to be of different origin, studying different material qualities is thus planned for future experiments as well as annealing the rhenium samples after dicing. Studying the difference between a polycrystalline rhenium foil and a large volume single crystal is included in this work.

Although the findings presented here were not expected, the detectors developed for a rhenium experiment already have a great potential now. Especially the achieved fast signal rise is discussed in the following.

Signal Rise

One of the main goals for this detector prototype was to achieve fast signal rise times that are necessary to study the thermalization of energy within the superconductor and, ultimately, to minimize the unresolved pileup of events in a neutrino mass experiment measuring the rhenium β-spectrum. Figure 6.15 shows the measured flux signal in the SQUID upon the absorption of a 5.9 keV X-ray in the rhenium absorber as a function of time. The main figure focuses on the rise of the signal whereas the inset gives an impression of the decay of the pulse. The data was acquired for a field generating current of $I_\mathrm{f} = 30\,\mathrm{mA}$ at the base temperature of the cryostat of $T = 18\,\mathrm{mK}$. The signal rise is very fast reaching 80% of its maximum value after less than $8\,\mu\mathrm{s}$. The signal shape can be described by

$$s(t) = -A_0 e^{\sqrt{-t/\tau_0}} + \sum_i^n A_i e^{-t/\tau_i} \tag{6.14}$$

using a diffusive like summand to describe the rise and at least two exponentials

for the decaying part of the pulse. The time constant for the rise is found to be $\tau_0 \simeq 5\,\mu$s independent of field generating current or temperature. Currently, this represents the fasted signal rise measured with low temperature detectors with a rhenium absorber [Nuc10].

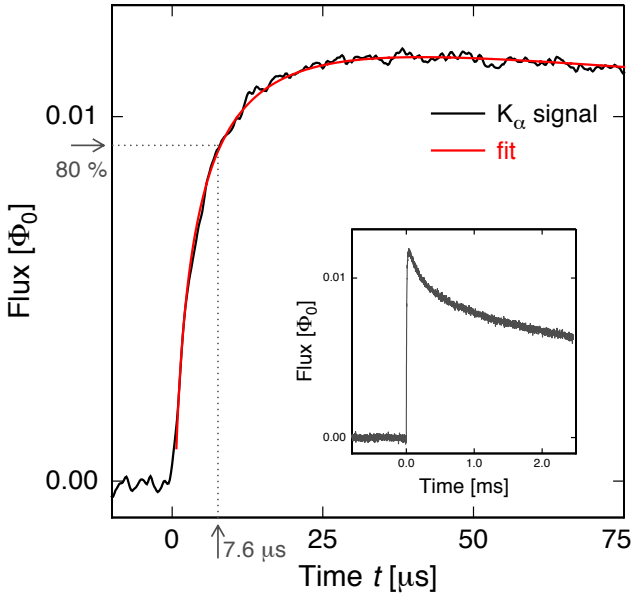

Figure 6.15 Magnetic flux signal in the SQUID upon the absorption of a 5.9 keV photon. The time to reach 80% of the maximum signal size is indicated.

Hidden heat capacity

An additional observation could be made that could not be resolved in earlier measurements with rhenium absorbers. The pulse heights of the signal depend on the temperature at which the field generating persistent current is prepared in the meander. Injecting the current at temperatures above the critical temperature of rhenium $T_c = 1.7\,\mathrm{K}$ results in larger signals compared to the procedure at lower temperatures. Within the error the measured magnetization as a function of temperature is not effected by the different procedures. For a field generating current of $I_f = 30\,\mathrm{mA}$ the difference of pulse height was found to be 35%. Figure 6.16 shows the comparison of signals acquired for both current freezing scenarios at a temperature of $T = 20\,\mathrm{mK}$.

Also in this case the precise cause of the reduction in pulse height is unknown but there is strong indication pointing at an increase of the total heat capacity. In this case not only the pulse height is effected. A clear crossing of the two pulses can be observed implicating that the dominant decay time is increased for the smaller signal. The dominant time constant is found to be increased from 8.5 ms to 11.5 ms also showing an increase of 35%. In conclusion this reduction of pulse height can be attributed to an additional heat capacity. The mechanism that links the preparation of the persistent current at a temperature below T_C of rhenium with the increase in heat capacity is not known but further experiments with different superconducting absorbers will help to better interpret this observation.

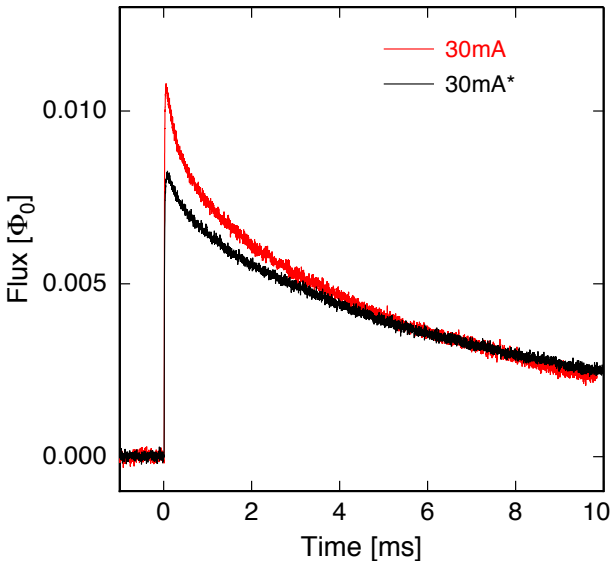

Figure 6.16 Magnetic flux signal in the SQUID upon the absorption of a 5.9 keV photon at $T = 20\,\mathrm{mK}$ for a field generating current of $I_\mathrm{f} = 30\,\mathrm{mA}$ injected at $T > 1.7\,\mathrm{K}$ (red) and $T < 1.7\,\mathrm{K}$ (black).

6.2.4 Conclusion

The primary aim of this work was to provide a reliable MMC suited and optimized for the β-spectroscopy on ^{187}Re. The results presented in the first part of this section demonstrate that micro-fabricated detectors were developed where most design parameters were obtained as expected. For future improvements, the inductive coupling from the meander to the SQUID will be further investigated.

The developed devices were used to investigate two possible species of natural rhenium as absorber materials. First, a polycrystalline foil and second a single crystal cuboid. In both detectors the mechanisms of energy thermalization in superconducting rhenium was affecting the signal shape. Signals upon the absorption of X-rays in the rhenium foil exhibited a pulse shape variation in the first millisecond of the pulse, while in the case of the single crystal a drastic reduction of the detected energy was observed. Likely this latter observation is caused by the material quality as in previous experiments with single crystals of other suppliers an energy loss of that extent was not observed.

A new technique to couple rhenium absorbers mechanically and thermally well to the sensor was developed and successfully tested. With the metallic contact, signal rise times faster than $5\,\mu$s could be observed. According to the characterization of micro-structured devices this rise time is limited by the thermalization of energy in the superconductor. Among low temperature micro-calorimeters, the devices presented in this work exhibit the fastest rise times measured in superconducting absorbers so far. This marks a big step towards an experiment for β-spectroscopy on ^{187}rhenium, as it drastically reduces the effect of unresolved pileup. In addition the detectors developed provide a good basis to study the thermalization of energy in superconducting absorbers.

6.3 Hydra detector

This section is devoted to the characterization of a position sensitive device featuring four absorbers. First, the magnetic properties of the Au:Er sensor are discussed. The pulse shapes resulting from the absorption of X-rays in the different absorbers are presented. Furthermore, the heat capacities of the sensor and the absorbers are discussed and the different implemented thermal links are characterized. A model is presented that allows to predict pulse shapes for detectors with several absorbers. The modeled detector response is compared to measured data in the case of a 4 pixel detector. Finally, high resolution X-ray spectra acquired with the device are presented as well as an outlook on future optimized devices featuring even more absorbers.

6.3.1 Magnetization

Figure 6.17 shows the magnetization of the $100\,\mu\text{m} \times 100\,\mu\text{m} \times 1\,\mu\text{m}$ Au:$\text{Er}_{950\text{ppm}}$ sensor versus inverse temperature measured for a magnetic field generating current of $I_\text{f} = 50\,\text{mA}$. These measured data are represented by a solid line, whereas calculated data for different field generating currents are depicted as dashed lines.

The measured magnetization does not reach the theoretical expectations, it is approximately a factor of 2 lower than calculated. However, the overall behavior for $1/T > 5\ \text{K}^{-1}$ is as expected, with a Curie like trend for high temperatures and slightly saturating behavior for low temperatures. It is evident from the measured magnetization curve that there is an anomalous non-paramagnetic behavior at temperatures greater than 200 mK ($1/T = 5\ \text{K}^{-1}$). A set of additional observations support the interpretation that this behavior can be explained by a superconducting layer in between the meander and the sensor. In fact in one step of the microfabrication process a thin niobium sticking layer is deposited onto the Al_2O_3 insulation layer that covers the meander to enhance the sticking of the succeeding Au:Er sensor. However, in the fabrication run for the device discussed here this sticking layer turned out to be too thick. The design of the device required a niobium film thickness of approximately 5 nm, so that the proximity effect from the Au:Er would keep it normal. In the devices that were tested so far, this niobium layer has been determined to be $20 - 30\,\text{nm}$ thick, and stays superconducting. The magnetic field from the meander, while able to penetrate the thin niobium, is reduced at the Au:Er sensor due to partial screening from the superconducting adhesion layer. This layer affects the size of the magnetic field seen by the erbium spins as well as the size of the coupling between the spins and the meander, both leading to a reduced magnitude of magnetization. Both of these effects also reduce the size of flux change at the meander after an X-ray is absorbed in one of the absorbers.

The same magnetization measurement was carried out for a single pixel device

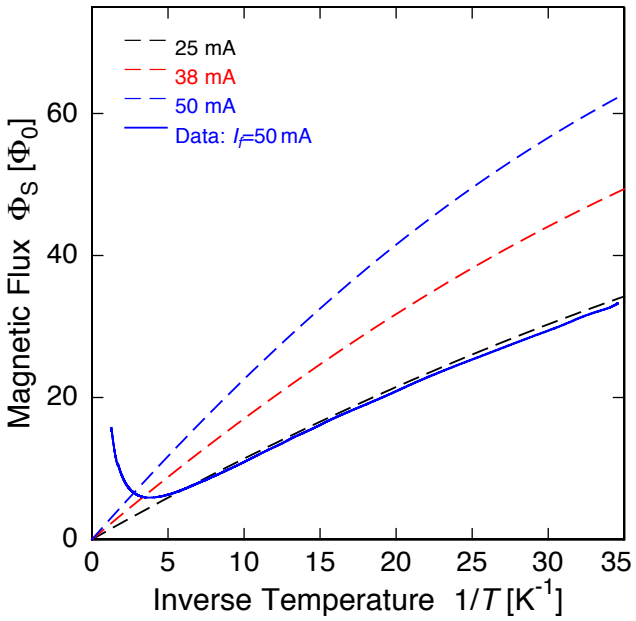

Figure 6.17 Magnetization measured as flux in the SQUID versus inverse temperature. The solid line represents measured data for $I_f = 50\,\mathrm{mA}$, dashed lines represent results of numerical calculations for different currents.

produced on the same wafer for numerous field generating currents, all exhibiting the same behavior. The magnetization is not as large as expected, but the scaling of the magnetization with current is reached with satisfying precision [Ban09].

In a separate experiment the magnetic susceptibility of a sample of the sputter deposited Au:Er film was tested in a dc magnetic field of $B = 0.5\,\mathrm{T}$ from room temperature down to 2 K in a commercial magnetometer[5]. In these data an unusual sharp change in slope of the magnetization curve was observed just below 5 K. The niobium layer was then etched away chemically and the measurement was repeated. After etching, the magnetization was very close to the expected value for an erbium concentration of 950 ppm, and there was no transition near 5 K.

In conclusion the measured magnetization of the Au:Er film does not hold the theoretical expectations. Nevertheless, the magnitude of the magnetization signal is sufficient to achieve excellent detector performance. Furthermore, the reason for the reduced magnetization signal seems to be understood and can be circumvented in future fabrication runs.

6.3.2 Pulse shapes and position discrimination

Figure 6.18 shows the measured change of magnetic flux in the SQUID as a function of time when an X-ray with an energy of $E = 5.9\,\mathrm{keV}$ is absorbed in one of the four absorbers. Each trace represents an averaged signal to reduce noise. The working temperature was $T = 35\,\mathrm{mK}$ and the field generating persistent current $I_f = 50\,\mathrm{mA}$. After the initial absorber-index-dependent equilibration the pulses of all the pixels

[5]MPMS, Quantum Design, San Diego, CA, USA.

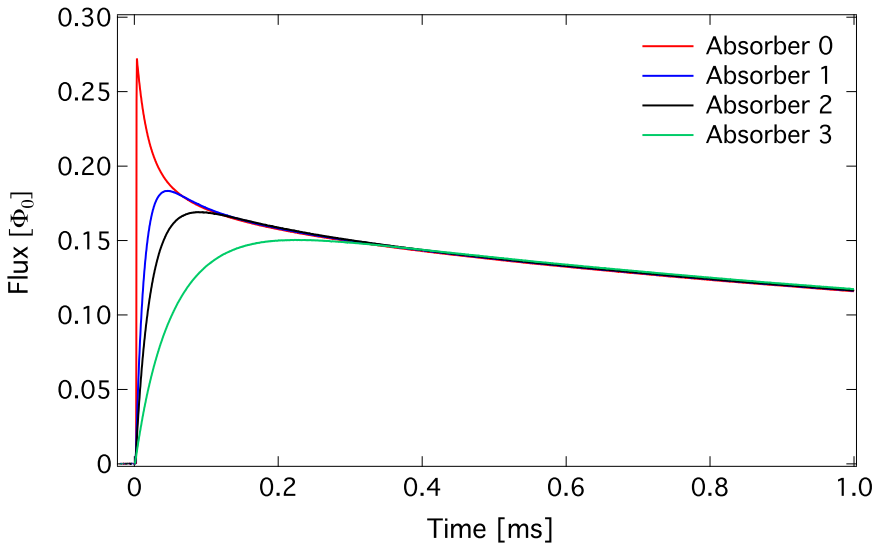

Figure 6.18 Measured averaged pulse shapes for events in the individual pixels of the Hydra detector.

decay with the same exponential decay time, which is determined by the total heat capacity of the sensor and the four absorbers and the thermal conductance between the sensor and the thermal bath. The signal shapes clearly show different rise times which are used for position discrimination. The pulses shown here were acquired without applying a low pass filter to study the unaltered signal rise times, solely limited by the bandwidth of the SQUID readout, which is large enough not to distort the signal shapes discussed here.

Figure 6.19 shows a plot of the rise time versus the pulse height. These data were acquired for the same field generating current of $I_\mathrm{f} = 50\,\mathrm{mA}$ at a temperature of $T = 35\,\mathrm{mK}$ and a low pass filter of 30 kHz was applied in the readout chain. The pulse height was determined prior to optimal filtering from simply the pulse maximum value. The rise time τ_{20-80} is here defined as the time the signal needs to rise from 20 % to 80 % of its maximum value, by a so called 20 % − 80 % boxcar algorithm. It is calculated from the original, unsmoothed data record. The points in the unsmoothed record closest to 20% and 80% of the raw pulse height are found, and interpolation is done to find the 20 % and 80 % points in time t_int^{20} and t_int^{80}, respectively. The rise time is then given as $\tau_{20-80} = (t_\mathrm{int}^{80} - t_\mathrm{int}^{20})/[\log(0.8) - \log(0.2)]$.

The horizontal lines of X-ray events are clearly separated in terms of rise times, varying between 20 μs and 120 μs. For this reason an elongated rise time is determined for the most strongly coupled absorber 0. The events corresponding to the absorption of MnK_α X-rays in all absorbers are labeled on the graph. The low energy continuum can e.g. be attributed to photo-electron loss or background events occurring in the absorber. These events show that position discrimination is possible

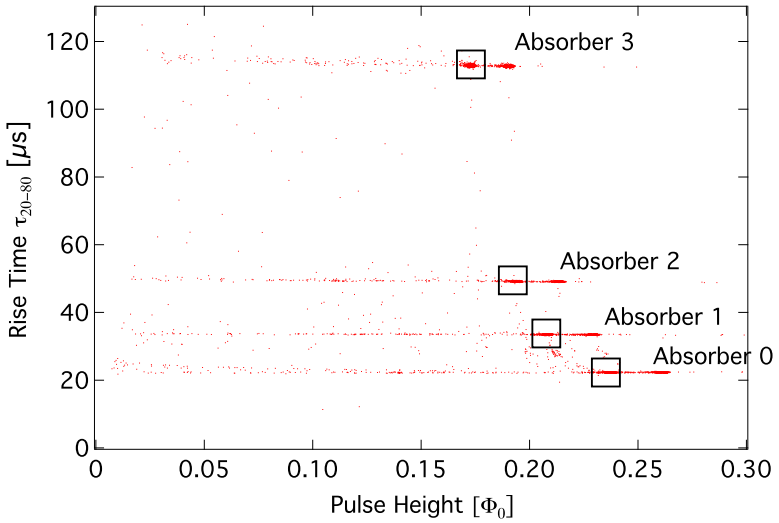

Figure 6.19 Measured rise times (20%-80%) of pulses versus pulse height of the events. Events in the different pixels can clearly be discriminated by their rise time. Points corresponding to MnK_α events are labeled for each absorber.

down to energies of the order of $E < 0.5\,\mathrm{keV}$. More sophisticated algorithms have been developed for micro-calorimeters based on transition edge sensors [Smi09a] and can as well be applied to detectors based on magnetic sensors.

6.3.3 Thermal Properties

After the position discrimination could be shown for X-ray absorption in all four absorbers, a more detailed analysis of the thermal properties of the detector is now given. To gain knowledge of the absolute values of the thermal conductances, the heat capacities involved need to be determined. This is achieved by studying the pulse shapes of X-ray events in the absorber directly above the sensor as a function of temperature.

Heat Capacity

The signal shape corresponding to X-ray events in the absorber right on top of the sensor show a very fast rise time. After reaching its maximum a first exponential decay is observed proceeding into a slower exponential decay. The magnitude of the pulse peak is related to the heat capacity of the sensor plus that of the absorber most strongly coupled to it by

$$\Delta\Phi = \frac{\partial\Phi}{\partial T}\frac{1}{C_\mathrm{s} + C_{\mathrm{a}_0}}\Delta T. \tag{6.15}$$

.

After the initial decay all absorbers and the sensor are in thermal equilibrium. Thus the initial amplitude to the later exponential decay determines the total heat capacity, i.e., the sum of the heat capacity of the sensor and all four absorbers ($C_\mathrm{s}+\sum_i C_{\mathrm{a_i}}$).

To quantitatively extract the heat capacities the pulses, measured as a flux change in the SQUID, are converted to temperature pulses using the derivative $\partial\Phi/\partial T$ of the magnetization versus temperature curve measured for this device. The exponential decays of the initial pulse peak and the later decay are extrapolated back to the time of the first point in the rise to determine all heat capacities.

Figure 6.20 shows the temperature dependence of the derived heat capacities of the sensor plus all four absorber, just the sensor and just one absorber, respectively. A linear fit to the heat capacity of a single absorber is also included in the graph (solid gray line) as well the expected heat capacity (solid blue line) of this sensor with a field generating persistent current of $I_\mathrm{f} = 50\,\mathrm{mA}$. At temperatures above $T = 50\,\mathrm{mK}$ the heat capacity of the absorber on top of the sensor is nearly linear in temperature, as expected for a metal at low temperatures. The derived slope of $8.75\,\mathrm{pJ/K^2}$ represents the electronic contribution to the heat capacity of the absorber. This precise heat capacity measurement can be interpreted as follows considering that the absorber is fabricated as a bilayer of $1\,\mu$m gold and $6\,\mu$m bismuth: Assuming a Sommerfeld coefficient of gold of $\gamma = 0.73\,\mathrm{mJ/K^2/mol}$ [Pob07] the total heat capacity measured would correspond to a $2\,\mu$m thick absorber of given area. Further assuming that the deposited gold will have a heat capacity close to literature value, the $6\,\mu$m thick layer of bismuth would approximately have the same heat capacity as the $1\,\mu$m of gold below. The presented heat capacities are consistent with independent measurements of a single absorber device fabricated on the same wafer [Ban09].

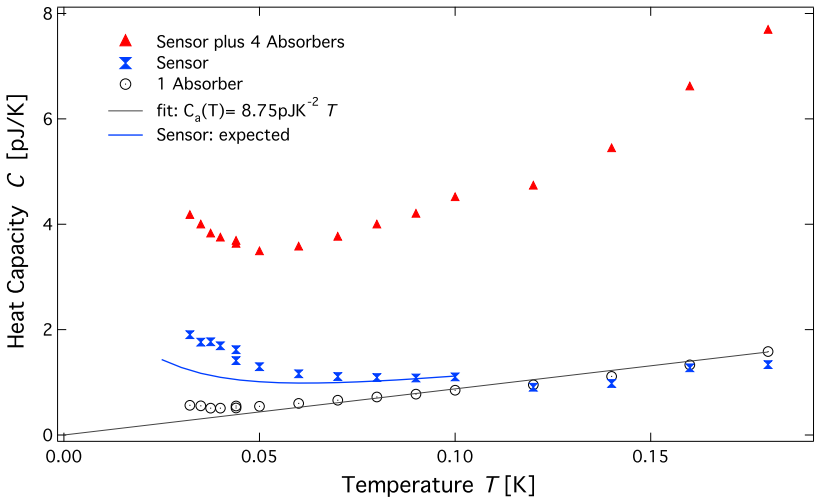

Figure 6.20 Measured heat capacities as a function of temperature. The heat capacities of a single absorber, the sensor plus one absorber, and the sensor plus all four absorbers are shown. The heat capacity of the absorber is fitted linearly as a function of temperature.

The disagreement of the expected to the measured heat capacity of the sensor is not fully understood. Bearing in mind, that the magnetization measurement suggested a lower field generating current, this disagreement would even be larger. For this device no further investigations were made and future detectors with a thiner superconducting film underneath the sensor need to be studied with respect to the disagreement shown here.

Thermal conductances

A crucial part of the detector design are the thermal conductances of both, the internal links between each absorbed and the temperature sensor and the link from the sensor to the thermal bath. It is not only important to achieve the desired ratios of thermal conductances to optimize the desired level of position discrimination, it is equally important to maintain the level of energy resolution. It is to bear in mind that all links were fabricated in the same e-beam evaporated gold layer and the ratio of thermal conductances should be given by the different geometries. Figure 6.21 depicts the measured thermal conductance g_b from the sensor to the heat bath in a temperature range from 32 mK to 180 mK.

The data of the measured thermal conductances were calculated using the measured total heat capacity of the detector consisting of the sensor and the four absorbers as shown in figure 6.20 and an exponential decay time fitted to the slowest decay of the pulses at each temperature. The resulting temperature dependent thermal conductances can be described by a sum of two contributions: one linear and the other cubic in temperature $g_\mathrm{b}(T) = aT + bT^3$. Both contributions are illustrated by the two grey lines in the graph. The coefficients are found to be $a = 32.1\,\mathrm{nW/K^2}$ and $b = 1078\,\mathrm{nW/K^4}$, respectively.

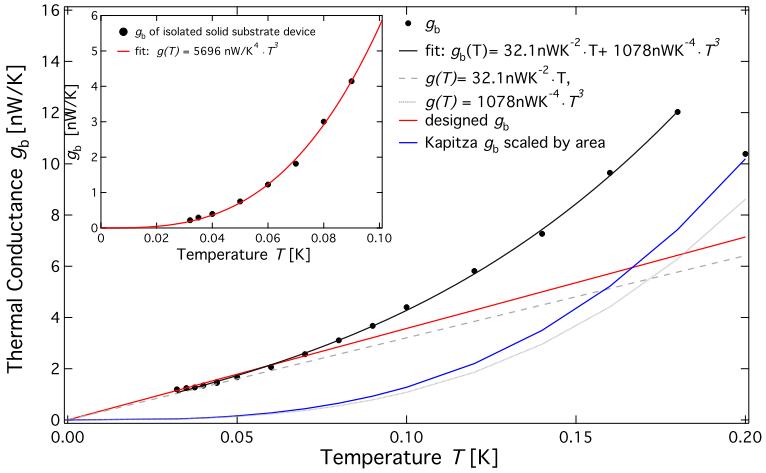

Figure 6.21 Thermal conductance g_b to the bath versus temperature. The inset shows data of a MMC on solid substrate without a metallic heat link to the bath.

The measured pre-factor a of the linear part of the thermal conductance g_b for the metallic heat link can be compared to the expected one, which can be calculated from the geometry and the measured electrical resistivity of the e-beam evaporated gold layer using the Wiedemann-Franz law to be

$$g_\mathrm{b} = L\frac{1}{\rho}\frac{h_\mathrm{Au}}{n_\square}, \tag{6.16}$$

where $L = 2.4 \times 10^{-8}\,\mathrm{W\Omega/K^2}$ is the Lorenz number, ρ is the specific resistivity of gold at the given temperature, h_Au is the thickness of the thermalization link and $n_\square$ specifies the length of the thermal link given in number of micro-structured squares. For the given geometry of 35 squares, a gold thickness of $0.25\,\mu$m and a residual resistivity ratio of 5 for the evaporated gold film, the slope of the thermal conductivity versus temperature is $a = 35.7\,\mathrm{nW/K^2}$. This is approximately 10% larger than the linear term derived from the data above. The calculated thermal conductance is plotted as a solid red line and agrees well with the linear part of the fit (dashed gray line). The observed deviation from the design value can be explained by equally large uncertainties in one of the fabrication parameters, like for example the gold thickness or the residual resistivity ratio.

From basic assumptions the linear term of the thermal conductance is defined by the electronic thermal conductance of the metallic gold link. By design this link should dominate the thermal conductance throughout the temperature range. As the device is fabricated on a thin membrane only a negligible thermal conductance to the bath is expected to be contributed by phononic transport.

Nevertheless, a significant additional contribution to the thermal conductance between the sensor and the bath with cubic temperature dependence is observed. This additional thermal conductance can be interpreted in two ways. The first is motivated by the data shown in the inset of figure 6.21. Here the thermal conductance to the bath is shown as a function of temperature, measured for a single pixel magnetic calorimeter. The sensor of this device was deposited onto a solid substrate and no metallic heat link to the bath was present. The thermal conductance g_b of this device follows a cubic temperature dependence with good agreement to theoretical values for the thermal boundary resistance from acoustic mismatch theory. The measured value of $g_\mathrm{b}/(A \times T^3) = 0.057\,\mathrm{W/cm^2/K^4}$, where A is the area of contact, is in between the calculated values for a silicon to gold interface ($0.063\,\mathrm{W/cm^2/K^4}$) and for an aluminum oxide to gold interface ($0.053\,\mathrm{W/cm^2/K^4}$) [Swa89].

In the case of the position sensitive detector, the sensor itself is structured on a membrane but the metallic thermal link to the heat bath passes over solid substrate for most of its length. The contact area of the thermal link to the solid substrate is approximately 20% compared to the one of the solid substrate device. Scaling the value found for the solid substrate device with the solid substrate contact area of

the thermal link leads to the solid blue line shown in figure 6.21 and shows close agreement with the conductance measured.

Another explanation for the additional thermal conductance cubic in temperature could be given by an extra conductance through the membrane that is limited by a Kapitza resistance from the sensor to the membrane. This boundary resistance would need to be a factor of 5 lower than the boundary resistance to a solid substrate. A limited set of data on such a device does support these findings. This latter explanation is further supported by the observation that the rise times of pulses appear to be faster than expected for events occurring in the three weakly coupled absorbers.

6.3.4 Noise

Figure 6.22 shows a spectrum of the measured flux noise in the SQUID at a temperature of $T = 36\,\mathrm{mK}$. A low pass filter of 15 kHz was applied while acquiring the data. The calibration source was removed for this measurement. X-rays did not illuminate the detector.

At frequencies up to 100 Hz the noise contribution given by thermodynamic fluctuations can clearly be observed above the $1/f$-type noise contributions of the SQUID and the erbium ions. The data can be understood theoretically with the model introduced in section 6.3.6. The sum in quadrature of the noise contributions considered in the model is overlaid as dashed blue line. The individual contributions to the modeled noise are also shown as dashed lines. The thermodynamic fluctuations of energy are depicted as dashed grey line and are calculated based on the measured heat capacity and thermal conductances.

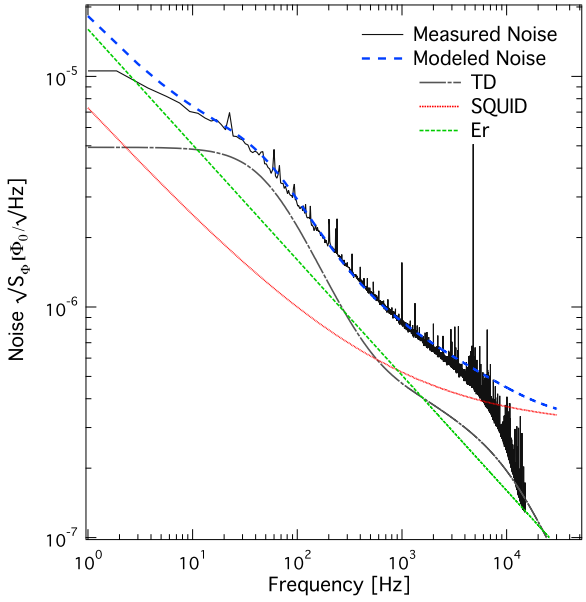

Figure 6.22 Measured flux in the SQUID of a 4 absorber Hydra (solid black line). The dashed red line shows a modeled noise spectrum for parameters given in the text.

The contribution attributed to the erbium ions is shown as dashed green line and according to the concentration and the coupling scheme the amplitude at $f = 1\,\mathrm{Hz}$ of $17\,\mu\Phi_0/\sqrt{\mathrm{Hz}}$ is realistic. The flux noise of the SQUID is shown as dashed red line. Here, the white noise level of the SQUID was set to $0.3\,\mu\Phi_0/\sqrt{\mathrm{Hz}}$, and the amplitude of the $1/f$-type noise of the SQUID was varied freely and was set to be $7\ \mu\Phi_0/\sqrt{\mathrm{Hz}}$ at a frequency of 1 Hz, both are reasonable values for the used type of SQUID operated at millikelvin temperatures.

6.3.5 Spectra

Besides the thorough characterization of the thermodynamic properties of all detector components, also high resolution X-ray spectra were acquired. All four absorbers of the detector were simultaneously irradiated with a moderate rate. Figure 6.23 shows the measured spectra of the MnK_α line for all four pixels of the device. The superimposed smooth curve represents the natural lineshape [Höl97] convoluted with a Gaussian representing the lineshape of each detector pixel with a full width at half maximum linewidth as noted on the right of each spectrum. The detector was operated with an applied field generating persistent current of $I_\mathrm{f} = 50\,\mathrm{mA}$ at a bath temperature of $T = 32\,\mathrm{mK}$. The spectrum for each absorber consists of approximately 2500 single photon events. The data have been analyzed applying gain drifts and individual optimal filter algorithms for each pixel separately.

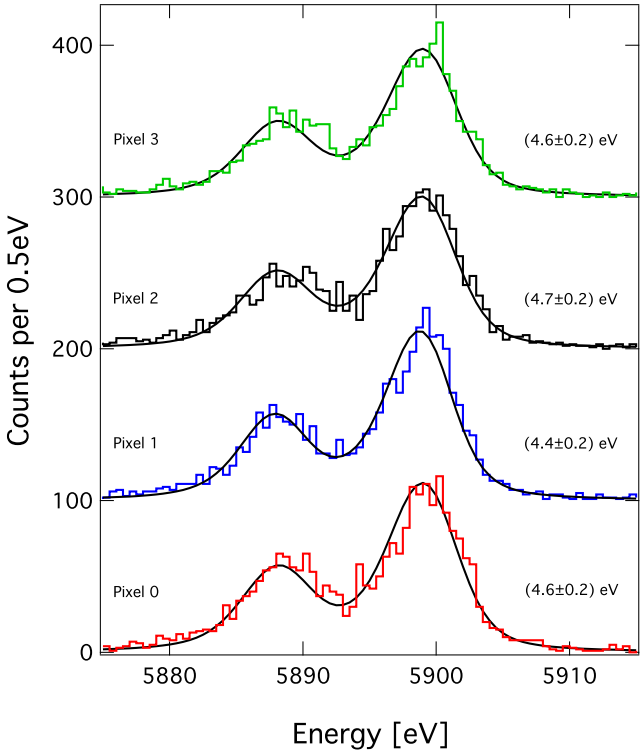

Figure 6.23 Spectra of the MnK_α lines measured with a Hydra detector operated at 32 mK. The spectra from the individual absorbers are vertically offset by 100 counts/bin. The applied field was generated using a persistent current of 50 mA. No data cuts other than pileup rejection was performed, a gain drift as well as individual optimal filters were applied.

The spectra for all four absorbers show an energy resolution lower than $\Delta E_{\mathrm{FWHM}} = 5\,\mathrm{eV}$. The integrated noise equivalent power (NEP) as derived from measured noise without X-ray illumination and the measured pulse shape of 5.9 keV X-rays of the pixels were 2.2 eV, 2.4 eV, 2.5 eV and 2.8 eV for absorber 0,1,2 and 3 respectively.

An especially large broadening in the energy resolution compared to the achieved NEP was observed for pixel 0, where the absorber is most strongly coupled to the magnetic sensor. It is most probably caused by position sensitivity within the absorber. The energy deposited in an absorber must come into thermal equilibrium on a time scale that is faster than the time scale with which it thermalizes with the other absorbers. Otherwise, heat that leaves the absorber before it has fully equilibrated leads to position dependence and can be observed as pulse shape variation. This pulse shape variation should be kept approximately as small as the desired resolving power of the detector in order to not compromise spectral resolution.

As a consequence of this finding, for absorber 0 a bandwidth limit of 500 Hz was successfully applied to the digital optimal filter. In doing so the usable bandwidth is reduced and the baseline resolution is degraded, but the instrumental energy resolution of this pixel is improved, by suppressing high frequency components in the signal and the impact of the pulse shape variation can be reduced significantly.

The same effect has been observed for position-sensitive detectors using transition edge sensors as thermometer [Smi09b].

Absorber 1 to 3 do not show such a large broadening compared to the determined NEP. As their thermal coupling to the temperature sensor is progressively reduced the internal links naturally act as a thermal low pass filter and the position sensitive signal components are suppressed. The degree of position dependence within an absorber generally depends upon the ratio of the thermal conductance between the absorber and the sensor and some effective conductance within the absorber.

The energy resolution achieved so far is very encouraging, even if there is some degradation compared to what is expected from the measured noise equivalent power. A similar degradation in energy resolution was also seen in single absorber devices [Ban09] and is thought to be mainly due to instabilities that require further investigation. Furthermore, as discussed in section 6.3.1 further improvement of both the NEP and the line width measured with the devices are foreseen solely by eliminating the superconducting film below the Au:Er temperature sensor and thus increasing the signal sizes. Nevertheless, it is worthwhile to mention that this detector currently is the highest resolving position sensitive micro-calorimeter at these energies. A sub 5 eV energy resolution was demonstrated over all 4 pixels, approximately 1 eV lower than for a comparable device based on transition edge sensor technology [Smi09b].

6.3.6 Modeling position sensitive detectors

In this section the detector response as well as the expected noise are modeled. The results are compared to the acquired data presented above for the Hydra detector with four absorbers. Finally, a future detector featuring nine absorbers is proposed.

A sketch of the thermal subsystems of a magnetic calorimeter with pixellated absorber is depicted in figure 6.24. Here, n absorbers (0 through n-1) are thermally in contact with one temperature sensor through different thermal conductances $g_0 \dots g_{n-1}$, the temperature sensor in turn is coupled to a thermal bath via the significantly smaller thermal conductance g_b. For each heat capacity in this device, namely the absorbers and the paramagnetic sensor, the temperature evolution with time can be calculated following a set of linear differential equation.

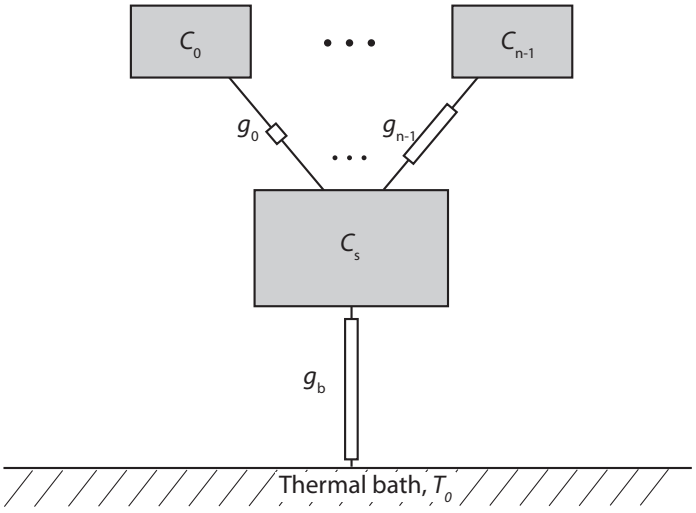

Figure 6.24 Sketch of the thermal subsystems of a Hydra with n absorbers.

Detector response

The detector response following the absorption of an energetic particle in one of the absorbers is determined solving the differential equation including all heat capacities and thermal conductances. The temperature evolution of the absorbers can be formulated as follows:

$$\dot{T}_{\mathrm{a}_i} = -\frac{T_{\mathrm{a}_i} - T_\mathrm{s}}{C_{\mathrm{a}_i}/g_i} + \frac{\dot{Q}_i}{C_{\mathrm{a}_i}}, \tag{6.17}$$

where T_{a_i} denotes the temperature of absorber i, C_{a_i} is the heat capacity of absorber i and g_i is the thermal conductance from absorber i to the sensor. $\dot{Q}_i$ is an additional heat input in absorber i for example originating from the absorption of an energetic particle. An additional thermal conductance to the bath e.g. for each absorber to

the substrate can easily be incorporated in the model if necessary, but is not included at present.

The situation for the temperature sensor is slightly more complex as it is in thermal contact to all four absorbers and the thermal bath. The overall formalism stays the same and the temperature evolution of the sensor is

$$\dot{T}_{\mathrm{s}} = \frac{T_{\mathrm{a}_0} - T_{\mathrm{s}}}{C_{\mathrm{s}}/g_0} + \ldots + \frac{T_{\mathrm{n}-1} - T_{\mathrm{s}}}{C_{\mathrm{s}}/g_{\mathrm{n}-1}} + \frac{T_0 - T_{\mathrm{s}}}{C_{\mathrm{s}}/g_b}, \tag{6.18}$$

here the heat input term is omitted, as energy absorption should only take place in the absorbers. To numerically calculate the temperature evolution of the sensor and all four absorbers with time a more compact notation with a matrix formulation for the set of equations discussed was used. This formalism is used for numerical evaluation with MATLAB[6] and Mathematica[7].

Introducing a temperature vector

$$\mathbf{T} = \begin{pmatrix} T_{\mathrm{s}} \\ T_{\mathrm{a}_0} \\ \vdots \\ T_{\mathrm{n}-1} \end{pmatrix} \tag{6.19}$$

with entries for the temperatures of the sensor and all absorbers, the evolution in time can be formulated as

$$\frac{\partial}{\partial t}\mathbf{T} = \mathbf{D}\mathbf{T} + \mathbf{Q}\mathbf{s}. \tag{6.20}$$

For simplicity the temperature differences $T - T_0$ between the individual systems and the bath will be treated as the absolute temperatures $T \mathrel{\widehat{=}} T - T_0$. The product **Qs** defines the power input given by the energy E of incoming particles. The matrix **D** contains all heat capacities and thermal conductances ruling the dynamics of the system. For the present case they are as follows:

$$\mathbf{Q} = \begin{pmatrix} \frac{1}{C_{\mathrm{s}}} & 0 & \cdots & 0 \\ 0 & \frac{1}{C_{\mathrm{a}_0}} & 0 & 0 \\ \vdots & 0 & \ddots & 0 \\ 0 & 0 & 0 & \frac{1}{C_{\mathrm{a}_{n-1}}} \end{pmatrix}; \qquad \mathbf{s} = \begin{pmatrix} 0 \\ E\,\delta(t - t_0) \\ \vdots \\ E\,\delta(t - t_0) \end{pmatrix} \tag{6.21}$$

[6]MATLAB by MathWorks, Ismaning, Germany.
[7]Wolfram Research, Inc. Champaign, IL, USA.

$$\mathbf{D} = \begin{pmatrix} \left[\frac{-g_0-\cdots-g_{\mathrm{n}-1}-g_{\mathrm{b}}}{C_{\mathrm{s}}}\right] & \frac{g_0}{C_{\mathrm{s}}} & \cdots & \frac{g_{\mathrm{n}-1}}{C_{\mathrm{s}}} \\ \frac{g_0}{C_{\mathrm{a}_0}} & -\frac{g_0}{C_{\mathrm{a}_0}} & 0 & 0 \\ \vdots & 0 & \ddots & 0 \\ \frac{g_{a_{\mathrm{n}-1}}}{C_{a_{\mathrm{n}-1}}} & 0 & 0 & -\frac{g_{n-1}}{C_{\mathrm{a}_{n-1}}} \end{pmatrix} \tag{6.22}$$

The ith row of the matrix $\mathbf{D}$ denotes the heat flow in and out of the ith system. Since the absorbers are only in thermal contact to the temperature sensor, the matrix solely has entries on the diagonal and on the first row and column, respectively. A more complex model can be introduced allowing thermal shortcuts from one absorber to the other but will not be discussed here. The absorption of X-rays in the absorber is represented by the vector **Qs**, that defines the initial temperature rise upon the absorption of energy at the time t_0 by the incoming energy and the heat capacity of the absorber, here the delta function $\delta(t)$ has the physical unit 1/s.

Internal noise

Predictions on energy resolution are only possible combing the detector response with the expected noise. For this a noise model including all the internal thermodynamic noise sources between the absorbers and the sensor was developed. The computed noise is combined with the noise sources described in section 2.5 to predict the energy resolution of each pixel.

To model the internal thermodynamic fluctuations, for each link g_i a noise contributions is introduced according to

$$S_{g_i}(f) = 4k_{\mathrm{B}}T^2 g_i \tag{6.23}$$

With this equation (6.20) takes the following form

$$\frac{\partial}{\partial t}\mathbf{T} = \mathbf{DT} + \mathbf{Qs} + \mathbf{Fn}, \tag{6.24}$$

with

$$\mathbf{F} = \begin{pmatrix} \left[\frac{-g_0-\cdots-g_{n-1}-g_{\mathrm{b}}}{C_{\mathrm{s}}}\right] & \frac{g_0}{C_{\mathrm{s}}} & \cdots & \frac{g_{n-1}}{C_{\mathrm{s}}} \\ 0 & -\frac{g_0}{C_{\mathrm{a}_0}} & 0 & 0 \\ 0 & 0 & \ddots & 0 \\ 0 & 0 & 0 & -\frac{g_{n-1}}{C_{\mathrm{a}_{n-1}}} \end{pmatrix} \tag{6.25}$$

and

$$\mathbf{n} = \begin{pmatrix} P_\mathrm{b} \\ P_0 \\ \vdots \\ P_{n-1} \end{pmatrix}. \tag{6.26}$$

To get the frequency response we use the Fourier transform of the matrix equation, thus $\partial/\partial t$ becomes $\imath\omega = \imath 2\pi f$. Introducing the unit matrix $\mathbf{I}$ equation (6.24) can be solved for $\mathbf{T}$.

$$\tilde{\mathbf{T}} = (\imath 2\pi f\mathbf{I} - \mathbf{D})^{-1}\mathbf{Q}\mathbf{s} + (\imath 2\pi f\mathbf{I} - \mathbf{D})^{-1}\mathbf{F}\mathbf{n}, \tag{6.27}$$

The first summand of this equation will give the frequency response of the temperature signal after the absorption of energy E. The second summand gives the frequency response of the noise caused by the thermal conductances between the absorbers and the sensor and the thermal conductance from the sensor to the bath. This can also be written as

$$\tilde{\mathbf{T}} = \tilde{\mathbf{S}}(f)\mathbf{s} + \tilde{\mathbf{N}}(f)\mathbf{n} \tag{6.28}$$

with

$$\tilde{S}(f) = (\imath 2\pi f\mathbf{I} - \mathbf{D})^{-1}\mathbf{Q} \tag{6.29}$$

and

$$\tilde{N}(f) = (\imath 2\pi f\mathbf{I} - \mathbf{D})^{-1}\mathbf{F}. \tag{6.30}$$

The frequency dependent response of the MMC after the absorption of energy E as well as the individual noise contributions can be extracted from 6.29 and 6.30, respectively. In particular, the temperature response of the sensor for energy deposition in the individual absorbers $i = 0 \ldots n-1$ is

$$p_T^i(f) = \sqrt{|S_{1,i+2}|^2 s_{i+2}^2}, \tag{6.31}$$

and the individual noise contributions originating from the fluctuations of energy between the individual absorber $i = 1 \ldots n-1$ and the temperature sensor are

$$S_T^i(f) = \sqrt{|N_{1,i+2}|^2 n_{i+2}^2}, \tag{6.32}$$

$S_T^{\mathrm{TD}}(f) = \sqrt{|N_{1,1}|^2 n_1^2}$ then describes the temperature noise caused by thermal fluctuations of energy between the sensor and the thermal bath. All temperature amplitudes can easily be transformed into flux signals in the SQUID by multiplying them with the temperature-to-flux transfer coefficient $\partial\Phi/\partial T$ of the temperature sensor.

6.3.7 Testing the model

The heat capacities of the sensor and the absorber, the thermal conductances and the measured magnetization – all determined from the experimental data – can now be used as input parameters for the thermal modeling of the pulses.

Figure 6.25 shows a comparison of the experimentally measured pulse shapes acquired at a temperature of $T = 35\,\mathrm{mK}$ to numerically simulated pulses. For the modeled pulses an absorber heat capacity for each absorber of $C_{a_i} = 0.55\,\mathrm{pJ/K}$, a sensor heat capacity of $C_s = 1.76\,\mathrm{pJ/K}$ as well as a slope of the temperature dependent magnetization signal of $\partial\Phi/\partial T = 670\,\Phi_0/\mathrm{K}$ were used as parameters as determined in section 6.3.3. The internal thermal conductances between each absorber and the sensor are used according to the geometries realized in the detector design. These thermal conductances were normalized to the measured thermal conductance from the sensor to the bath $g_b = 1.25\,\mathrm{nW/K}$.

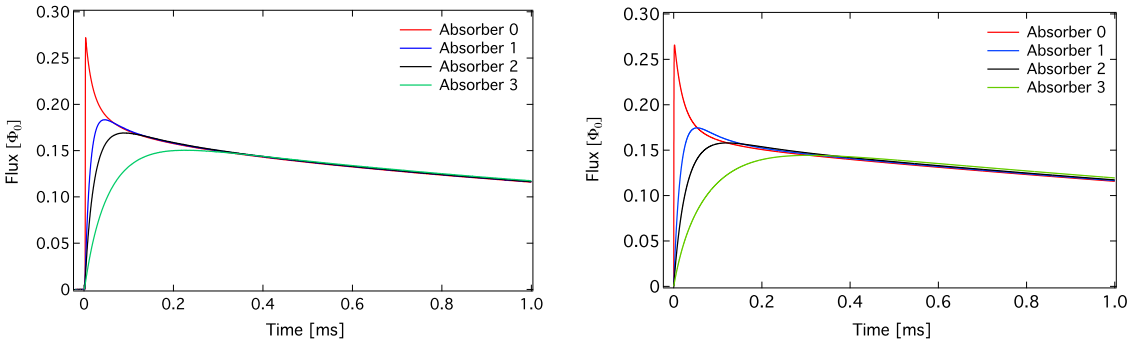

Figure 6.25 Comparison of measured pulse shapes (left) and numerically simulated pulse shapes (right) for X-ray absorption in the different absorbers.

In general the measured signal shapes and amplitude ratios agree well with those modeled. The rise times measured are approximately 20 % to 30 % shorter than modeled but still lead to a more than satisfactory position discrimination. A comparison of data from the experiment and the model is given in table 6.1. The left hand part of the table lists the 20 % to 80 % rise times of both. Here, the rise time for X-ray absorption in absorber 0 is listed to be less than $1\,\mu\mathrm{s}$, as the data shown was not taken with the highest possible time resolution.

The rise time of an absorber fabricated on top of the sensor was measured in a separate measurement with a setup of a single pixel detector. The majority of rise times seen there were $100 - 120\,\mathrm{ns}$ long [Ban09]. A distribution of rise times was observed in the single pixel experiment, this was interpreted as position sensitivity in the overhanging gold bismuth absorbers.

The right hand side of table 6.1 compares the rise times ratios from pixel to pixel determined in the experiment to the design values as described in section 4.2. It once more illustrates the good agreement between predictions and experimental data.

Table 6.1 Comparison of 20% to 80% rise times for experimentally measured and modeled pulses. On the right a comparison of rise time ratios to design values are listed.

	20%-80% rise time			**rise time ratios**	
Abs. Nr.	Experimental	Modeled	**ratios**	Experimental	Designed
0	$< 1\,\mu$s	$< 1\,\mu$s			
1	$22.9\,\mu$s	$27.9\,\mu$s	**2:1**	1.8	2
2	$41.2\,\mu$s	$56.8\,\mu$s	**3:1**	4.7	4.7
3	$107.6\,\mu$s	$146.8\,\mu$s	**3:2**	2.6	2.3

Overall these results are very encouraging as the scaling of the thermal properties are as expected. Future investigation of the thermal conductance through the membrane will be instructive to continue to improve the thermal modeling. To further improve the performance of the device simple adjustments like fabricating thermalization links of different thicknesses can be realized in future devices.

6.3.8 9 headed Hydra

The demonstrated performance of a Hydra detector with four absorbers and the reliable modeling of the detector response allows for further development towards a detector with more absorbers. As an example, in this section, a detector featuring nine absorbers is discussed on the basis of modeled data, the expected detector noise as well as the detector response are presented. Furthermore, the modeled signal shapes are combined with the noise. Standard data analysis is presented showing good position sensitivity throughout the tested energy range.

The detector presented features 9 absorbers with an area of $250\,\mu\text{m} \times 250\,\mu\text{m}$ each, giving a detection area of $A = 0.56\,\text{mm}^2$. The absorbers are assumed to be made of a gold bismuth bilayer. At an operational temperature of $T = 35\,\text{mK}$ a heat capacity of $C_{a_i} = 0.31\,\text{pJ/K}$ is attributed to each absorber, which is less than the heat capacity determined in the four absorber Hydra, but mimics the expected heat capacity for absorbers of that size assuming literature values of the specific heat of bulk bismuth. The assumed paramagnetic sensor is optimized for a total absorber heat capacity of $C_{\text{a}_{\text{tot}}} = 9 \times C_{a_i}$ based on the detector theory discussed in section 2.5 and matched accordingly. It is assumed to have a heat capacity of $C_\text{s} = 2.7\,\text{pJ/K}$, an erbium concentration of $x = 900\,\text{ppm}$ and a temperature-to-flux transfer coefficient of $\partial\Phi/\partial T = 1540\,\Phi_0/\,\text{K}$ at this temperature. Table 6.2 lists potential thermal conductances between each absorber and the sensor for such a device, the thermal conductances are given in units of the thermal conductance to the bath.

Table 6.2 Thermal conductances between the listed absorber and the sensor in units of the thermal conductance to the bath $g_\mathrm{b} = 1.25\,\mathrm{nW/K}$ and the theoretical energy resolution of a modeled position sensitive MMC.

Abs. Nr.	link strength	ΔE_FWHM [eV]
0	50000	2.9
1	40	3.1
2	26	3.2
3	18	3.3
4	13	3.4
5	9	3.4
6	6.5	3.5
7	5	3.6
8	3.5	3.8

Figure 6.26 shows the spectrum of magnetic flux noise in the SQUID for such a device. The solid blue line represents the quadratic sum of all noise contributions considered:

- The thermal fluctuations between the sensor and the bath show the usual plateau like behavior for low frequencies with a roll off at the inverse of the characteristic time constant given by the thermal conductance between the sensor and the bath and the total heat capacity. The value for $f \to 0$ is described by

$$\sqrt{S_\Phi^{g_\mathrm{b}}(f)} = \sqrt{4k_\mathrm{B}T^2/g_\mathrm{b}}\partial\Phi/\partial T \tag{6.33}$$

  and is found to be $11\,\mu\Phi_0/\sqrt{\mathrm{Hz}}$.

- The flux noise in the SQUID caused by thermal fluctuations of energy between the individual absorbers and the temperature sensor are shown as thin grey lines. All but the very strongly thermally coupled absorber show a plateau like noise that shows a roll off towards low and high frequencies. The plateau values of the flux noise are found to be between $0.08\,\mu\Phi_0/\sqrt{\mathrm{Hz}}$ and $0.4\,\mu\Phi_0/\sqrt{\mathrm{Hz}}$. For the stronger thermally coupled absorbers the plateau value is lower and the bandwidth is higher.

- The flux noise contribution of the SQUID is shown as a solid red line.

- The flux noise of the erbium ions is depicted as a solid green line.

The total noise is dominated by fundamental noise contributions in most regions of the frequency. The noise generated by the fluctuations of energy between the

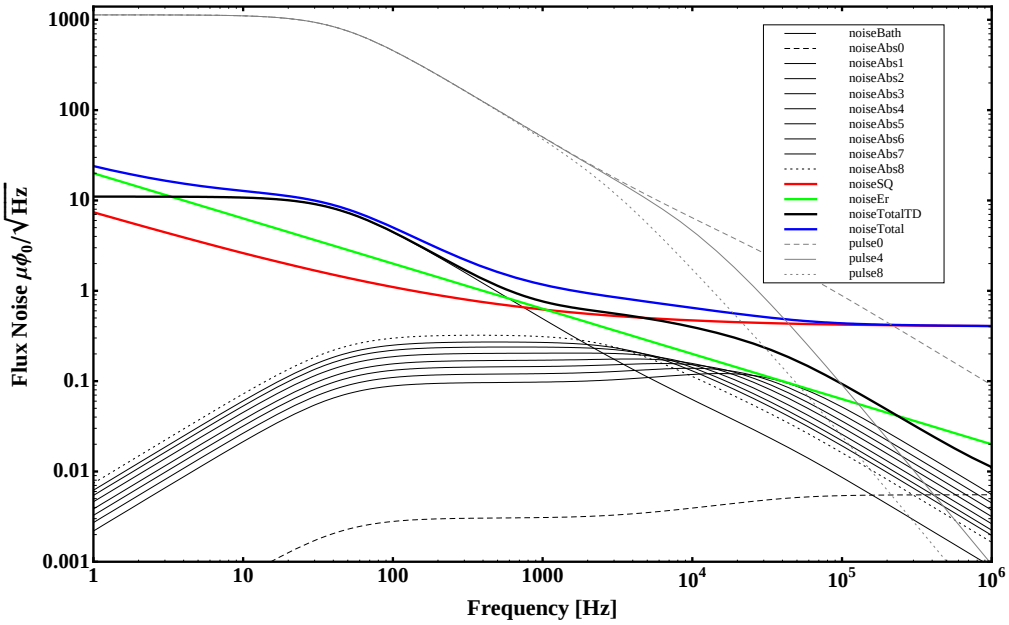

Figure 6.26 Modeled noise and detector response of a position sensitive MMC with 9 absorbers. All internal noise contributions are shown, but only three representative response functions are shown.

absorbers and the sensor do not contribute at low frequencies. For the higher frequencies the sum of all internal noise contributions is in the order of the SQUID noise. Overall, the signal to noise ratio is hardly degraded in the important low frequency range compared to a single pixel absorber with heat capacity $C_a = \sum_i C_{a_i}$. Of course the relatively high heat capacity of the 9 absorbers require a sensor with a steep temperature response and thus strong thermodynamic fluctuations can be observed.

The spectral shape of the detector response function is also depicted in figure 6.26. For low frequencies the response of all pixels is identical. For zero frequency up to the frequency determined by the inverse of the overall thermal decay time all pixels show a constant response. For even higher frequencies the signal of each pixel exhibits a second roll of that is dominated by the corresponding thermal conductance g_i. The more weakly linked absorbers roll of first, followed by the more strongly thermally coupled absorbers.

The time domain pulse shapes of such a device are shown in figure 6.27. For the pulses shown the position discrimination should be given. The noise remains unchanged for all pixels but as the frequency dependent signal response is different for all pixels the NEP will also be different for the individual pixels. Table 6.2 also lists the predicted energy resolution for each pixel. All 9 pixels show an excellent energy resolution ΔE_{FWHM} below 4 eV.

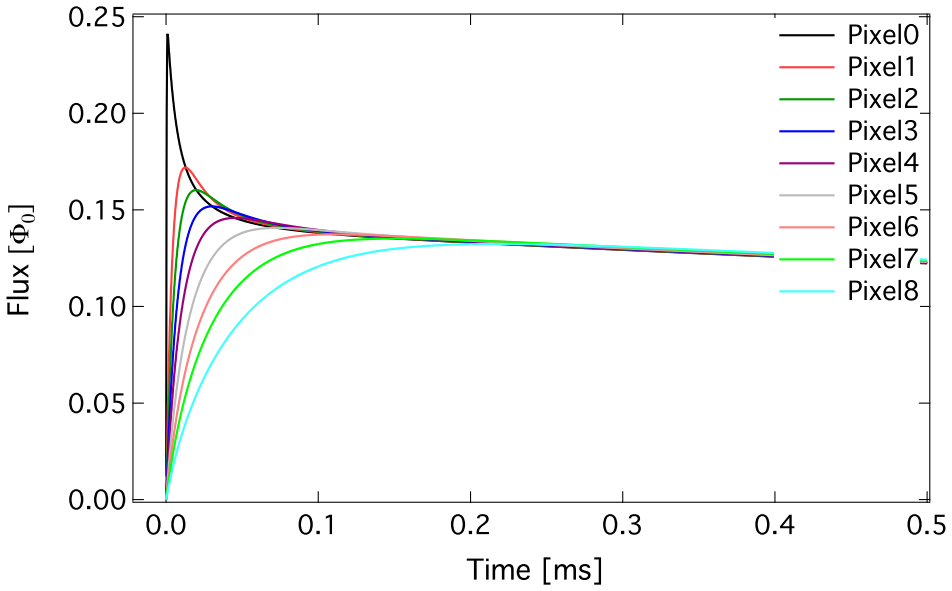

Figure 6.27 Modeled pulses of a position sensitive MMC with 9 absorbers.

To prove position sensitivity for all nine pixels across the studied energy range pulse spectra were synthesized by combining the modeled pulse shapes with the expected noise. The white noise and the thermodynamic fluctuations were modeled in the time domain by calculating 16 384 voltage samples from random numbers. The random numbers are mapped on the voltage samples by the inverse error function of given width. These time traces are then low pass filtered in time domain. For the white noise a high low pass frequency is introduced to prevent aliasing effects. The thermodynamic fluctuation noise is generated in the same way, the plateau value is determined and a low pass filter according to the dominant decay constant is applied.

At this stage an effective $1/f$ type noise was implemented for generating the synthesized data that represents the combined contributions of the flux noise attributed to the SQUID and of the flux noise attributed to the erbium ions. For the presented data an effective $1/f$-type noise was assumed as $\sqrt{S_\Phi^{1/\mathrm{f}}} = 10\,\mu\Phi_0/\sqrt{\mathrm{Hz}} \times 1/f$.

5000 pulse traces per pixel were created using the methods described above. Subsequently these data were analyzed regarding their rise time. The rise time was determined from the time taken for the pulse to rise from 20% to 80% of the maximum value. It was found that calculating the $20\% - 80\%$ rise time after smoothing the records for $20\,\mu$s leads to the best position discrimination. While synthesizing the data no digital low pass filter was implemented, in the case of the most strongly coupled absorber of Pixel 0 the rise times are thus very short and were determined without applying any smoothing algorithm.

Subsequent to synthesizing the signals, a template pulse is generated for each characteristic rise time and all events with that rise time are fitted with a time domain

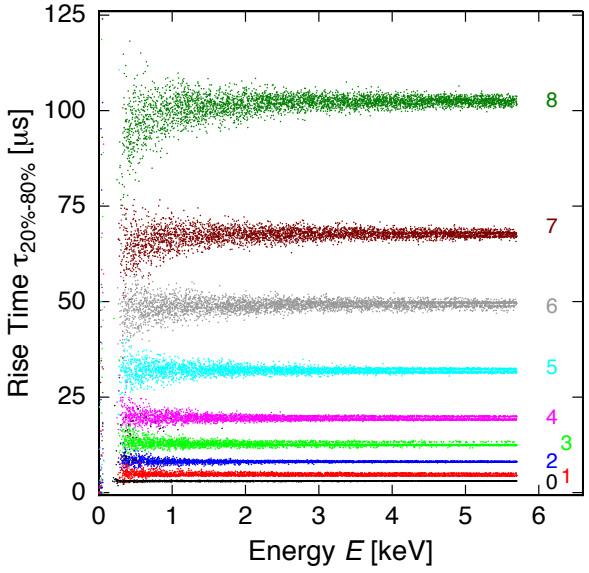

Figure 6.28 Analyzed rise times (20%−80%) of synthesized pulses for a 9 absorber Hydra detector.

based routine to determine a signal size relative to the template signal. Figure 6.28 shows the $20\% - 80\%$ rise time as a function of energy for the synthesized data sets of all 9 pixels.

A clear pixel discrimination can be seen even for energies down to 500 eV. The device presented can be read out by only one SQUID channel and is perfectly suited for high resolution experiments where very high event rates are not foreseen and a position resolved readout is required. The modeled data makes even larger devices appear plausible.

6.3.9 Conclusion

In this section the first experimental results for a four absorber position-sensitive magnetic calorimeters were presented. The observed device performance agrees well with calculations and modeling except for reduced signal sizes that are believed to be understood. Straightforward position discrimination using the pulse rise time has been demonstrated at 5.9 keV. These first generation devices demonstrate proof of concept and already show energy resolution close to those shown in single pixel devices. The best FWHM energy resolution achieved was under 5 eV across all four pixels, and the theoretically achievable energy resolution was below 3 eV across all pixels. This currently is the record for any position-sensitive micro-calorimeter at these energies. And as the coupling of the paramagnetic temperature sensor to the readout meander is still to be improved, larger signals are foreseen for detectors fabricated in future and thus the achieved energy resolution can be improved even further.

Conclusion and Outlook

Among other methods, the neutrino rest mass can be determined by investigating the endpoint region of the spectrum of a β-emitter. A good candidate is the β-spectrum of ^{187}Re, due to its relatively low endpoint energy. However, for any considered $\beta-$emitter, a quantitative statement about the neutrino rest mass can only be made by means of collecting a spectrum with very high statistics. To achieve this, the MARE project proposes the development of large detector arrays with ^{187}Re, in order to be sensitive to a neutrino mass of about $0.2\,\mathrm{eV/c^2}$ and possibly below.

Within this work developments for a high resolution neutrino rest mass detector based on calorimetric low temperature detectors were carried out. The detector is based on a fully micro-fabricated metallic magnetic calorimeter (MMC) that comprises of a paramagnetic temperature sensor located in a weak magnetic field. A rhenium cuboid, acting as absorber and β-source, is well thermally coupled to the sensor. At an operating temperature of about 50 mK the rhenium absorber is superconducting and should therefore have a very low heat capacity. An energy deposition by a β-particle within the absorber leads to a temperature increase of the detector and thus to a change of magnetization in the sensor. The detector makes use of a low noise dc-SQUID magnetometer which is inductively well coupled to the sensor to measure the corresponding magnetic flux change.

Within this thesis the detector theory of metallic magnetic calorimeter is presented and based on the well known properties of the sensor material Au:Er and all currently known noise contributions and detector prototype suited for a rhenium experiment is optimized.

While measuring the β-spectrum, the discrimination of consecutive nuclear decays is mandatory to avoid unresolved pileup events. At high decay rates unresolved pileup is only avoidable if the temperature rise in the sensor is sufficiently fast. This in turn means that a good thermal coupling of the absorber to the sensor is required. Therefore, in the framework of this thesis, a diffusion welding process to realize an entirely metallic connection was developed and characterized. It is also shown that the magnetic properties of the sensor remains unaltered after the 30 min heat treatment at 245 °C during the diffusion welding process.

Based on numerical optimization a detector was developed. The detector design

comprises of 8 photolithography masks and in total 7 layers were deposited in micro-fabrication. The MMC is based on a superconducting planar meander-shaped pick-up coil, that is covered by a sputter deposited Au:Er layer with an optimal erbium concentration of about 300 ppm. For diffusion welding the rhenium absorbers to the sensor and to reduce the probability of escaping high energetic phonons, the detector design includes gold stems that are electroplated in the last step of fabrication.

The characterization work for the detector covered three main steps. First, a fully micro-fabricated detector was developed and setup, but instead of a rhenium-an electroplated gold absorber was used. This way it was possible to ensure and compare the performance of the detector by simply taking spectra with an external X-ray source. This detector achieved an energy resolution of $\Delta E_{\mathrm{FWHM}} = 4.0\,\mathrm{eV}$, which is in good agreement with the theoretically expected value. This marks a significant progress in comparison to all the MMCs used before for rhenium experiments. Not only the energy resolution has been vastly improved, also the thermodynamic properties of the micro-fabricated sensors and absorbers have been proven to agree well with their corresponding bulk values.

The next two steps analyzed the impact of the rhenium absorbers on the detector performance. Two detectors with a polycrystalline rhenium foil and later with a large volume rhenium single crystal were built, respectively. Both detectors show signal rise times below $10\,\mu\mathrm{s}$. This is an order of magnitude lower than for all former detectors, where the absorber was glued to the temperature sensor creating a non-metallic interface. These detectors showed rise times between $100\,\mu\mathrm{s}$ and up to more than 1 ms. This improvement directly reduces the unresolved pileup rate at a given β-activity, and therefore shortens the total acquisition in the proposed MARE experiment.

For both of the rhenium detectors reduced signal sizes compared to expectations derived from the first detector were found. Still, with the polycrystalline foil the best X-ray energy resolution so far with an MMC based readout of a rhenium absorber of $\Delta E_{\mathrm{FWHM}} = 45\,\mathrm{eV}$ at 5.9 keV was achieved. The observations made for this detector suggest that an additional heat capacity of about $2\,\mathrm{pJ/K}$ can be attributed to the polycrystalline rhenium foil. No significant evidence could be found that a fraction of the incoming energy could not be measured by the temperature sensor. The detector with the large volume single crystal rhenium absorber was thoroughly characterized with the same X-ray source and showed drastically reduced signal sizes compared to expectations. Here an interpretation of an additional heat capacity does not hold and there is clear evidence that not the entire energy deposited in the detector can be detected by the MMC.

This finding points to complex intrinsic properties of rhenium as being a superconductor. The thermalization process in these systems is not well understood in the literature and further theoretical investigations would be helpful to understand

the underlying mechanisms. In the current state of the development the detector performance of the latest detector with large volume rhenium absorber is severely limited by reduced signal sizes.

Knowing the complexity of this topic, it should be very helpful for further research that within this work a detector platform has been developed that builds a basis to study different configurations of rhenium detectors on the way to a large scale neutrino mass experiment. It provides a low noise detector scheme with optimized coupling for the desired class of absorbers. With the developed fabrication techniques the desired fast signal rises could be achieved for both, polycrystalline and single crystal rhenium absorbers.

In addition to the single pixel detector development, an alternative approach of reading out many pixels was developed and tested in this thesis. Here, multiple absorbers are thermally coupled to a single sensor. Different thermal conductances from the individual absorbers to the sensor, as designed in the fabrication process, lead to different event rise times corresponding to the absorber the energy was deposited in.

Experimental results for a four-absorber position-sensitive metallic magnetic calorimeter are demonstrated. The observed device performance agrees well with calculations and modeled pulses. Straightforward position discrimination using the pulse rise time has been demonstrated at X-ray energies of 5.9 keV. These first generation devices demonstrate a proof of concept and already showed energy resolution close to those shown in single pixel devices. The best full width at half maximum energy resolution achieved was under $\Delta E_{\mathrm{FWHM}} < 5\,\mathrm{eV}$ across all four pixels, currently the record for any position-sensitive micro-calorimeter at this energy. With improved coupling of the magnetic temperature sensor larger signals are foreseen for detectors fabricated in future and, thus, the achieved energy resolution can be enhanced even further.

Part of this work was also the development of a thermal model to calculate the signals of events in the different absorbers and the expected noise from the fluctuations of energy between the weakly linked absorbers and the temperature sensor. On this basis a larger 9 pixel detector was modeled and which showed satisfactory position discrimination for all 9 pixels and an expected energy resolution of under $\Delta E_{\mathrm{FWHM}} < 4\,\mathrm{eV}$ across all pixels.

Bibliography

[Ang04] J. Angrik, T. Armbrust, A. Beglarian, U. Besserer, J. Blumer, et al., KATRIN Design Report, *FZK Scientific Report*, **7090**:1–245, 2004.

[Ard06] F. Ardellier, I. Barabanov, J. Barriere, F. Beiel, S. Berridge, et al., Double Chooz, A Search for the Neutrino Mixing Angle Θ_{13}, *arXiv [hep-ex]*, **0606025**], 2006.

[Arn05] R. Arnold, C. Augier, J. Baker, A. Barabash, G. Broudin, et al., First results of the search for neutrinoless double-beta decay with the NEMO 3 detector, *Phys. Rev. Lett.*, **95**(182302), 2005.

[Arn08] C. Arnaboldi, D. Artusa, F. Avignone, M. Balata, I. Bandac, et al., Results from a search for the $0\nu\beta\beta$-decay of ^{130}Te, *Phys. Rev. C*, **78**(3):035502, 2008.

[Ast10] Astro-H Mission, 2010, http://astro-h.isas.jaxa.jp/index.html.en.

[Ban93] S. R. Bandler, C. Enss, R. E. Lanou, H. J. Maris, T. More, et al., Metallic magnetic bolometers for particle detection, *J. Low Temp. Phys.*, **93**(3):709–714, 1993.

[Ban08] S. R. Bandler, R. P. Brekosky, A.-D. Brown, J. A. Chervenak, E. Figueroa-Feliciano, et al., Performance of TES X-ray microcalorimeters with a novel absorber design, *J. Low Temp. Phys.*, **151**(1):400–405, 2008.

[Ban09] S. R. Bandler, J.-P. Porst, J. S. Adams, J. Beyer, W.-T. Hsieh, et al., Performance of High-Resolution, Micro-fabricated, X-ray Magnetic Calorimeters, *AIP Conf. Proc.*, **1185**:579, 2009.

[Bro08] A.-D. Brown, S. R. Bandler, R. P. Brekosky, J. A. Chervenak, E. Figueroa-Feliciano, et al., Absorber Materials for Transition-Edge Sensor X-ray Microcalorimeters, *J. Low Temp. Phys.*, **151**(1):413–417, 2008.

[Büh88] M. Bühler and E. Umlauf, A magnetic bolometer for single-particle detection, *Europhys. Lett.*, **5**(4):297–301, 1988.

[Büh93] M. Bühler, T. Fausch, and E. Umlauf, Measurement of spin-lattice relaxation times at millikelvin temperatures, *Europhys. Lett.*, **23**(7):529–534, 1993.

[Büh94] M. Bühler, E. Umlauf, and J. C. Mather, Noise of a bolometer with vanishing self-heating, *Nucl. Instr. Meth. A.*, **346**:225–229, 1994.

[Bur08] A. Burck, S. Kempf, S. Schäfer, H. Rotzinger, M. Rodrigues, et al., Microstructured magnetic calorimeter with meander-shaped pickup coil, *J. Low Temp. Phys.*, **151**(1):337–344, 2008.

[Bur09] A. Burck, Entwicklung großflächiger mikrostrukturierter magnetischer Kalorimeter mit Au:Er- und Ag:Er-Sensoren für den energieaufgelösten Nachweis von Röntgenquanten und hochenergetischen Teilchen, *PhD thesis, Heidelberg University*, 148, 2009.

[But74] D. B. Butrymowicz, J. R. Manning, and M. E. Read, Diffusion in copper and copper alloys Part II. Copper-silver and copper-gold systems, *J. Phys. Chem. Ref Data*, **3**(2):527, 1974.

[CAS] Center for astronomy signal processing and electronics research, http://casper.berkeley.edu/.

[Che99] J. Chervenak, K. Irwin, E. Grossman, J. Martinis, C. Reintsema, et al., Superconducting multiplexer for arrays of transition edge sensors, *Appl. Phys. Lett.*, **74**(26):4043–4045, 1999.

[Cla04] J. Clarke and A. Braginski, *The SQUID Handbook: Fundamentals and Technology of SQUIDs and SQUID Systems, Volume 1* (Wiley - Weinheim, 2004).

[Cos93] E. Cosulich, F. Gatti, and S. Vitale, Further results on μ-calorimeters with superconducting absorber, *J. Low Temp. Phys.*, **93**(3):263–268, 1993.

[Cow56] C. Cowan, F. Reines, F. Harrison, H. Kruse, and A. MacGuire, Detection of the free neutrino: a confirmation, *Science*, **124**:103–104, 1956.

[Cun02] M. Cunningham, J. Ullom, T. Miyazaki, S. Labov, J. Clarke, et al., High-resolution operation of frequency-multiplexed transition-edge photon sensors, *Appl. Phys. Lett.*, **81**(1):159–161, 2002.

[Dav73] D. Davidov, C. Rettori, A. Dixon, K. Baberschke, E. P. Chock, et al., Crystalline-field effects in the electron-spin resonance of rare earths in the noble metals, *Phys. Rev. B*, **8**(8):3563–3568, 1973.

[Day03] P. K. Day, H. G. Leduc, B. A. Mazin, A. Vayonakis, and J. Zmuidzinas, A broadband superconducting detector suitable for use in large arrays, *Nature*, **425**:817–821, 2003.

[dK03] P. de Korte, J. Beyer, S. Deiker, G. Hilton, K. Irwin, et al., Time-division superconducting quantum interference device multiplexer for transition-edge sensors, *Rev. Sci. Instrum.*, **74**(8):3807–3815, 2003.

[Dor04] W. Doriese, J. Beall, S. Deiker, W. Duncan, L. Ferreira, et al., Time-division multiplexing of high-resolution X-ray microcalorimeters: Four pixels and beyond, *Appl. Phys. Lett.*, **85**(20):4762–4764, 2004.

[Dre10] P. Dreiske, M. Carmody, C. Grein, J. Zhao, R. Bommena, et al., Molecular Beam Epitaxially Grown HgTe and HgCdTe-on-Silicon for Space-Based X-Ray Calorimetry Applications, *Journal of Electronic Materials*, **39**(7):1087–1096, 2010.

[Dru07] D. Drung, C. Assmann, J. Beyer, A. Kirste, M. Peters, et al., Highly sensitive and easy-to-use SQUID sensors, *IEEE Transactions on Applied Superconductivity*, **17**(2):699, 2007.

[Dvo09] R. Dvornicky and F. Simkovic, Measuring mass of neutrinos with beta-decays of tritium and rhenium, *Workshop on Calculation of Double-Beta-Decay Matrix Elements (MEDEX '09)*, 1–5, 2009.

[Ens05] C. Enss and S. Hunklinger, Low-temperature physics, *Springer-Verlag Berlin, Heidelberg*, 2005.

[Fer09] E. Ferri, C. Arnaboldi, G. Ceruti, C. A. Kilbourne, S. Kraft-Bermuth, et al., Status of the MARE experiment in Milan, *AIP Conf. Proc.*, **1185**(1):565–568, 2009.

[Fle98] A. Fleischmann, Hochauflösendes magnetisches kalorimeter zur detektion von einzelnen röntgenquanten, *Diploma Thesis, Heidelberg University*, 1–79, 1998.

[Fle03] A. Fleischmann, Magnetische Mikrokalorimeter: Hochauflösende Röntgenspektroskopie mit energiedispersiven Detektoren, *Ph.D. thesis, Heidelberg University*, 2003.

[Fle05] A. Fleischmann, C. Enss, and G. M. Seidel, Metallic Magnetic Calorimeters, in *Cryogenic Particle Detection* (ed.: C. Enss), volume 99 of *Topics in Applied Physics*, 151–216 (Springer Berlin,Heidelberg, 2005).

[Fle09a] A. Fleischmann, L. Gastaldo, J.-P. Porst, S. Kempf, A. Kirsch, et al., Metallic magnetic calorimeters, *AIP Conf. Proc.*, **1185**:571, 2009.

[Fle09b] L. Fleischmann, M. Linck, A. Burck, J.-P. Porst, S. Kempf, et al., Metallic Magnetic Calorimeters for X-Ray Spectroscopy, *IEEE Transactions on Applied Superconductivity*, **19**(2):63–68, 2009.

[Fog06] G. L. Fogli, E. Lisi, A. Marrone, and A. Palazzo, Global analysis of three-flavor neutrino masses and mixings, *Progress in Particle and Nuclear Physics*, **57**:742–795, 2006.

[Fog08a] G. Fogli, E. Lisi, A. Marrone, A. Palazzo, and A. Rotunno, Hints of $\theta_{13} > 0$ from global neutrino data analysis, *Phys. Rev. Lett.*, **101**(14):141801, 2008.

[Fog08b] G. L. Fogli, E. Lisi, A. Marrone, and A. Melchiorri, Observables sensitive to absolute neutrino masses. II, *Phys. Rev. D*, **78**(3), 2008.

[Gas09] L. Gastaldo, J. Porst, F. von Seggern, A. Kirsch, P. Ranitzsch, et al., Low Temperature Magnetic Calorimeters For Neutrino Mass Direct Measurement, *AIP Conf. Proc.*, **1185**:607–611, 2009.

[Gat00] F. Gatti, F. Fontanelli, M. Galeazzi, and S. Vitale, First results of the calorimetric spectrometer for the beta decay of rhenium-187, *Nucl. Instr. Meth. A.*, **444**(1-2):88–91, 2000.

[Gat06a] F. Gatti, private communication, 2006.

[Gat06b] F. Gatti et al., MARE - Microcalorimeter Arrays for a Rhenium Experiment, 2006.

[Gen09] Gen X, 2009, http://www.cfa.harvard.edu/hea/genx.html.

[GH71] P. E. Gregers-Hansen, M. Krusius, and G. R. Pickett, Sign of the nuclear quadrupole interaction in rhenium metal, *Phys. Rev. Lett.*, **27**(1):38–41, 1971.

[Giu07] C. Giunti and C. W. Kim, Fundamentals of neutrino physics and astrophysics, *Oxford University Press, USA*, 2007.

[Hah92] W. Hahn, M. Loewenhaupt, and B. Frick, Crystal field excitations in dilute rare earth noble metal alloys, *Physica B*, **180 & 181**:176–178, 1992.

[Hal77] P. Hall, J. Morabito, and N. Panousis, Interdiffusion in the Cu–Au thin film system at 25 °C to 250 °C, *Thin Solid Films*, **41**(3):341–361, 1977.

[Han10] S. Hannestad, The connection between cosmology and neutrino physics, *arXiv [astro-ph]*, **1003.4119v1**, 2010.

[Hau06] D. Haug, Entwicklung eines magnetischen Kalorimeters zur Neutrinomassenbestimmung aus dem Endpunkt des β-Spektrums von ^{187}Re, *Diploma Thesis, Heidelberg University*, 2006.

[Hen93] B. Henke, E. Gullikson, and J. Davis, X-ray interactions: Photoabsorption, scattering, transmission, and reflection at $E = 50 - 30,000\,\mathrm{eV}$, $Z = 1 - 92$, *Atomic Data and Nuclear Data Tables*, **54**(2):181–342, 1993.

[Höh08] C. Höhn, Investigation of the thermalisation in a metallic magnetic calorimeter with a superconducting rhenium absorber, *Diploma Thesis, Heidelberg University*, 2008.

[Höl97] G. Hölzer, M. Fritsch, M. Deutsch, J. Härtwig, and E. Förster, $K_{\alpha_{1,2}}$ and $K_{\beta_{1,3}}$ x-ray emission lines of the 3d transition metals, *Phys. Rev. A*, **56**(6):4554–4567, 1997.

[Hsi08] W.-T. Hsieh, J. S. Adams, S. R. Bandler, J. Beyer, K. Denis, et al., Fabrication of metallic magnetic calorimeter x-ray detector arrays, *J. Low Temp. Phys.*, **151**(1):357–362, 2008.

[Hsi09] W.-T. Hsieh, S. R. Bandler, D. P. Kelley, J.-P. Porst, H. Rotzinger, et al., Microfabrication of High Resolution X-ray Magnetic Calorimeters, *AIP Conf. Proc.*, **1185**:591, 2009.

[Irw04] K. Irwin and K. W. Lehnert, Microwave SQUID multiplexer, *Appl. Phys. Lett.*, **85**(11):2107–2109, 2004.

[Irw05] K. D. Irwin and G. C. Hilton, Transition-Edge Sensors, in *Cryogenic Particle Detection* (ed.: C. Enss), volume 99 of *Topics in Applied Physics*, 63–150 (Springer Berlin,Heidelberg, 2005).

[Joc10] J. Jochum, Germanium detector array–GERDA, *Progress in Particle and Nuclear Physics*, **64**:261–263, 2010.

[Kap76] S. B. Kaplan, C. C. Chi, D. N. Langenberg, J. J. Chang, S. Jafarey, et al., Quasiparticle and phonon lifetimes in superconductors, *Phys. Rev. B*, **14**(11):4854–4873, 1976.

[Kim08] S.-B. Kim and the RENO Collaboration, RENO: reactor experiment for neutrino oscillation at Yonggwang, *Journal of Physics: Conference Series*, **120**(5):052025, 2008.

[Kir10] A. Kirsch, Entwicklung eines mikrostrukturierten metallisch magnetischen Kalorimeters mit massivem Rheniumabsorber zur β-Spektroskopie von ^{187}Re, *Diploma Thesis, Heidelberg University*, 2010.

[Kit06] C. Kittel, *Einführung in die Festkörperphysik* (Oldenbourg Wissenschaftsverlag, 2006).

[KK01] H. Klapdor-Kleingrothaus, A. Dietz, L. Baudis, G. Heusser, I. Krivosheina, et al., Latest results from the HEIDELBERG-MOSCOW double beta decay experiment, *Eur Phys J A*, **12**(2):147–154, 2001.

[Koz00] A. G. Kozorezov, A. F. Volkov, J. K. Wigmore, A. Peacock, A. Poelaert, et al., Quasiparticle-phonon downconversion in nonequilibrium superconductors, *Phys. Rev. B*, **61**(17):11807–11819, 2000.

[Kra05] C. Kraus, B. Bornschein, L. Bornschein, J. Bonn, B. Flatt, et al., Final results from phase II of the Mainz neutrino mass search in tritium β-decay, *Eur. Phys. J. C*, **40**(4):447–468, 2005.

[Les06] J. Lesgourgues and S. Pastor, Massive neutrinos and cosmology, *Physics Reports*, **429**(6):307–379, 2006.

[Lob85] V. M. Lobashev and P. E. Spivak, A method for measuring the electron antineutrino rest mass, *Nucl. Instr. Meth. A.*, **240**(2):305–310, 1985.

[Lob03] V. M. Lobashev, The search for the neutrino mass by direct method in the tritium β-decay and perspectives of study it in the project KATRIN, *Nuclear Physics A*, **719**:153c–160c, 2003.

[Lor02] T. Loredo and D. Lamb, Bayesian analysis of neutrinos observed from supernova SN 1987A, *Phys. Rev. D.*, **65**(6):063002, 2002.

[Maz10] B. A. Mazin, K. O'Brien, S. McHugh, B. Bumble, D. Moore, et al., ARCHONS: A highly multiplexed superconducting optical to near-IR camera, *Proc. of SPIE*, **7735**(1):773518–1, 2010.

[McC05] D. McCammon, Semiconductor Thermistors, in *Cryogenic Particle Detection* (ed.: C. Enss), volume 99 of *Topics in Applied Physics*, 35–62 (Springer Berlin,Heidelberg, 2005).

[Mon09] B. Monreal and J. A. Formaggio, Relativistic cyclotron radiation detection of tritium decay electrons as a new technique for measuring the neutrino mass, *Phys. Rev. D.*, **80**(5):051301, 2009.

[Nuc09] A. Nucciotti, E. Ferri, and O. Cremonesi, Expectations for a new calorimetric neutrino mass experiment, *arXiv [hep-ph]*, **0912.4638v1**, 2009.

[Nuc10] A. Nucciotti, Neutrino mass calorimetric searches in the MARE experiment, *Presentation: Neutrino 2010 conferecen, Athens*, 2010.

[PDG10] PDG, Particle Data Group - The Review of Particle Physics 2010, *J. Phys. G*, **37**(075021), 2010.

[Per04] E. Perinati, M. Barbera, A. Collura, S. Serio, and E. Silver, Spectral broadening by incomplete thermalization of the energy in X-ray microcalorimeters with superconducting absorber and NTD-Ge thermal sensor, *Nucl. Instr. Meth. A.*, **531**(3):459–466, 2004.

[Per08] E. Perinati, M. Barbera, S. Varisco, E. Silver, J. Beeman, et al., Experimental evidence of an incomplete thermalization of the energy in an X-ray microcalorimeter with a Ta/Au absorber, *Rev. Sci. Instrum.*, **79**(5):053905, 2008.

[Phi64] N. E. Phillips, Low-Temperature Heat Capacities of Gallium, Cadmium, and Copper, *Phys. Rev.*, **134**(2A):A385–A391, 1964.

[Pin72] M. Pinnel and J. Bennett, Mass diffusion in polycrystalline copper/electroplated gold planar couples, *Metallurgical and Materials Transactions B*, **3**:1989–1997, 1972.

[Pir81] T. Piran, Neutrino mass and detection of neutrino supernova bursts, *Physics Letters B*, **102B**(4):299–302, 1981.

[Pob07] F. Pobell, Matter and methods at low temperatures, *Springer-Verlag Berlin Heidelberg*, 2007.

[Por07] J.-P. Porst, Towards mare: Development of a metallic magnetic calorimeter with superconducting rhenium absorber, *Diploma Thesis, Heidelberg University*, 2007.

[Por08] J.-P. Porst, C. Höhn, D. Haug, R. Weldle, G. M. Seidel, et al., Properties of Superconducting Rhenium as an Absorber for Magnetic Calorimeters, *J. Low Temp. Phys.*, **151**(1-2):436–442, 2008.

[Por09] J.-P. Porst, S. R. Bandler, J. S. Adams, W.-T. Hsieh, H. Rotzinger, et al., Development of Position-Sensitive Magnetic Calorimeter X-ray Detectors, *AIP Conf. Proc.*, **1185**:599, 2009.

[Ran09] P. Ranitzsch, Low temperature calorimeters with superconducting particle absorbers, *Diploma Thesis, Heidelberg University*, 2009.

[Rei03] C. Reintsema, J. Beyer, S. Nam, S. Deiker, G. Hilton, et al., Prototype system for superconducting quantum interference device multiplexing of large-format transition-edge sensor arrays, *Rev. Sci. Instrum.*, **74**(10):4500–4508, 2003.

[Rid65] P. E. Rider, K. Gschneider, and O. D. McMaster, Gold-rich rare-earth-gold solid solutions, *Trans. Metallurgical Soc. AIME*, **233**:1488, 1965.

[Rod06] V. Rodin, A. Faessler, F. Simkovic, and P. Vogel, Assessment of uncertainties in QRPA $0\nu\beta\beta$-decay nuclear matrix elements, *Nuclear Physics A*, **766**:107–131, 2006.

[Rod07] V. Rodin, A. Faessler, F. Simkovic, and P. Vogel, Erratum to: *Assessment of uncertainties in QRPA $0\nu\beta\beta$-decay nuclear matrix elements* in *Nucl. Phys. A 766,*(2006) 107, *Nuclear Physics A*, **793**(1-4):213–215, 2007.

[Sch87] D. Schramm, Neutrinos from supernova SN 1987A, *Comments Nucl. Part. Phys.*, **17**:239, 1987.

[Sch08] T. Schwetz, M. Tórtola, and R. Valle, Three-flavour neutrino oscillation update, *New Journal of Physics*, **10**(113011), 2008.

[Sha67] J. K. N. Sharma, Heat conductivities below 1K, I, *Cryogenics*, **7**(1-4):141–156, 1967.

[Sim81] J. J. Simpson, Measurement of the β-energy spectrum of ^{3}H to determine the antineutrino mass, *Phys. Rev. D*, **23**(3):649, 1981.

[Sis04] M. Sisti, C. Arnaboldi, C. Brofferio, G. Ceruti, O. Cremonesi, et al., New limits from the milano neutrino mass experiment with thermal microcalorimeters; proceedings of the 10th international workshop on low temperature detectors, *Nucl. Instr. Meth. A.*, **520**(1-3):125–131, 2004.

[Sis10] M. Sisti, From cuoricino to cuore: Investigating neutrino properties with double beta decay, *Journal of Physics: Conference Series*, **203**(012069), 2010.

[Sjö75] M. Sjöstrand and G. M. Seidel, Hyperfine resonance properties of Er^{3+} in Au, *Phys. Rev. B*, **11**(9):3292–3297, 1975.

[Smi70] D. R. Smith and P. H. Keesom, Specific Heat of Rhenium between 0.15 and 4.0 K, *Phys. Rev. B*, **1**(1):188–192, 1970.

[Smi08] S. J. Smith, S. R. Bandler, R. P. Brekosky, A.-D. Brown, E. Figueroa-Feliciano, et al., Development of arrays of position-sensitive microcalorimeters for Constellation-X, *Proc. of SPIE*, **7011**(701126), 2008.

[Smi09a] S. J. Smith, Implementation of complex signal-processing algorithms for position-sensitive microcalorimeters, *Nucl. Instr. Meth. A.*, **602**:537–544, 2009.

[Smi09b] S. J. Smith, S. R. Bandler, R. P. Brekosky, A.-D. Brown, J. A. Chervenak, et al., Development of position-sensitive transition-edge sensor X-ray detectors, *IEEE Transactions on Applied Superconductivity*, **19**(3, Part 1):451 – 455, 2009.

[Swa89] E. Swartz and R. Pohl, Thermal boundary resistance, *Rev. Mod. Phys.*, **61**(3):605–668, 1989.

[Szy93] A. E. Szymkowiak, R. L. Kelley, S. H. Moseley, and C. K. Stahle, Signal processing for microcalorimeters, *J. Low Temp. Phys.*, 1993.

[Tao71] L. Tao, D. Davidov, R. Orbach, and E. Chock, Hyperfine Splitting of Er and Yb Resonances in Au: A Separation between the Atomic and Covalent Contributions to the Exchange Integral, *Phys. Rev. B*, **4**(1):5, 1971.

[Tau04] J. Tauber, The Planck mission, *Advances in Space Research*, 2004.

[Tul80] N. Tulina, Influence of renium purity on the magnetic characteristics in the superconducting state, *Fizika metallov i metallovedenie*, **50**:747, 1980.

[Twe88] D. Twerenbold, Superconducting tunneling junctions as X-ray detectors and their possible applications in astrophysics, *Nucl. Instr. Meth. A.*, **273**(2-3):575–582, 1988.

[vdK02] J. van der Kuur, P. de Korte, H. Hoevers, M. Kiviranta, and H. Seppa, Performance of an X-ray microcalorimeter under ac biasing, *Appl. Phys. Lett.*, **81**(23):4467–4469, 2002.

[vS81] Y. von Spalden and K. Baberschke, Analysis of the residual linewidth in electron-paramagnetic resonance of AuEr and AuYb, *Journal of Magnetism and Magnetic Materials*, **23**:183, 1981.

[Wan09] W. Wang, For the Daya Bay Collaboration: The hunt for θ_{13} at the Daya Bay nuclear power plant, *arXiv [hep-ex]*, **0910.4605v1**, 2009.

[Wei96] H. Weinstock, Squid sensors: fundamentals, fabrication, and applications, *Kluwer Academic Publishers*, 1996.

[Wel08] R. Weldle, Untersuchung des Effekts magnetischer Verunreinigungen auf das Thermalisierungsverhalten von supraleitenden Teilchenabsorbern, *Diploma Thesis, Heidelberg University*, 2008.

[Wil69] G. Williams and L. L. Hirst, Crystal-field effects in solid solutions of rare earths in noble metals, *Phys. Rev.*, **185**(2):407–415, 1969.

[Win07] M. Winter, Webelements$^{\text{TM}}$, the periodic table on the www, 2007.

[Wol08] S. Wolk, R. Brissenden, M. Elvis, G. Fabbiano, A. E. Hornschneider, et al., Science with Generation-X, *Proc. of SPIE*, **7011**:701130, 2008.

[Yoo01] J. Yoon, J. Clarke, J. Gildemeister, A. Lee, M. Myers, et al., Single superconducting quantum interference device multiplexer for arrays of low-temperature sensors, *Appl. Phys. Lett.*, **78**(3):371–373, 2001.

[Zin04] B. L. Zink, K. Irwin, G. Hilton, D. Pappas, J. Ullom, et al., Lithographically patterned magnetic calorimeter X-ray detectors with integrated SQUID readout, *Nucl. Instr. Meth. A.*, **520**(1-3):52–55, 2004.

[Zin06] B. L. Zink, J. Ullom, J. A. Beall, K. Irwin, W. B. Doriese, et al., Array-compatible transition-edge sensor microcalorimeter gamma-ray detector with 42 eV energy resolution at 103 keV, *Appl. Phys. Lett.*, **89**(12):124101, 2006.

[Zub06] K. Zuber, Neutrinoless double beta decay experiments, *arXiv [nucl-ex]*, **0610007v1**, 2006.

Acknowledgments

There are many people whom I would like to thank for the role they played, be it academic or otherwise, in making this project possible.

Professor Christian Enss for kindly welcoming me in his exciting group and opening up the opportunity to experience the Goddard group.

I thank Professor Klaus Blaum for taking the time to be on my reading committee. Also thanks to Professor Heinz Horner and Professor Andreas Wolf for being in my dissertation committee.

Special thanks go to Loredana Gastaldo for being excited over every pulse seen and her support to finish this work. Additional gratitude is due for Andreas Fleischmann for all his input over the years, as well as for proof reading.

I also thank Professor George M. Seidel for making my extended visit to the US possible as well as supporting my attendance at the LTD-13 workshop.

For my stay at Goddard I wish to thank Simon Bandler not only for kindly introducing me to the group, but also for our daily discussions during my stay. Here my thanks also go to Stephen Smith for the many fruitful discussions on Hydras and for exploring DCs nightlife. My "thank you" of course extends to the entire X-ray Calorimeter Group at Goddard: Joe Adams, Regis Brekosky, Megan Eckart, Fred Finkenbeiner, Wen-Ting Hsieh, Richard Kelley, Dan Kelly, Caroline Kilbourne, Scott Porter, Jack Sadleir, Thomas Stevenson who welcomed and supported the German.

Of course all this work would be inconceivable without my fellow Ph.D. students and the numerous Diploma students, who helped pushing the MMC projects forward over the last years. Special thanks go to Sebastian Kempf, Christian Pies and Sönke Schäfer – without our discussions and mutual support, this work would not have been possible. All the Bolos accompanying me and the rhenium project over the last year should not be unmentioned: Andreas Burck, Christian Domesle, Daniel Haug, Sebastian Heuser, Christian Höhn, Alexandra Kampkötter, Andrea Kirsch, Stefan Lausberg, Andreas Pabinger, Philipp Ranitzsch, Falk v. Seggern and Richard Weldle – thank you!

From the group of Bolos I wish to point out my gratitude to Hannes Rotzinger. The fruitful discussions around Heidelberg's bars as well as all the advice and help you offered helped me a lot.

In addition I thank all the No-Bolos: Masoomeh Baszrafshan, Gudrun Fickenscher, Angela Halfar, Gernot Kasper, Florian Klotz, Manfred von Schickfus and Andreas Reiser – though mostly not sharing the same lab, I appreciated your sympathy for dying SQUIDs, lost rhenium crystals and leaking fridges and I enjoyed the extended coffee hours.

I thank Thomas Wolf for all the fabricated wafers, diced crystals and the tireless efforts to make the impossible come true. Also my thank goes to Rudi Eitel and Ralf Achenbach for their technical support.

Finally, I wish to thank my parents, without your unlimited support and your far-reaching advice I would never have come to this point. I also thank my brother Sven and Jule for all their support over the last years.